Theses and Dissertations | 1. Thesis and Dissertation Collection, all items

2008-09

Enhanced detection of orthogonal radar waveforms using time-frequency and bi-frequency signal processing techniques

Crescitelli, David M.; Kistner, Patrick B.

Monterey, California. Naval Postgraduate School

http://hdl.handle.net/10945/3931

NAVAL POSTGRADUATE SCHOOL

MONTEREY, CALIFORNIA

THESIS

ENHANCED DETECTION OF ORTHOGONAL RADAR WAVEFORMS USING TIME-FREQUENCY AND BI-FREQUENCY SIGNAL PROCESSING TECHNIQUES

by

Patrick B. Kistner
David M. Crescitelli

September 2008

Thesis Advisor:	Phillip E. Pace
Second Reader:	Terry E. Smith

THIS PAGE INTENTIONALLY LEFT BLANK

REPORT DOCUMENTATION PAGE		*Form Approved OMB No. 0704-0188*
Public reporting burden for this collection of information is estimated to average 1 hour per response, including the time for reviewing instruction, searching existing data sources, gathering and maintaining the data needed, and completing and reviewing the collection of information. Send comments regarding this burden estimate or any other aspect of this collection of information, including suggestions for reducing this burden, to Washington headquarters Services, Directorate for Information Operations and Reports, 1215 Jefferson Davis Highway, Suite 1204, Arlington, VA 22202-4302, and to the Office of Management and Budget, Paperwork Reduction Project (0704-0188) Washington DC 20503.

13. ABSTRACT (maximum 200 words)

This thesis investigates the periodic autocorrelation function (PACF) and periodic ambiguity function (PAF) for orthogonal continuous waveform (CW) modulations used in netted low probability of intercept (LPI) radar. Three orthogonal polyphase sequences and one frequency coding sequence are examined and their PACF and PAF characteristics are quantified. The Wigner-Ville distribution (WVD) and quadrature mirror filter bank (QMFB) time-frequency signal processing techniques and the cyclostationary bi-frequency technique (often used in non-cooperative intercept receivers) are used to detect the orthogonal CW signals and extract their parameters. The results shows that a combination of the techniques used were able to extract the basic signal parameters of bandwidth and code period from the polyphase waveforms and also the frequency hop slots and code length from the frequency coding sequence. The concept of using a swarm of unmanned aerial vehicles (UAV) is examined from the viewpoint of a coordinated group of netted intercept receivers in search of an LPI radar network.

14. SUBJECT TERMS Polyphase, Orthogonal, Netted Radar, Simulated Annealing, Signal Design, LPI, UAV Swarm, Stigmergy, and Gossip Network.

15. NUMBER OF PAGES
135

16. PRICE CODE

17. SECURITY CLASSIFICATION OF REPORT
Unclassified

18. SECURITY CLASSIFICATION OF THIS PAGE
Unclassified

19. SECURITY CLASSIFICATION OF ABSTRACT
Unclassified

20. LIMITATION OF ABSTRACT
UU

THIS PAGE INTENTIONALLY LEFT BLANK

ENHANCED DETECTION OF ORTHOGONAL RADAR WAVEFORMS USING TIME-FREQUENCY AND BI-FREQUENCY SIGNAL PROCESSING TECHNIQUES

Patrick B. Kistner
Lieutenant, United States Navy
B.S., New School for Social Research, 1994

David M. Crescitelli
Lieutenant, United States Navy
B.S., United States Naval Academy, 2002

Submitted in partial fulfillment of the
requirements for the degree of

**MASTER OF SCIENCE IN INFORMATION WARFARE
SYSTEMS ENGINEERING**

from the

**NAVAL POSTGRADUATE SCHOOL
September 2008**

Authors: Patrick B. Kistner

                 David M. Crescitelli

Approved by: Phillip E. Pace
                 Thesis Advisor

                 Terry E. Smith
                 Second Reader

                 Professor Dan Boger
                 Chairman, Department of Information Sciences

iii

THIS PAGE INTENTIONALLY LEFT BLANK

ABSTRACT

This thesis investigates the periodic autocorrelation function (PACF) and periodic ambiguity function (PAF) for orthogonal continuous waveform (CW) modulations used in netted low probability of intercept (LPI) radar. Three orthogonal polyphase sequences and one frequency coding sequence are examined and their PACF and PAF characteristics are quantified. The Wigner-Ville distribution (WVD) and quadrature mirror filter bank (QMFB) time-frequency signal processing techniques and the cyclostationary bi-frequency technique (often used in non-cooperative intercept receivers) are used to detect the orthogonal CW signals and extract their parameters. The results shows that a combination of the techniques used were able to extract the basic signal parameters of bandwidth and code period from the polyphase waveforms and also the frequency hop slots and code length from the frequency coding sequence. The concept of using a swarm of unmanned aerial vehicles (UAV) is examined from the viewpoint of a coordinated group of netted intercept receivers in search of an LPI radar network.

THIS PAGE INTENTIONALLY LEFT BLANK

TABLE OF CONTENTS

LIST OF FIGURES

x

THIS PAGE INTENTIONALLY LEFT BLANK

LIST OF TABLES

THIS PAGE INTENTIONALLY LEFT BLANK

ACKNOWLEDGMENTS

THIS PAGE INTENTIONALLY LEFT BLANK

I. INTRODUCTION

A. ORTHOGONAL NETTED LPI RADAR SYSTEMS

The term LPI is that property of radar theory that, because of its lower transmitted power, wide bandwidth, frequency variability, or other design characteristics, make it difficult to be detected by a non-cooperative passive intercept receiver. The principle of target detection by the radar prior to the target being able to detect the electromagnetic energy from the radar is the key to LPI. Radars that possess these qualities reduce their vulnerability to detection, location, and most importantly destruction. LPI radars are able to provide the operator with warning of incoming targets while remaining relatively invisible to the target. This distinct advantage is the impetus for the great interest in the ability to produce viable LPI radars and systems that can detect an adversarial LPI radar system. LPI radar is typically identified by one or more of the following characteristics [1]:

- Low average power continuous wave (CW) radiation with a large time bandwidth product.

- Radiated energy that is spread over a wide angular region, wide frequency band, and long time interval.

- Ultra-low side lobe transmit antenna

- Power management via radiation only as necessary to obtain target information, reduced levels to maintain situational awareness of target movement, and a reduction in power as a target gets closer to the radar.

- Utilization of the properties of the atmosphere to attenuate a radar signal beyond a usable range.

The networking of LPI radar systems will further reduce their vulnerability probability of detection by non-cooperative electronic support receivers (ESR). A networked LPI system can share target information in one of two ways. The first method

1

would simply share a common operating picture, passing target data between LPI radars to fuse the data and refine the target. The second method would rely on each radar system transmitting its own signal, but process echoes from the target from its own signal and also process echoes from the other LPI transmitted waveforms. This system could reduce its total transmitted power requirement as it would integrate the returns from the other LPI radars to maintain track on the target. Both cases present a difficult target for anti-radiation missiles.

The study of LPI radars requires two perspectives to be effective. This concept is to ensure that the LPI radar provides an operator with target information while remaining below the threshold of the adversarial ESR ability to identify the LPI radar. The other perspective is that of the operator of the ESR, to identify and locate an adversary's LPI radar. This thesis looks through both "lenses" first by incorporating advances in signal design to a networked LPI system and second by utilizing a networked swarm of UAV equipped with ESR capabilities that incorporate advanced signal processing to identify and locate the adversary's LPI radar.

B. PRINCIPAL CONTRIBUTIONS

The first objective of this thesis is to examine several orthogonal LPI radar waveforms and their vulnerability to the detection by a non-cooperative ESR utilizing time frequency and bi-frequency detection methods. The second objective is to illustrate the concept of swarm theory as applied to a network of UAV equipped with the non-cooperative ESR to show the benefits of a stand-in sensor approach to LPI radar detection.

The orthogonal LPI signals were developed in MATLAB [2] and based on code sequences [3-5] in a program titled "LPI Signal Toolbox" [6], which also includes other contributions by the authors of this thesis. The netted LPI radar signals generated include three orthogonal polyphase coded (OPS) CW waveforms and a discrete frequency coding (DFC) or frequency hopping waveform was simulated.

Radar receiver performance was determined by examining the autocorrelation function (ACF), periodic autocorrelation function (PACF) and periodic ambiguity

function of the LPI waveforms. Non-cooperative receiver processing techniques including the Wigner-Ville Distribution, Quadrature Mirror Filter Bank, and Cyclostationary Spectral Analysis [1] were applied to study how the waveform parameters were revealed in the time-frequency and bi-frequency domains. The concept of swarm theory using a UAV as a stand-in sensor to locate and identify the netted LPI radar systems is studied. The simulation of the radar detecting UAV swarm in Java Code shows the effectiveness of networking a swarm of UAV to enhance detection capability of the netted LPI radar system.

C. THESIS OUTLINE

Chapter II provides a brief description of LPI receiver analysis techniques used and the mathematical principles that govern LPI radar performance. This description is necessary as these techniques quantify the performance of each signal type and allow for a direct comparison of their characteristics.

Chapter III presents the orthogonal netted radar waveforms, a description of their characteristics and the MATLAB$^©$ [2] tool that was used to create the simulated waveform. Receiver characteristics of each waveform are described and compared.

Chapter IV shows the results of the time-frequency and bi-frequency detection techniques used in the ESR.

Chapter V introduces swarm theory and the advantages a UAV Swarm has in detection and location of networked LPI radars.

Chapter VI will contain a brief discussion of the JAVA program code for simulating the UAV swarm, instructions for use of the program, and a battlefield application.

Chapter VII will summarize this thesis and provide recommendations for future research.

THIS PAGE INTENTIONALLY LEFT BLANK

II.   NETTED RADAR RECEIVER ANALYSIS

In this chapter, the signal-to-noise ratio (SNR), the periodic ambiguity function (PAF), and the periodic autocorrelation function (PACF) of a system of netted LPI radars is discussed. The cross correlation function (CCF) used to evaluate the orthogonality of the netted radar waveforms is also discussed.

A.   SIGNAL-TO-NOISE RATIO

The power received by any single radar is:

$$P_r = \frac{P_t G_t G_r \lambda^2 \sigma}{(4\pi)^3 R_t^2 R_r^2} \tag{1}$$

where, P_r is the received power, P_t is the transmitted power, G_t is the transmit antenna gain, G_r is the receive antenna gain, λ is the transmitted signal wavelength, σ is the radar cross section of the target, R_t is the range from the radar transmit antenna to the target, R_r is the range from the target to the receive antenna (the two ranges are equal for a monostatic radar, but in netted radar theory, the transmitter and receiver are often not co-located). The received power also factors into the SNR calculation. The SNR is often used to determine the threshold at which the radar or netted radars will be able to detect an incoming target [9].

In most networked radar systems, the nodes in a network consist of transmitters and receivers that have been engineered to be very similar if not completely alike. Given the likelihood of each node having very similar characteristics, the SNR equation is altered to isolate the immutable parameters from those that can be changed by [9]:

$$SNR_{Netted} = \frac{P_t G_t G_r \sigma \lambda^2 t}{(4\pi)^3 k T_s N_F L} \sum_{i=1}^{m} \sum_{j=1}^{n} \frac{1}{R_{ti}^2 R_{rj}^2} \tag{2}$$

where t is the target integration time in seconds, k is Boltzmann's constant, T_s is the system temperature, N_F is the noise factor of the system, L is the term that incorporates any system losses in the signal processing, m and n are summation indices that account

for all the transmit and receive antennas in the radar network. From this new form of the SNR equation, it is evident that range to the target greatly affects the received SNR. Most radar designs have the ability to adjust transmitted power as needed to acquire their targets at maximum detection range. However, the main premise of LPI radar is to maintain the transmit power at a very low level (on the order of watts or milliwatts) to avoid detection by an adversary intercept receiver. Hence, a target's range is related indirectly to the receive SNR [18].

The ability of netted radars to collectively assess the position of the target due to the multiple received signals is the main advantage over single radars. Given *N* co-operative radars in a battle space, there are *N* possible radar returns that any individual radar in the network can process. Assuming an isotropic radiator as the target and the noise as the primary limiting factor in network performance, the netted SNR Equation (2) normalized to the case of a single radar ($(SNR)_I$) yields [18]:

$$\frac{(SNR)_N}{(SNR)_I} = R^4 \sum_{i=1}^{N} \sum_{j=1}^{N} \frac{1}{R_{ti}^2 R_{rj}^2} \tag{3}$$

This result takes into account the removal of all the common terms in the equation. Assuming that $R_{ti} = R_{rj}$, Equation (3) is proportional to the square of the number of individual radars in the network, or [18]:

$$\frac{(SNR)_N}{(SNR)_I} \propto N^2 \tag{4}$$

B.   THE AMBIGUITY FUNCTION

The ambiguity function (AF) of all the radars in a network can be weighted in order to achieve a more accurate target position. For a simplistic view of this concept, it is assumed that: the noise levels at the receivers are all the same, the transmitted signals and matched filters are all the same signifying a coherent system, the returns from the target are not aspect dependent and therefore the target can be treated as an isotropic radiator. With these assumptions, the weighting factors for all *N* radars in the network can be calculated using the received power equation and comparing that to the maximum

received power by any of the radars in the network. The weighting factor is determined by comparing the received power of one radar Equation (1) with the maximum received power of any radar in the network using

$$w_i = \frac{P_{ri}}{Max(P_r)} \tag{5}$$

with w_i as the weighting factor for the ith radar, and $Max(P_r)$ is the maximum received power of any receiver in the network [9].

The AF is an integral part of the radar's ability to process target detections using a low transmitted power level. The theory behind the AF is the use of a copy of the transmitted signal to identify anomalies (alterations in the transmitted signal) that correspond to potential target echoes. A matched filter is used to process the incoming received signal. The matched filter is directly correlated to the transmitted signal. When the received signal is processed through the matched filter, the differences in the Doppler shift of the received signal correspond to potential target detections. A positive v implies a target is moving towards the radar receiver. A positive range offset τ means the target is further from the radar than the reference value of $\tau = 0$. The ambiguity function should be viewed as the envelope of the matched filter output when the received signal is the input (even this signal is just the transmitted signal with any Doppler shifts that correspond to potential targets). The equation below represents the AF [8]:

$$|\chi(\tau, v)| = \left| \int_{-\infty}^{+\infty} u(t)u^*(t+\tau)e^{j2\pi vt} dt \right| \tag{6}$$

The combination of the weighting factor from Equation (5) and the individual AF results from the individual radars Equation (6) can be summed to provide an overall netted ambiguity for the target or targets of interest [9]:

$$\chi_{netted} = \left| \sum_{i=1}^{N} w_i \chi_i \right|^2 \tag{7}$$

There are three properties of the AF that are the basis of the analyses discussed later in this paper. The first of these defines the origin as the location for the maximum of the AF. This is obtained by normalizing the received signal energy, which in turn

yields a value of unity at the origin $|\chi(\tau,v)| \le |\chi(0,0)| = 1$ [10]. The second property refers to the conservation of the energy of a signal. Specifically, the total volume under the square of the normalized ambiguity surface is equal to unity and is independent of the particular signal's waveform as shown by [10]:

$$\int_{-\infty}^{\infty}\int_{-\infty}^{\infty} |\chi(\tau,v)|^2 \, d\tau dv = 1 \qquad (8)$$

The third property describes the symmetry of the AF with respect to the origin $|\chi(-\tau,-v)| = |\chi(\tau,v)|$ [10]. This allows for the focus of analytical efforts on the two adjacent quadrants of the AF. The analyses and plots will only contain quadrants 1 and 2, which will show the positive Doppler shift values of the received signal.

C.   THE PERIODIC AMBIGUITY FUNCTION

The AF is defined for signals of a finite duration, so it can be surmised that the periodic ambiguity function (PAF) uses multiple periods of the AF and is therefore defined for infinite duration signals. The LPI signals discussed in this paper are CW waveforms, so the PAF will be used to analyze these signals of infinite duration in the same way the AF is used to analyze the pulsed waveforms of finite duration [1]. The PAF is shown below as the normalized response of the matched received that correlates an infinite length of received signal with a reference signal of finite duration. The equation for a single reference code PAF would be a slight modification of the AF Equation (6) [10]:

$$\left|\chi_{T_r}(\tau,v)\right| = \left|\frac{1}{T_r}\int_{0}^{T_r} u(t)u*(t+\tau)e^{j2\pi vt} dt\right| \qquad (9)$$

where $u(t)$ is the received CW signal of infinite duration and T_r is the received signal code period. The reference signal of N' code periods have a PAF as shown below [14]:

$$\left|\chi_{N'T_r}(\tau,v)\right| = \left|\frac{1}{N'T_r}\int_{0}^{N'T_r} u(t)u*(t+\tau)e^{j2\pi vt} dt\right| \qquad (10)$$

8

This is *N'* copies of the reference signal being integrated over the length of the received signal. Using an important relationship between Equation (9) and Equation (10) [14]:

$$\left|\chi_{N'T}(\tau,\nu)\right| = \left|\chi_T(\tau,\nu)\right| \left|\frac{\sin(N'\pi\nu T_r)}{N'\sin(\pi\nu T_r)}\right| \tag{11}$$

This suggests a simplified process to obtain the *N'* period PAF from the single period PAF by multiplying the single period PAF by [14]:

$$\left|\frac{\sin(N'\pi\nu T_r)}{N'\sin(\pi\nu T_r)}\right| \tag{12}$$

D. THE AUTOCORRELATION FUNCTION

The autocorrelation function (ACF) is generally used for signals of finite energy. The incoming signal is detected by the receiver and sent to its matched filter. The received signal, which is the same as the transmitted signal except for any target interactions, is then shifted along the time axis by varying time shifts. During the shifting process of the received signal, the transmitted signal is correlated with the time shifted received signal to identify any anomalies present. These differences of the transmitted and received signals correlated with one another over the time interval defined by the matched filter can be attributed to targets detected by the radar.

$$\left|R(\tau)\right| = \left|\int_{-\infty}^{\infty} u(t)u*(t+\tau)dt\right| = \left|\chi_T(\tau,0)\right| \tag{13}$$

As shown above, there is a unique relationship between the two-dimensional AF with the Doppler shift equal to zero and the ACF. A Doppler shift of zero equates to the equivalent range window of the matched filter in the receiver. This is only a single instance of the matched filter having the same range window as the ACF, but it illustrates the relationship between the two functions and their properties [10].

E. THE PERIODIC AUTOCORRELATION FUNCTION

The PACF is related to the PAF in the same way the ACF is related to the AF. The CW waveforms that are typical of LPI signals are often modulated by a periodic

9

function such as a phase code sequence or a linear frequency ramp function. The equation for the PACF shows its reliance on subcode duration t_b, delay r, and the complex envelope $u(t)$:

$$R(rt_b) = \frac{1}{N_c} \sum_{i=1}^{N_c} u(i)u*(i+r)$$

(14)

The PACF is also inversely proportional to the number of subcodes N_c present in the phase code sequence, which further annotates the distribution of the signal's energy. The PACF is also the zero Doppler cut of the PAF as shown by the relationship $\left|\chi_{NT_r}(\tau, 0)\right| = R(rt_b)$. LPI waveforms can sometimes yield a perfect PACF where the function reaches unity at $\tau = 0, T_r, 2T_r, \dots$ and is zero otherwise [11].

F.   THE CROSS CORRELATION FUNCTION

The CCF has limited use for proving a signal or waveform to be LPI, but its analysis gives a very definite indication of the amount of commonality occurring between two different signals. Consider two different LPI signals used by two or more different netted LPI radars. The orthogonal polyphase signals being studied have the same parameters with respect to the waveform, power level, center frequency, bandwidth, code period, but the one difference is their phase code sequence. It is necessary for the LPI radars to maintain integrity of their signals in order to properly analyze the return signals for possible target detections. A zero cross-correlation shows that one radar's signal will not interfere with the other. Using the equation below, a transmitted signal $u(t)$ and the complex conjugate of a second signal $v(t)$ are multiplied together and integrated over the length of the sequences:

$$R_{uv}(\tau) = \int_{-T_r}^{T_r} u(t)v*(t+\tau)d\tau$$

(15)

10

For CW polyphase signals, the integration is over the length of the code period. It is desirable for the result of the cross-correlation of the two polyphase signals to be zero. This represents an absence of interaction between the two signals. This will be illustrated in the following chapters of this paper [10].

G.   SUMMARY

In summary, the basic principles of signal analysis have been explained. In the next chapter, these principles will be applied to illustrate the performance of the OPS, Optimized OPS, and discrete frequency signals. In addition, the cross-correlation function will be used to show the non-interference characteristics of the orthogonal signals.

THIS PAGE INTENTIONALLY LEFT BLANK

III. LPI WAVEFORMS FOR NETTED RADAR

A. ORTHOGONAL POLYPHASE CODES

Polyphase waveforms have long been employed in LPI radar systems due to the difficulty they introduce in adversarial ESR detection and analysis. Polyphase waveform sequences are identified as a series of phase sequences of finite length (N_c), equal sub-code width (sub-code period, t_b). For each phase sequence, the phase of each sub-code varies in a specific pattern over the length of the sequence. The transmitted signal and antenna bandwidth are not increased by an increase in sequence length; bandwidth (B) is directly related to the carrier frequency f_c and inversely related to the number of cycles per phase (cpp) as shown by Equation(16). The bandwidth is also the inverse of the sub-code period. Code sequences can be designed to be longer to increase their processing gain and their resistance to compromise by adversary ESR without affecting the bandwidth size, although a longer code sequence will necessitate a more complex matched filter [1].

$$B = \frac{f_c}{cpp} = \frac{1}{t_b}$$

(16)

We assume that the orthogonal polyphase code set consists of L signals with each signal containing N_c sub-codes as:

$$s_l(n) = e^{j\varphi(n)} n = 1, 2, ... N_c, l = 1, ... L$$

The orthogonal polyphase waveforms are generally identified as a set (S) with three unique variables. The first variable is the code length (N_c); this length is variable from two to greater than 1000. As the sequence length increases, so does radar performance in terms of auto-correlation side lobe levels decreasing. This performance increase with length is similar to that of other polyphase waveforms to include Frank codes and the P1 - P4 codes [3]. As N_c increases, so does the complexity of the receiver, but the cost of

13

receiver design may outweigh the cost of adversary ESR improvements required to intercept and analyze the longer waveform. Computation time is increased drastically with values of N_c greater than 50 [3].

The second variable is the set size (L), usually from two to eight, but can be larger if required by design. The set size L is the number of codes of length N_c in a set. The value of L as applied to netted LPI radars determines the number of radar sites in the multisite radar system. The main complication with an increase value of L is the complex computation required to produce the final orthogonal polyphase waveform set S. For the same code length N_c it has been shown that the radar performance does not degrade as the set size L is increased [3].

The third variable to describe an orthogonal polyphase waveform is the number of admissible phase values (M) in the code sequence. The values are determined by the following general equation:

$$\phi(n) \in \{0, \frac{2\pi}{M}, 2\frac{2\pi}{M}, ..., (M-1)\frac{2\pi}{M}\} = \{\psi_1, \psi_2, ... \psi_M\} \tag{17}$$

Using this equation for a value of 4, the choice of phase values would be: $0, \frac{\pi}{2}, \pi, and \frac{3\pi}{2}$ and as the value of admissible phase values M increases so does the complexity of the receiver. Equation (18) illustrates a polycode phase set in an L by N_c phase matrix [3].

$$S(L, N_c, M) = \begin{bmatrix} \phi_1(1), \phi_1(2), \phi_1(3), ...\phi_1(N_c) \\ \phi_2(1), \phi_2(2), \phi_2(3), ...\phi_2(N_c) \\ \vdots \\ \phi_L(1), \phi_L(2), \phi_L(3), ...\phi_L(N_c) \end{bmatrix} \tag{18}$$

Once the values of L, N_c, and M are established the next step in the process is to determine the code sets in the form of a phase matrix. The matrix will consist of L sets of phase sequences of length N_c. The method to determine the each phase value in the phase sequence is called simulated annealing (SA) algorithm. SA is required in the determination of multiple long phase sequences with low cross-correlation because algebraic determination of greater than two sequences is very difficult. SA was initially

14

designed for VLSI circuit design. The algorithm is an optimization algorithm with the benefit of not becoming fixed on local optima during the search process [3].

The optimization process is based on the comparison of two properties of the OPS, the autocorrelation and the cross correlation. Specifically the code set must satisfy or nearly satisfy the ACF and CCF shown in discrete form in Equations (19) and (20).

$$A(s_l, k) = \begin{cases} \dfrac{1}{N_c} \displaystyle\sum_{n=1}^{N_c-k} s_l(n)s_l^*(n+k) = 0, 0 < k < N_c \\ \dfrac{1}{N_c} \displaystyle\sum_{n=-k+1}^{N} s_l(n)s_l^*(n+k) = 0, -N_c < k < 0 \end{cases} \quad l = 1,2,...L \qquad (19)$$

$$C(s_p, s_q, k) = \begin{cases} \dfrac{1}{N_c} \displaystyle\sum_{n=1}^{N_c-k} s_p(n)s_q^*(n+k) = 0, 0 < k < N_c \\ \dfrac{1}{N_c} \displaystyle\sum_{n=-k+1}^{N_c} s_p(n)s_q^*(n+k) = 0, -N_c < k < 0 \end{cases} \quad p \neq q, l = 1,2,...L \qquad (20)$$

The basic cost function is given by Equation (21). The variable λ is a weighting coefficient between the ACF and the CCF in the cost function. The principle of the function is to minimize the ACF sidelobe peaks and the CCF peaks. During the process using Equation (21) it is possible to obtain larger autocorrelation sidelobe levels with increased code length. Because of this a better optimization technique is to minimize total ACF sidelobe energy and CCF energy. This is shown in Equation (22).

$$E_1 = \sum_{l=1}^{L} \max |A(\phi_l, k)| + \lambda \sum_{p=1}^{L-1} \sum_{q=p+1}^{L} \max |C(\phi_p, \phi_q, k)|, k \neq 0 \qquad (21)$$

$$E_T = \sum_{l=1}^{L} \sum_{k=1}^{N_c-1} |A(\phi_l, k)|^2 + \lambda \sum_{p=1}^{L-1} \sum_{q=p+1}^{L} \sum_{k=-(N_c-1)}^{N_c-1} |C(\phi_p, \phi_q, k)|^2 \qquad (22)$$

Given the predetermined values of L, M, and N_c, the minimization of Equation (22) using SA will generate a group of polyphase sequences that are automatically constrained by Equation (19) and Equation (20) [3].

The four basic steps of the SA process are as follows:

- Step 1: Choose initial values of L, M, and N_c.

15

- Step 2: Choose annealing temperature. The initial starting temperature is based on the standard deviation of the initial cost distribution. This distribution is determined by sampling the number set produced by Equation (17) and illustrated by Equation(18).

- Step 3: Start the annealing process by "perturbing" the phase coding by randomly choosing a coding sequence from the waveform set. If the cost is reduced by the perturbation it will be accepted, if it increases it maybe accepted if it is within a probability tolerance based on the cost change and the current annealing temperature. This process is repeated until the standard deviation of the cost values becomes stable at the annealing temperature. Then the annealing temperature is changed until the standard deviation of the cost values becomes stable again.

- Step 4: Stop the process when the cost is not reduced over the period of three consecutive temperature reductions [3].

1. Orthogonal Polyphase Sequence of 40 Sub-codes

a. *Waveform Description*

The orthogonal polyphase sequence code with 40 sub-codes (OPS 40) was designed with the following initial values, $N_c = 40$, $L = 4$, and $M = 4$. There are $L = 4$ code sets associated with this particular design. The $M = 4$ available phases are $0, \frac{\pi}{2}, \pi, and \frac{3\pi}{2}$. The MATLAB$^©$ [2] code allows for user selection of all variables in the Table 1. To prevent confusion and aid the user in creation analysis of signals a naming convention was established for the OPS 40 code. The OPS 40 code file names begin with "O 40 4 4" (OPS "N" "L" "M"). They are followed by the code set number (i.e. C1), the carrier frequency (in kHz), the sampling frequency (in kHz), the code length, the number of cycles per phase, and finally the SNR (in dB, or "s" for signal only).

16

The OPS 40 code is selected as it is short enough that the algorithm used to generate it does not require a significant computation time, yet it is long enough that its performance exceeds that of shorter code lengths. The OPS 40 code set is displayed in Table 2. Each code sequence is listed vertically ($L = 4$) and the sub-code index is listed horizontally ($N_c = 40$) to show the difference in phase value between each sub-code in each sequence. The multiplier value to get the phase code value in radians is also shown in Table 2. This increased diversity provides an inherent invulnerability to the non-cooperative ESR and due to the nature of polyphase codes does not increase the signal bandwidth that is governed by the bit sub-code period [7]. The OPS 40 codes were generated for testing with the following characteristics shown in Table 1:

Specific Signal Identification: O 40 4 4 C1-1-7-40-1-s	
Carrier frequency (f_c)	1000 Hz
Sampling frequency (f_s)	7000 Hz
Number of phases	40
SNR	Signal Only
Number of cycles per phase	1
Number of potential signals in the set	4

Table 1.   OPS 40 Signal Characteristics.

17

	Code 1		Code 2		Code 3		Code 4	
Index	$x \times \pi$	Rad	$x \times \pi$	Rad	$x \times \pi$	Rad	$x \times \pi$	Rad
1	0.50	1.57	1.50	4.71	1.50	4.71	0.50	1.57
2	0.00	0.00	1.00	3.14	0.00	0.00	0.50	1.57
3	0.00	0.00	1.00	3.14	0.50	1.57	0.00	0.00
4	1.50	4.71	1.00	3.14	0.50	1.57	0.00	0.00
5	0.50	1.57	0.50	1.57	1.50	4.71	0.00	0.00
6	1.50	4.71	0.00	0.00	0.50	1.57	0.50	1.57
7	1.50	4.71	0.00	0.00	1.50	4.71	1.50	4.71
8	0.50	1.57	0.50	1.57	1.00	3.14	1.00	3.14
9	0.50	1.57	0.50	1.57	0.50	1.57	1.50	4.71
10	1.00	3.14	1.50	4.71	0.50	1.57	1.00	3.14
11	0.50	1.57	0.00	0.00	0.50	1.57	0.00	0.00
12	0.50	1.57	0.50	1.57	0.50	1.57	1.50	4.71
13	1.50	4.71	1.00	3.14	0.50	1.57	1.50	4.71
14	1.50	4.71	0.50	1.57	1.00	3.14	0.00	0.00
15	1.00	3.14	1.00	3.14	1.00	3.14	1.00	3.14
16	0.50	1.57	1.00	3.14	0.50	1.57	0.00	0.00
17	0.50	1.57	0.50	1.57	0.00	0.00	0.00	0.00
18	1.50	4.71	1.50	4.71	0.50	1.57	0.50	1.57
19	0.00	0.00	0.00	0.00	1.50	4.71	1.50	4.71
20	1.00	3.14	0.50	1.57	1.00	3.14	1.50	4.71
21	0.00	0.00	1.50	4.71	0.50	1.57	0.50	1.57
22	1.50	4.71	0.50	1.57	1.50	4.71	1.50	4.71
23	0.50	1.57	0.50	1.57	0.00	0.00	0.00	0.00
24	0.50	1.57	1.50	4.71	1.00	3.14	0.50	1.57
25	1.00	3.14	0.50	1.57	0.50	1.57	0.00	0.00
26	1.50	4.71	0.00	0.00	0.00	0.00	1.50	4.71
27	1.50	4.71	0.00	0.00	0.00	0.00	0.00	0.00
28	1.50	4.71	1.50	4.71	1.00	3.14	0.00	0.00
29	0.50	1.57	0.50	1.57	0.00	0.00	0.50	1.57
30	1.50	4.71	0.50	1.57	1.00	3.14	0.50	1.57
31	1.50	4.71	1.00	3.14	1.00	3.14	1.00	3.14
32	1.50	4.71	1.00	3.14	0.50	1.57	1.50	4.71
33	1.00	3.14	1.50	4.71	1.00	3.14	0.50	1.57
34	0.50	1.57	0.50	1.57	1.00	3.14	0.50	1.57
35	1.00	3.14	1.50	4.71	1.50	4.71	0.00	0.00
36	1.00	3.14	0.50	1.57	0.50	1.57	1.50	4.71
37	1.00	3.14	1.50	4.71	0.00	0.00	0.50	1.57
38	1.00	3.14	0.50	1.57	0.00	0.00	1.00	3.14
39	1.50	4.71	1.00	3.14	1.50	4.71	1.00	3.14
40	0.50	1.57	0.50	1.57	0.00	0.00	1.00	3.14

Table 2.   OPS Sequences with $N_c = 40$, $L = 4$, $M = 4$ (from [3]).

18

b.   *Waveform Characteristics from Simulation*

Figure 1 shows the power spectral density (PSD) versus frequency of the OPS 40 modulation code set #1 with $N_c = 40$. Figure 2 shows the discrete phase values for the OPS 40 modulation code set #1 with $N_c = 40$. The four phase values are readily apparent. Figure 3 shows the complex signal phase shift for the OPS 40 modulation code set #1. This plot best illustrates the different signal characteristics between the different code sets. The carrier frequency is $f_c = 1$ kHz, $f_s = 7$ kHz, and *cpp* = 1. All three plots were generated with the LPIT.
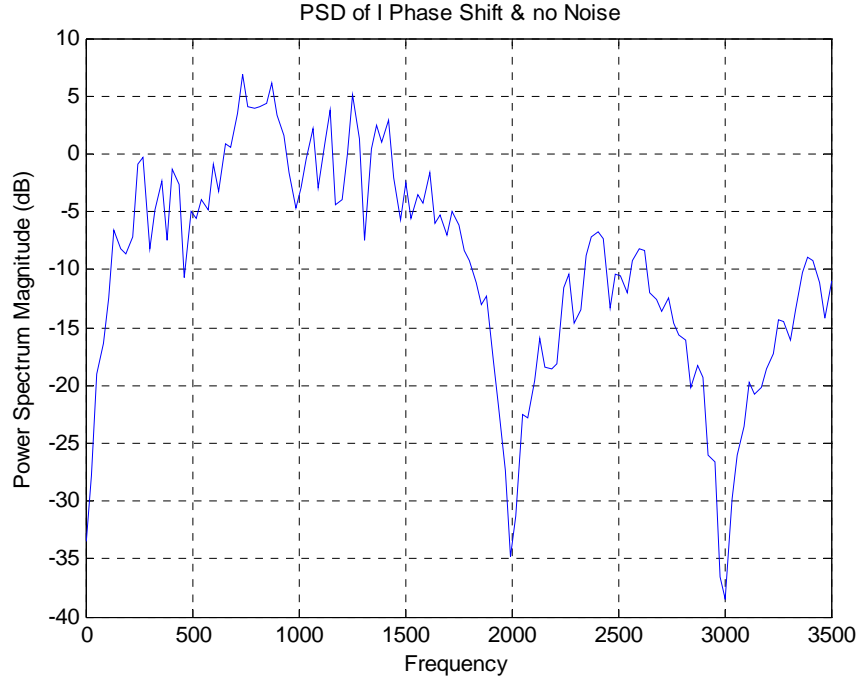
Figure 1.   Power Spectral Density of OPS Sequence
with $N_c = 40$, $L = 4$, $M = 4$ Code Set 1 (Signal only).

Figure 2.   OPS Sequence with $N_c = 40$, $L = 4$, $M = 4$ Code Set 1
showing one period of phase shifts (radians).

Figure 3.   OPS Sequence with $N_c = 40$, $L = 4$, $M = 4$ Code Set 1
showing five periods of phase shifts (degrees).

20
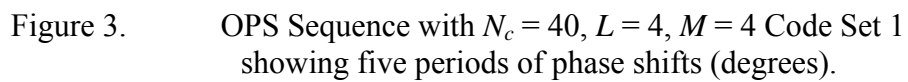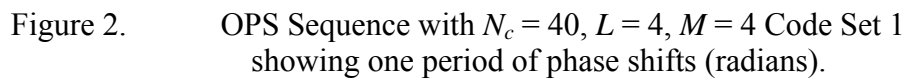
Figure 4 shows the PSD versus frequency of the OPS 40 modulation code set #2 with $N_c = 40$. Figure 5 shows the discrete phase values of the OPS 40 modulation code set #2 with $N_c = 40$. The four phase values are readily apparent. Figure 6 shows the "I + jQ" phase shift for the OPS 40 modulation code set #2. This plot best illustrates the different signal characteristics between the different code sets. The carrier frequency is $f_c = 1\,\text{kHz}$, $f_s = 7\,\text{kHz}$, and $cpp = 1$. All three plots were generated with the LPIT.
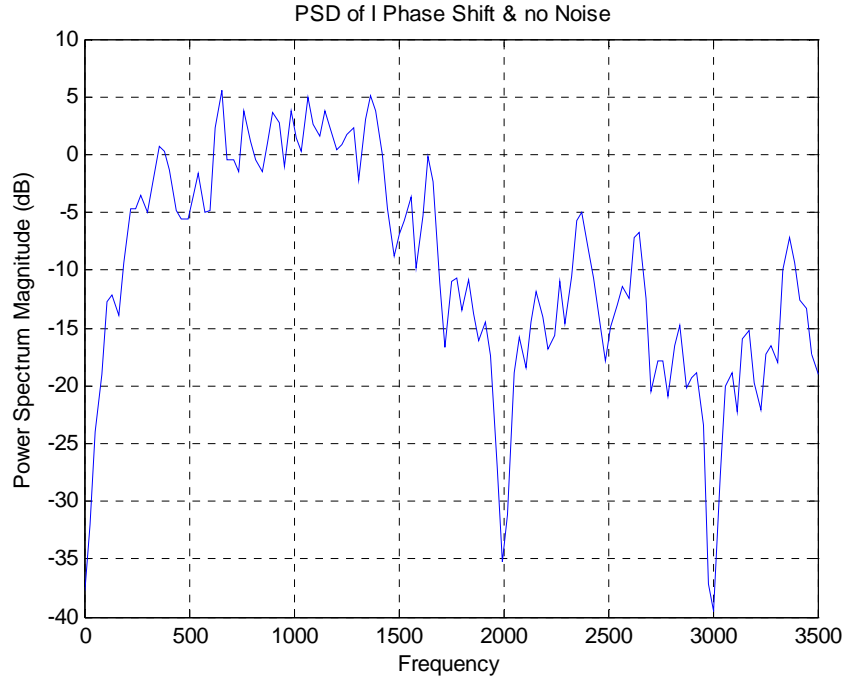
Figure 4. Power Spectral Density of OPS Sequence
with $N_c = 40$, $L = 4$, $M = 4$ Code Set 2 (Signal only).
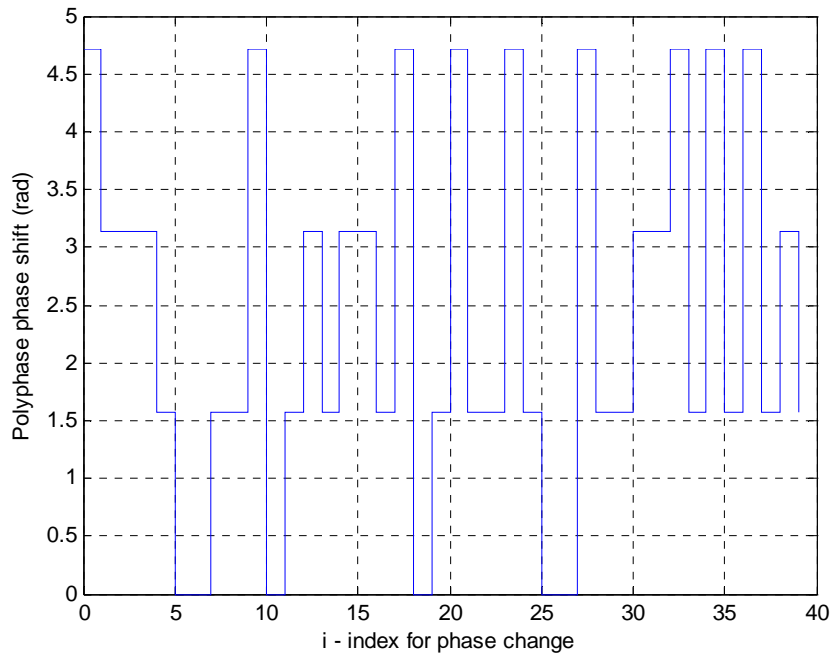
Figure 5.   OPS Sequence with $N_c = 40$, $L = 4$, $M = 4$ Code Set 2
showing one period of phase shifts (radians).
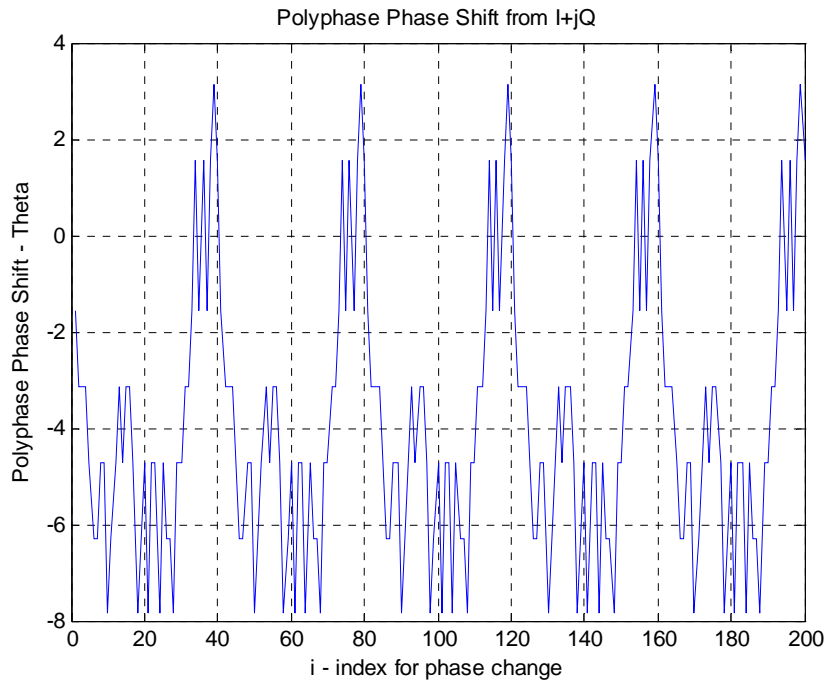
Figure 6.   OPS Sequence with $N_c = 40$, $L = 4$, $M = 4$ Code Set 2
showing five periods of phase shifts (degrees).

22

Figure 7 shows the PSD versus frequency of the OPS 40 modulation code set #3 with $N_c = 40$. Figure 8 shows the discrete phase values for the OPS 40 modulation code set #3 with $N_c = 40$. The four phase values are readily apparent. Figure 9 shows the "I + jQ" phase shift for the OPS 40 modulation code set #3, this plot best illustrates the different signal characteristics between the different code sets. The carrier frequency is $f_c = 1\,\text{kHz}$, $f_s = 7\,\text{kHz}$, and $cpp = 1$. All three plots were generated with the LPIT.
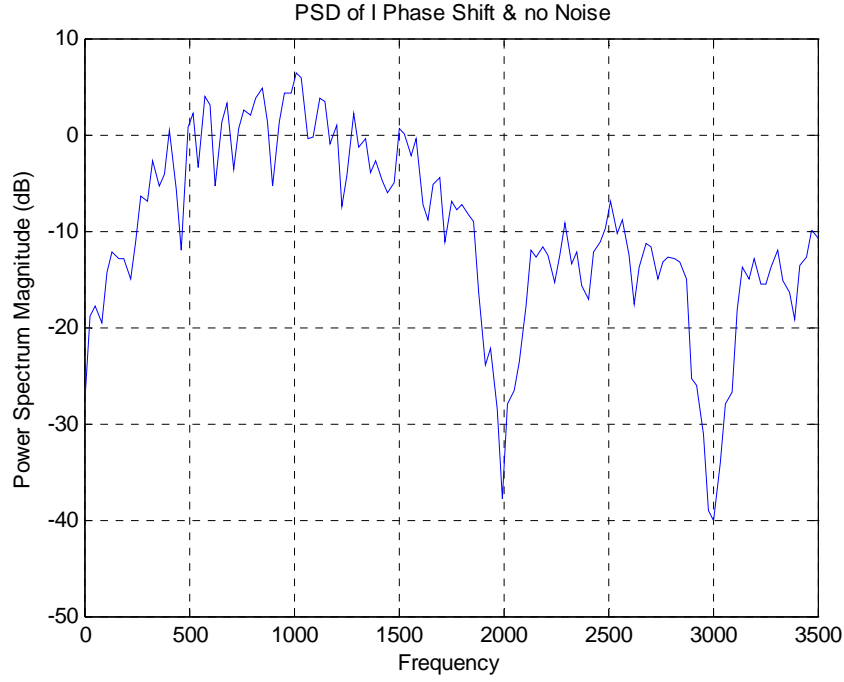
Figure 7.   Power Spectral Density of OPS Sequence with $N_c = 40$, $L = 4$, $M = 4$ Code Set 3 (Signal only).
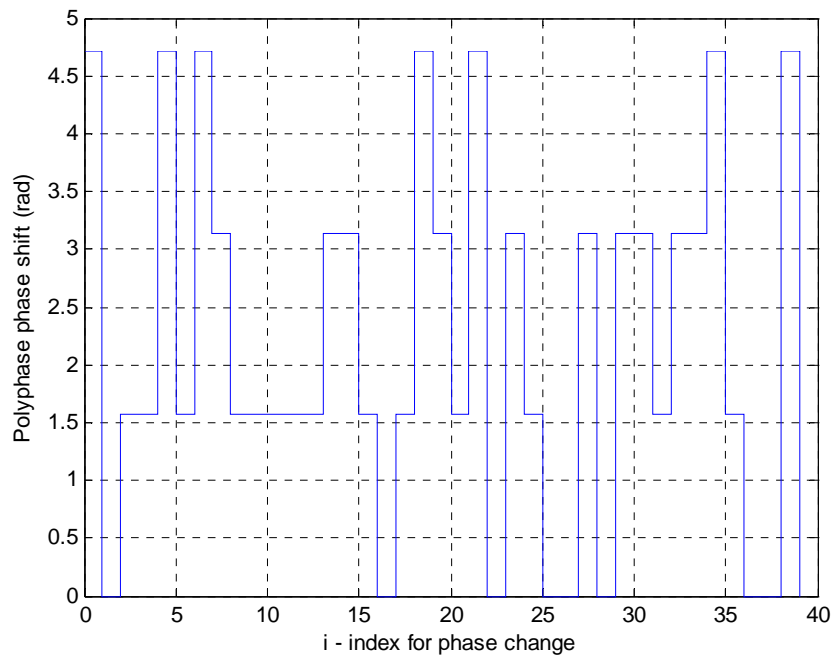
Figure 8.   OPS Sequence with $N_c = 40$, $L = 4$, $M = 4$ Code Set 3 showing one period of phase shifts (radians).
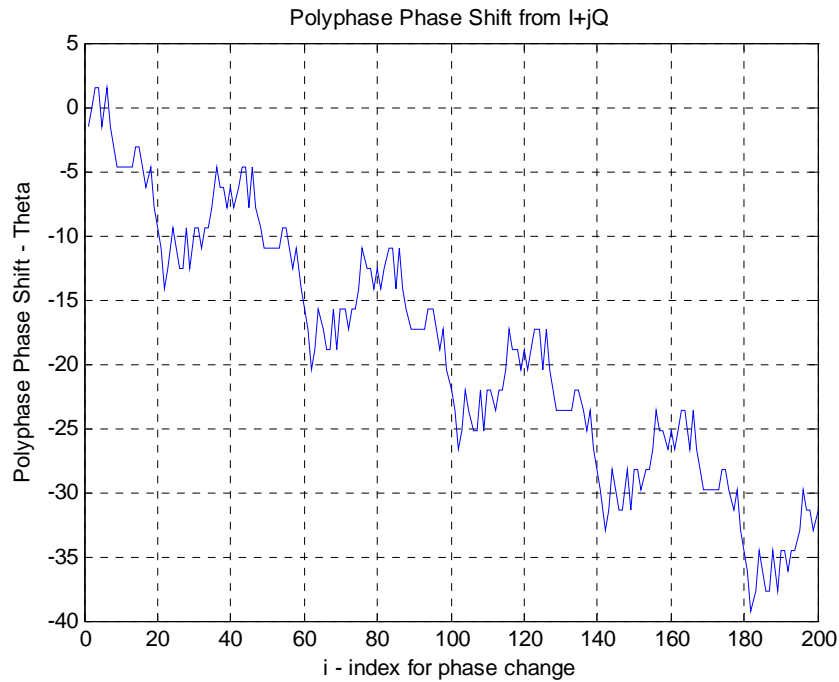
Figure 9.   OPS Sequence with $N_c = 40$, $L = 4$, $M = 4$ Code Set 3 showing five periods of phase shifts (degrees).

Figure 10 shows the PSD versus frequency of the OPS 40 modulation code set #4 with $N_c = 40$. Figure 11 shows the discrete phase values for the OPS 40 modulation code set #4 with $N_c = 40$. The four phase values are readily apparent. Figure 12 shows the "I + jQ" phase shift for the OPS 40 modulation code set #4, this plot best illustrates the different signal characteristics between the different code sets. The carrier frequency is $f_c = 1\,\text{kHz}$, $f_s = 7\,\text{kHz}$, and $cpp = 1$. All three plots were generated with the LPIT.
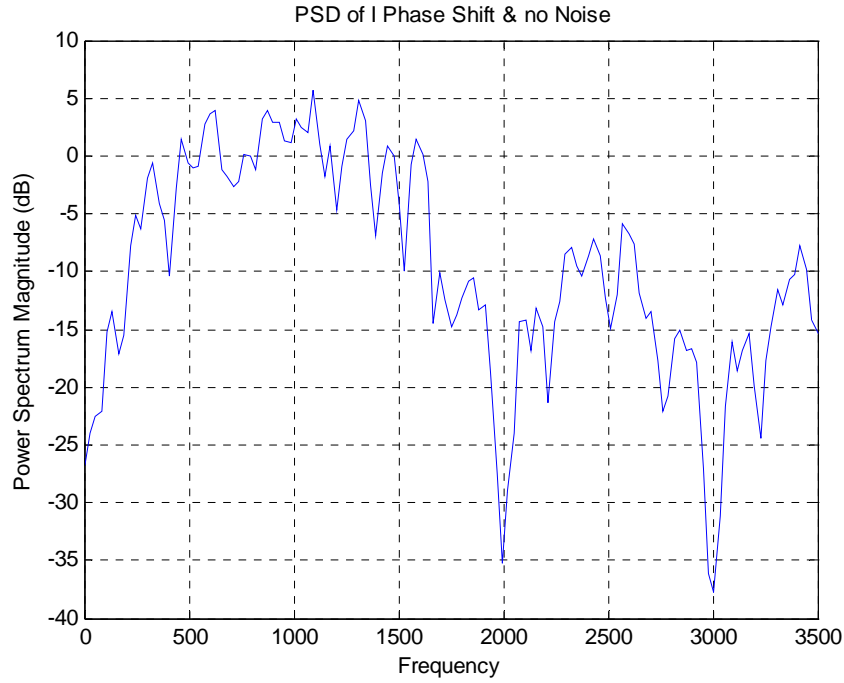
Figure 10.   Power Spectral Density of OPS Sequence
with $N_c = 40$, $L = 4$, $M = 4$ Code Set 4 (Signal only).

Figure 11.   OPS Sequence with $N_c = 40$, $L = 4$, $M = 4$ Code Set 4 showing one period of phase shifts (radians).

Figure 12.   OPS Sequence with $N_c = 40$, $L = 4$, $M = 4$ Code Set 4 showing five periods of phase shifts (degrees).
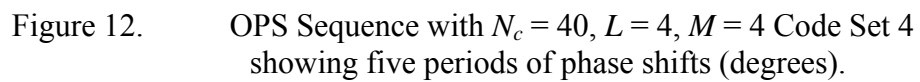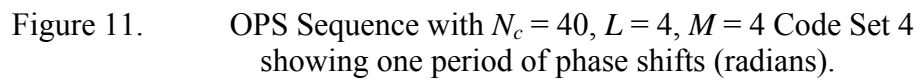
Figure 13 (top plot) shows the normalized ACF and the corresponding sidelobe structure for the OPS 40 code set #1. The offset τ is also normalized by the sub-code period t_b. The peak sidelobe level (PSL) can be seen at approximately $-16\,\text{dB}$ from the peak [3]. Figure 13 (bottom plot) shows the PACF. Figure 14 shows the PAF. Based on the signal parameters $f_c = 1\,\text{kHz}$, $f_s = 7\,\text{kHz}$, and *cpp* = 1 and using Equation (23) the PAF repeats every code period as shown by [1]:

$$b_{sc} = N_c \left(cpp * \frac{fs}{fc} \right) = 280 \text{ samples} \tag{23}$$

All three plots were generated with ambfn7 [16].
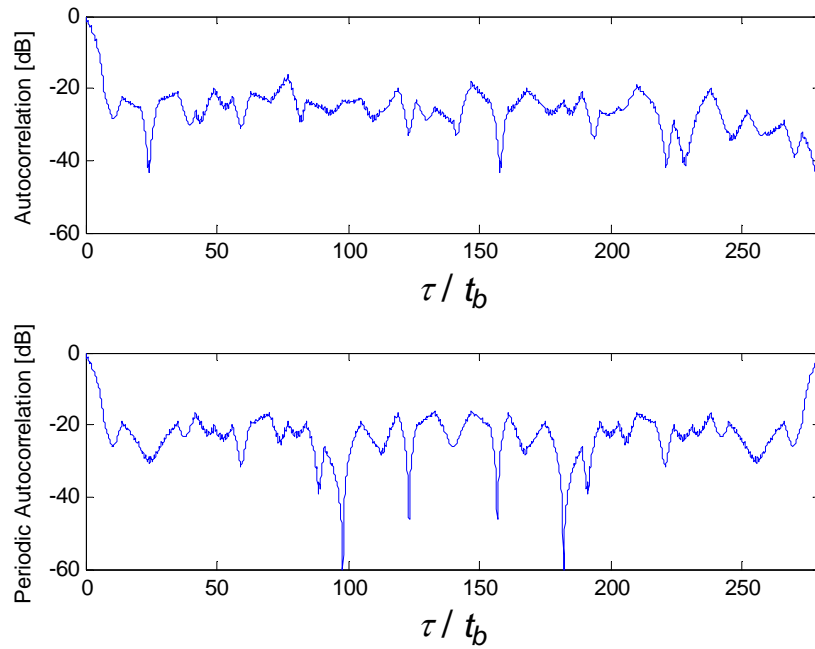
Figure 13.   OPS Sequence with $N_c = 40$, $L = 4$, $M = 4$ Code Set 1 ACF (top) and PACF (bottom).
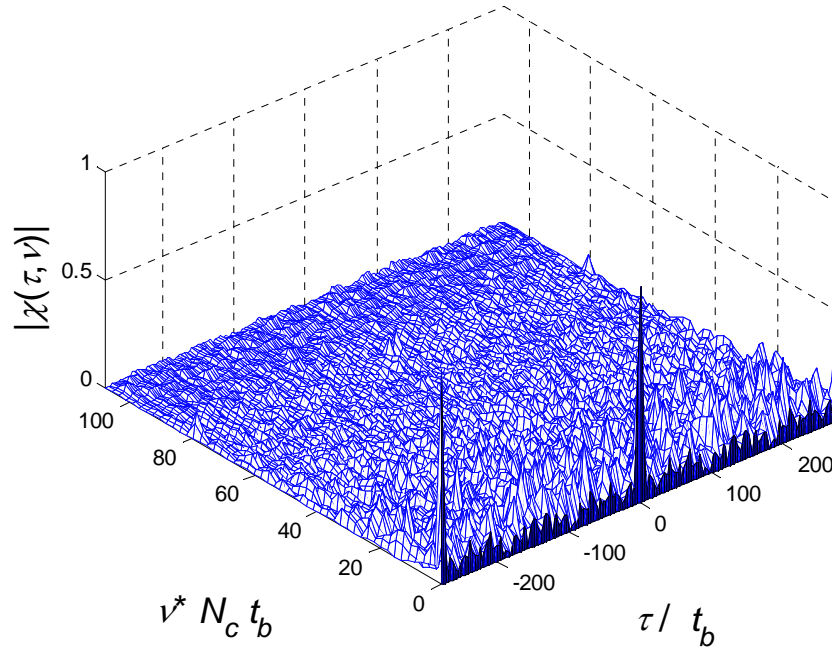
Figure 14.　　OPS Sequence with $N_c = 40$, $L = 4$, $M = 4$ Code Set 1
Periodic Ambiguity Function Plot.

To illustrate the non-interference nature of the OPS 40 signal the CCF was calculated for all six possible combinations of signals that would be utilized by a networked LPI radar system with four nodes. Each would be transmitting its own code set. Theoretically there would be no interference between each different code sets using similar signal parameters. Figure 15 shows the CCF for the OPS 40 code set #1 and code set #2 on the left contrasted with the ACF of OPS 40 code set #1 on the right. Figure 16 shows the CCF for the OPS 40 code set #2 and code set #3 on the left contrasted with the ACF of OPS 40 code set #2 on the right. Figure 17 shows the CCF for the OPS 40 code set #3 and code set #4 on the left contrasted with the ACF of OPS 40 code set #3 on the right. Figure 18 shows the CCF for the OPS 40 code set #4 and code set #1 on the left contrasted with the ACF of OPS 40 code set #4 on the right. Figure 19 shows the CCF for the OPS 40 code set #4 and code set #2 on the left contrasted with the ACF of OPS 40 code set #4 on the right. Figure 20 shows the CCF for the OPS 40 code set #3 and code set #1 on the left contrasted with the ACF of OPS 40 code set #3 on the right.

28

O 40 4 4 C1-1-7-40-1-s
cross-corr with
O 40 4 4 C2-1-7-40-1-s

ACF
O 40 4 4 C1-1-7-40-1-s
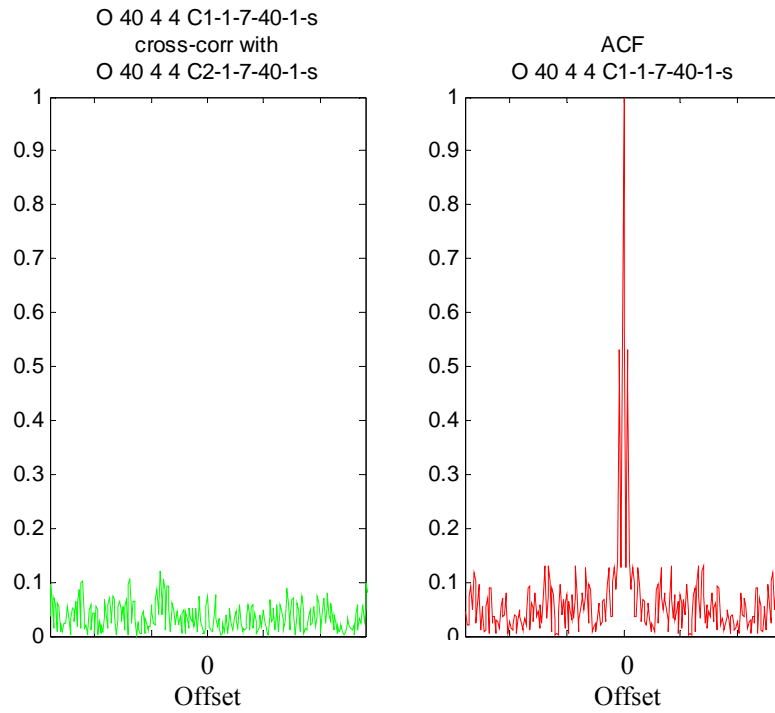
Figure 15.   OPS 40 Codes 1 and 2 CCF Plot (Left) and Code 1 ACF Plot (Right).

O 40 4 4 C2-1-7-40-1-s
cross-corr with
O 40 4 4 C3-1-7-40-1-s

ACF
O 40 4 4 C2-1-7-40-1-s
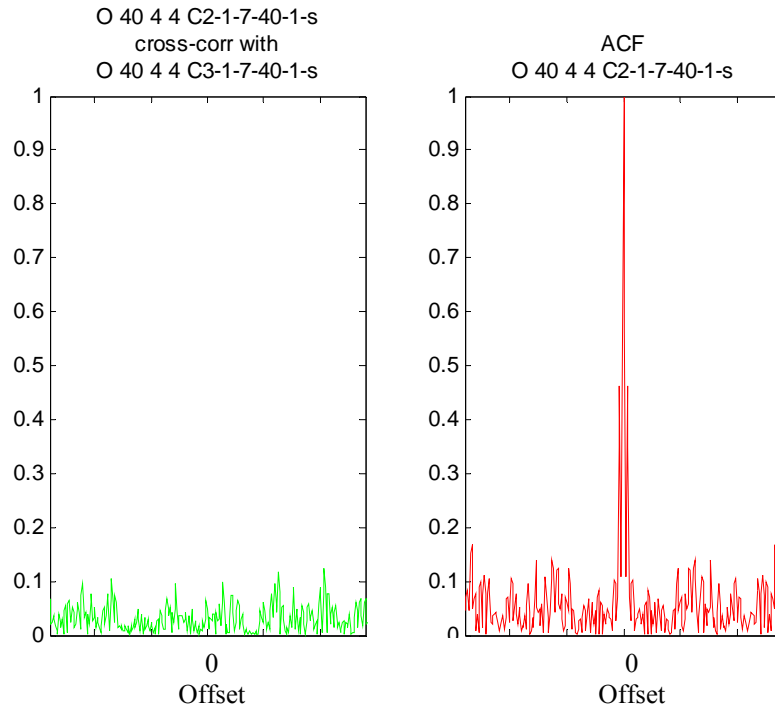
Figure 16.   OPS 40 Codes 2 and 3 CCF Plot (Left) and Code 2 ACF Plot (Right).

29
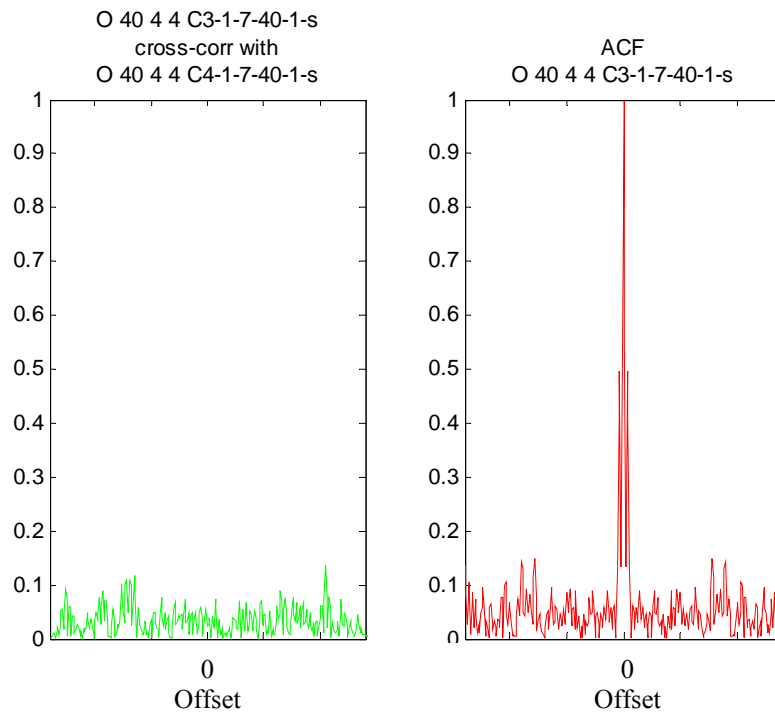
Figure 17.   OPS 40 Codes 3 and 4 CCF Plot (Left) and Code 3 ACF Plot (Right).
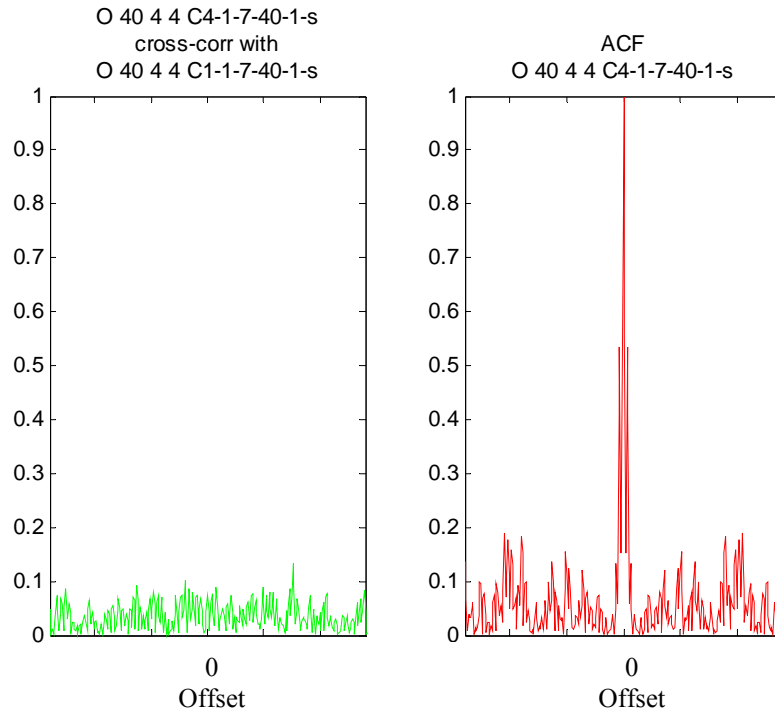
Figure 18.   OPS 40 Codes 4 and 1 CCF Plot (Left) and Code 4 ACF Plot (Right).
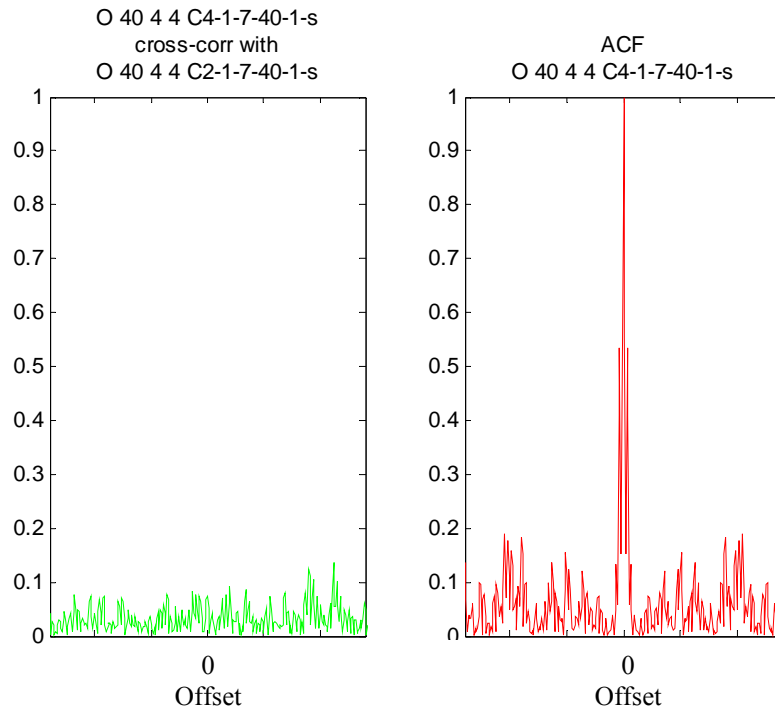
Figure 19.   OPS 40 Codes 4 and 2 CCF Plot (Left) and Code 4 ACF Plot (Right).
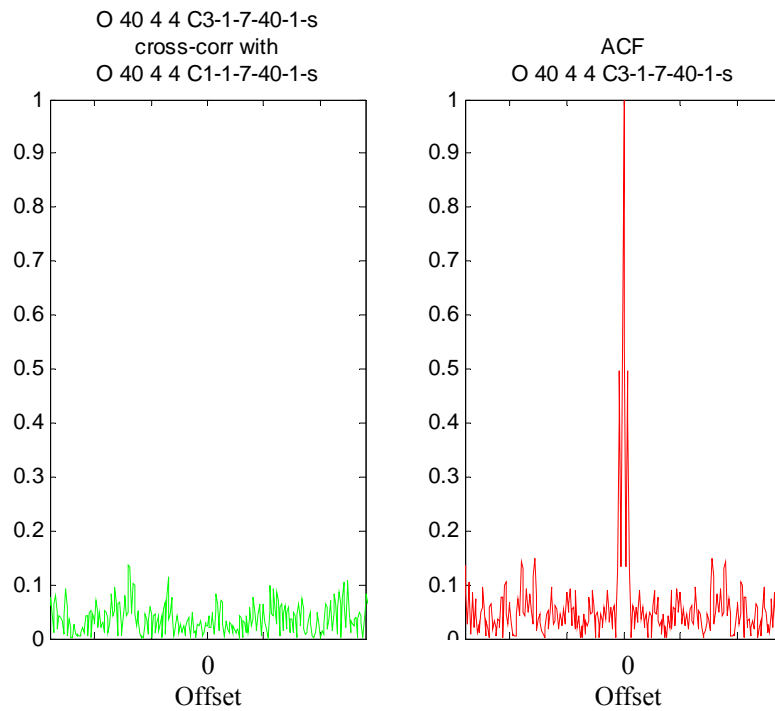
Figure 20.   OPS 40 Codes 3 and 1 CCF Plot (Left) and Code 3 ACF Plot (Right).

2. Orthogonal Polyphase Sequence of 128 Sub-codes

a. *Waveform Description*

The orthogonal polyphase sequence code with 128 sub-codes (OPS 128) was designed with the following initial values, N_c = 128, L = 3, and M = 4. There are three code sets associated with this particular design. The four available phases are $0, \dfrac{\pi}{2}, \pi, and \dfrac{3\pi}{2}$. The MATLAB$^{©}$ [2] code allows for user selection of all variables in the Table 3. To prevent confusion and aid the user in creation and analysis of signals a naming convention was established for the OPS 128 code. The entire OPS 128 code file names begin with O 128 3 4 (O "N" "L" "M"). They are followed by the code set number (i.e. C1), the carrier frequency (in kHz), the sampling frequency (in kHz), the code length, the number of cycles per phase, and finally the SNR (in dB, or "s" for signal only).

The OPS 128 code is much longer than the OPS 40 code. There is one less code set (L=3 vice L=4) reducing the computation time for signal design. It is much longer and its performance far exceeds that of shorter code lengths. The OPS 128 code is displayed in Table 4. Each code sequence is listed vertically (L = 3) and the sub-code index is listed horizontally (N_c = 128) to show the difference in phase value between each sub-code in each sequence. This increased diversity provides an increased invulnerability to non-cooperative ESR and due to the nature of polyphase codes does not increase the signal bandwidth that is governed by the sub-code period [7].

32

The OPS 128 codes were generated for testing with the following characteristics shown in Table 3:

Specific Signal Identification: O 128 3 4 C1-1-7-128-1-s	
Carrier frequency (f_c)	1000 Hz
Sampling frequency (f_s)	7000 Hz
Number of phases	128
SNR	Signal Only
Number of cycles per phase	1
Number of potential signals in the set	3

Table 3.   OPS 128 Signal Characteristics.

#	Code 1 x*pi	Rad	Code 2 x*pi	Rad	Code 3 x*pi	Rad	#	Code 1 x*pi	Rad	Code 2 x*pi	Rad	Code 3 x*pi	Rad	#	Code 1 x*pi	Rad	Code 2 x*pi	Rad	Code 3 x*pi	Rad
1	1.5	4.71	0.0	0.00	1.5	4.71	43	1.0	3.14	0.0	0.00	1.0	3.14	85	0.0	0.00	1.5	4.71	1.5	4.71
2	1.5	4.71	0.5	1.57	1.0	3.14	44	1.0	3.14	0.0	0.00	0.0	0.00	86	0.0	0.00	0.5	1.57	1.5	4.71
3	1.5	4.71	1.0	3.14	0.0	0.00	45	0.0	0.00	0.0	0.00	1.0	3.14	87	0.5	1.57	1.0	3.14	0.0	0.00
4	1.5	4.71	1.0	3.14	0.0	0.00	46	1.5	4.71	1.5	4.71	1.5	4.71	88	0.5	1.57	0.5	1.57	0.5	1.57
5	0.0	0.00	0.0	0.00	1.0	3.14	47	1.5	4.71	1.0	3.14	0.0	0.00	89	1.0	3.14	0.5	1.57	1.0	3.14
6	0.0	0.00	1.5	4.71	1.5	4.71	48	1.0	3.14	1.5	4.71	0.0	0.00	90	0.5	1.57	1.0	3.14	0.0	0.00
7	0.0	0.00	1.5	4.71	0.0	0.00	49	0.0	0.00	1.0	3.14	1.0	3.14	91	1.0	3.14	1.5	4.71	1.5	4.71
8	1.5	4.71	0.5	1.57	0.0	0.00	50	1.5	4.71	1.5	4.71	0.5	1.57	92	0.5	1.57	0.0	0.00	1.5	4.71
9	0.0	0.00	1.5	4.71	0.0	0.00	51	1.0	3.14	1.5	4.71	1.0	3.14	93	1.5	4.71	0.5	1.57	1.0	3.14
10	1.5	4.71	0.5	1.57	0.0	0.00	52	1.5	4.71	0.0	0.00	0.0	0.00	94	0.0	0.00	0.0	0.00	1.5	4.71
11	0.0	0.00	1.5	4.71	1.0	3.14	53	1.5	4.71	1.0	3.14	1.5	4.71	95	0.5	1.57	0.5	1.57	1.5	4.71
12	1.5	4.71	0.0	0.00	1.0	3.14	54	0.0	0.00	0.0	0.00	0.0	0.00	96	1.0	3.14	1.5	4.71	1.0	3.14
13	0.0	0.00	0.5	1.57	1.5	4.71	55	1.0	3.14	1.0	3.14	1.0	3.14	97	0.5	1.57	0.0	0.00	1.5	4.71
14	0.0	0.00	0.0	0.00	0.5	1.57	56	1.0	3.14	0.5	1.57	0.0	0.00	98	0.0	0.00	0.5	1.57	1.0	3.14
15	1.5	4.71	0.5	1.57	1.5	4.71	57	0.0	0.00	0.5	1.57	0.5	1.57	99	1.0	3.14	1.5	4.71	0.5	1.57
16	1.5	4.71	0.5	1.57	1.5	4.71	58	1.0	3.14	0.5	1.57	0.5	1.57	100	1.0	3.14	1.5	4.71	1.5	4.71
17	0.5	1.57	0.0	0.00	0.0	0.00	59	0.5	1.57	1.6	4.87	1.0	3.14	101	1.0	3.14	0.5	1.57	0.0	0.00
18	1.5	4.71	0.0	0.00	0.0	0.00	60	0.5	1.57	0.0	0.00	0.0	0.00	102	1.5	4.71	1.5	4.71	0.5	1.57
19	1.0	3.14	1.0	3.14	1.0	3.14	61	0.5	1.57	1.5	4.71	1.0	3.14	103	0.0	0.00	1.5	4.71	0.5	1.57
20	0.0	0.00	1.0	3.14	0.5	1.57	62	1.5	4.71	1.0	3.14	1.5	4.71	104	0.0	0.00	0.0	0.00	1.0	3.14
21	0.0	0.00	1.5	4.71	0.5	1.57	63	0.0	0.00	1.5	4.71	1.0	3.14	105	1.5	4.71	1.0	3.14	0.5	1.57
22	0.0	0.00	1.5	4.71	0.0	0.00	64	1.5	4.71	0.0	0.00	0.5	1.57	106	1.5	4.71	1.0	3.14	0.5	1.57
23	0.0	0.00	1.0	3.14	0.5	1.57	65	0.5	1.57	1.5	4.71	0.0	0.00	107	0.5	1.57	1.5	4.71	0.5	1.57
24	1.5	4.71	0.0	0.00	1.5	4.71	66	1.0	3.14	1.0	3.14	1.5	4.71	108	0.5	1.57	1.5	4.71	0.5	1.57
25	0.5	1.57	1.5	4.71	0.0	0.00	67	0.0	0.00	1.0	3.14	1.5	4.71	109	0.0	0.00	0.5	1.57	0.5	1.57
26	1.0	3.14	0.5	1.57	1.0	3.14	68	1.0	3.14	0.5	1.57	1.0	3.14	110	0.5	1.57	1.0	3.14	1.5	4.71
27	1.5	4.71	0.0	0.00	0.0	0.00	69	1.5	4.71	0.0	0.00	1.0	3.14	111	0.0	0.00	0.0	0.00	1.0	3.14
28	0.5	1.57	1.5	4.71	1.0	3.14	70	1.0	3.14	0.0	0.00	0.5	1.57	112	0.0	0.00	1.0	3.14	1.0	3.14
29	0.5	1.57	1.0	3.14	1.0	3.14	71	0.0	0.00	1.5	4.71	0.5	1.57	113	1.0	3.14	1.0	3.14	1.5	4.71
30	1.5	4.71	1.5	4.71	1.5	4.71	72	1.0	3.14	1.0	3.14	0.0	0.00	114	1.0	3.14	1.5	4.71	0.5	1.57
31	0.5	1.57	0.5	1.57	0.0	0.00	73	1.0	3.14	0.0	0.00	1.0	3.14	115	1.5	4.71	1.5	4.71	0.0	0.00
32	1.5	4.71	0.0	0.00	0.0	0.00	74	0.0	0.00	0.5	1.57	0.0	0.00	116	1.5	4.71	1.5	4.71	1.0	3.14
33	0.5	1.57	1.0	3.14	1.0	3.14	75	0.5	1.57	1.0	3.14	0.0	0.00	117	0.5	1.57	1.5	4.71	0.5	1.57
34	0.0	0.00	1.0	3.14	0.5	1.57	76	1.0	3.14	0.0	0.00	0.0	0.00	118	0.5	1.57	0.0	0.00	1.5	4.71
35	0.5	1.57	0.0	0.00	1.0	3.14	77	1.0	3.14	0.5	1.57	0.0	0.00	119	1.5	4.71	0.5	1.57	1.0	3.14
36	0.5	1.57	0.0	0.00	0.0	0.00	78	1.5	4.71	1.5	4.71	1.0	3.14	120	0.0	0.00	1.5	4.71	1.0	3.14
37	1.0	3.14	0.0	0.00	1.5	4.71	79	1.0	3.14	1.0	3.14	1.5	4.71	121	1.0	3.14	1.0	3.14	0.0	0.00
38	0.0	0.00	1.0	3.14	0.0	0.00	80	0.5	1.57	1.5	4.71	1.0	3.14	122	0.0	0.00	1.5	4.71	0.0	0.00
39	0.0	0.00	1.0	3.14	1.0	3.14	81	0.0	0.00	1.0	3.14	1.0	3.14	123	0.5	1.57	1.5	4.71	1.0	3.14
40	0.0	0.00	0.5	1.57	0.0	0.00	82	0.5	1.57	0.0	0.00	0.5	1.57	124	1.5	4.71	1.5	4.71	1.0	3.14
41	0.5	1.57	0.5	1.57	0.5	1.57	83	1.5	4.71	1.5	4.71	1.5	4.71	125	0.0	0.00	1.5	4.71	1.5	4.71
42	0.0	0.00	1.0	3.14	0.5	1.57	84	0.0	0.00	0.5	1.57	1.0	3.14	126	1.0	3.14	1.5	4.71	1.5	4.71
														127	0.5	1.57	1.0	3.14	1.5	4.71
														128	0.0	0.00	1.5	4.71	0.5	1.57

Table 4.   OPS Sequences with $N_c = 128$, $L = 3$, $M = 4$ (from [3]).

b. *Waveform Characteristics from Simulation*

Figure 21 shows the PSD versus frequency of the OPS 128 modulation code set #1 with N_c = 128. Figure 22 shows the discrete phase values for the OPS 128 modulation code set #1 with N_c = 128. The four phase values are readily apparent. Figure 23 shows the "I + jQ" phase shift for the OPS 128 modulation code set #1. This plot best illustrates the different signal characteristics between the different code sets. The carrier frequency is $f_c = 1\,\text{kHz}$, $f_s = 7\,\text{kHz}$, and *cpp* = 1. All three plots were generated with the LPIT.
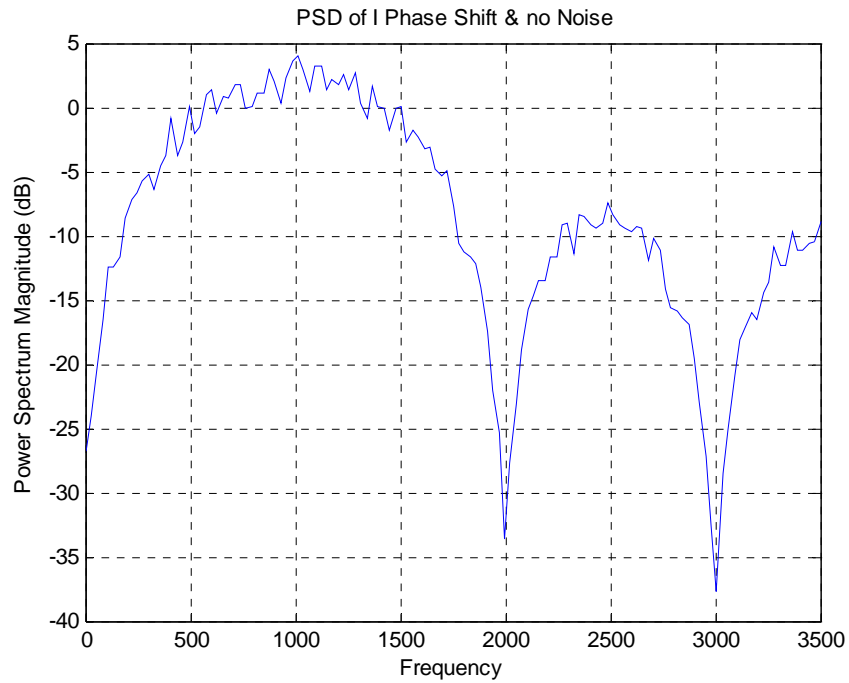
Figure 21.   Power Spectral Density of OPS 128 Code 1 (Signal only).
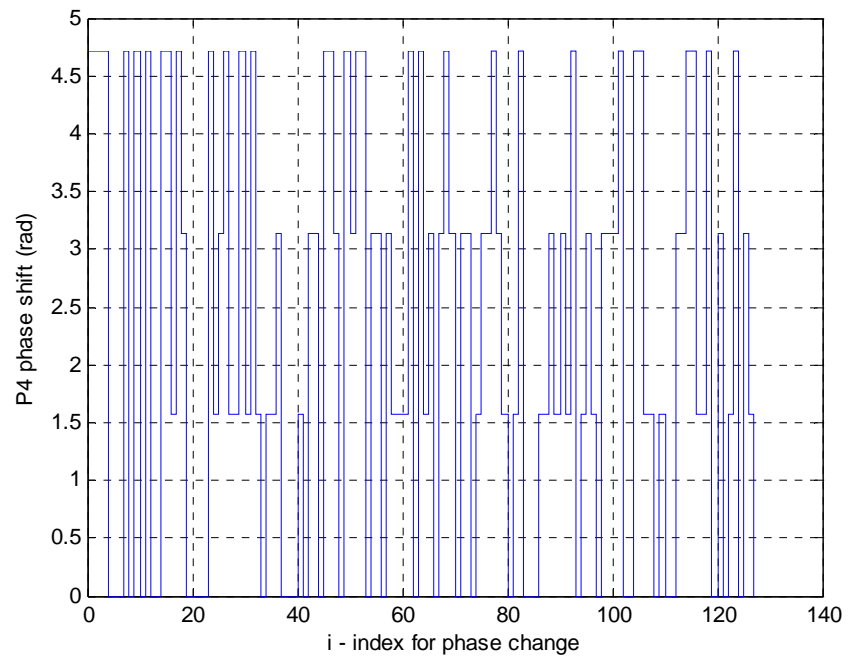
Figure 22.   OPS 128 Code 1 showing one period of phase shifts (radians).
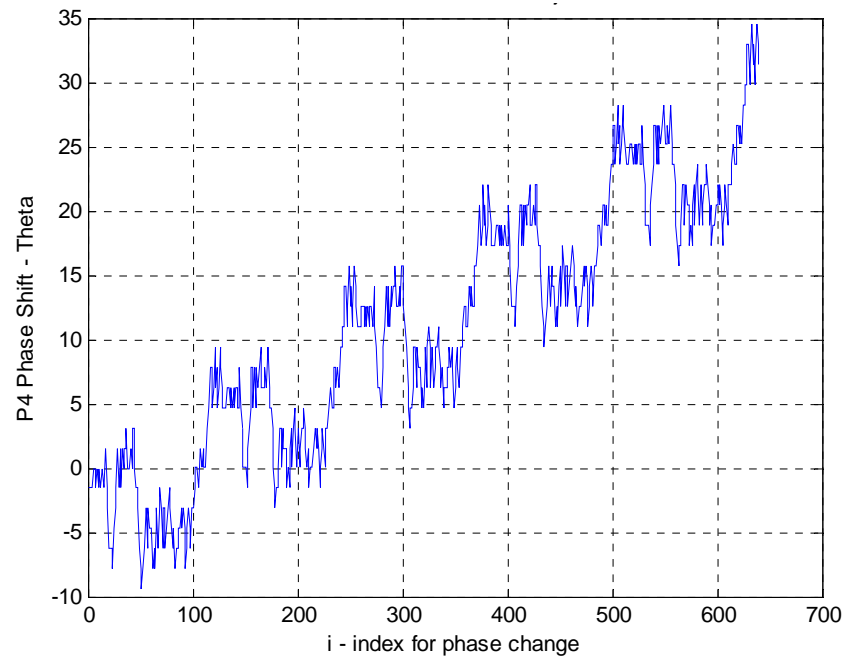
Figure 23.   OPS 128 Code 1 showing five periods of phase shifts (degrees).

36

Figure 24 shows the PSD versus frequency of the OPS 128 modulation code set #2 with N_c = 128. Figure 25 shows the discrete phase values for the OPS 128 modulation code set #2 with N_c = 128, the four phase values are readily apparent. Figure 26 shows the "I + jQ" phase shift for the OPS 128 modulation code set #2. This plot best illustrates the different signal characteristics between the different code sets. The carrier frequency is $f_c = 1\,\text{kHz}$, $f_s = 7\,\text{kHz}$, and cpp = 1. All three plots were generated with the LPIT.
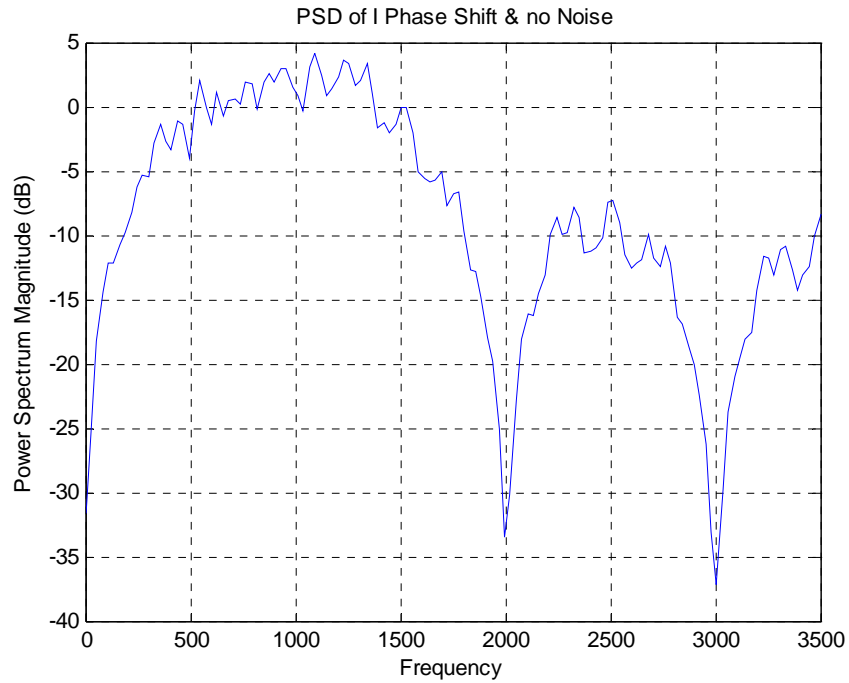
Figure 24.　　Power Spectral Density of OPS 128 Code 2 (Signal only).
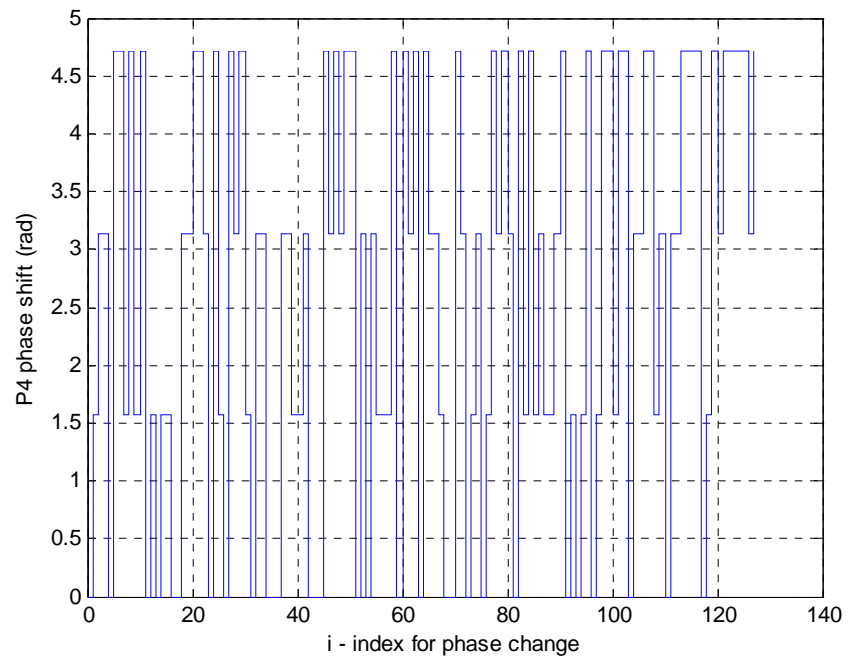
Figure 25.   OPS 128 Code 2 showing one period of phase shifts (radians).
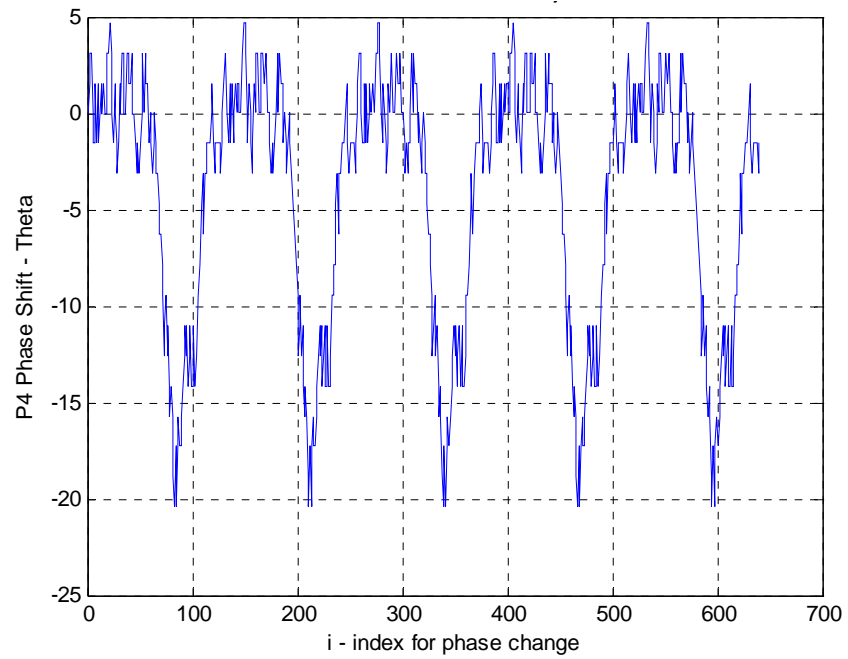
Figure 26.   OPS 128 Code 2 showing five periods of phase shifts (degrees).

38

Figure 27 shows the PSD versus frequency of the OPS 128 modulation code set #3 with N_c = 128. Figure 28 shows the discrete phase values for the OPS 128 modulation code set #3 with N_c = 128, the four phase values are readily apparent. Figure 29 shows the "I + jQ" phase shift for the OPS 128 modulation code set #3. This plot best illustrates the different signal characteristics between the different code sets. The carrier frequency is $f_c = 1\,\text{kHz}$, $f_s = 7\,\text{kHz}$, and cpp = 1. All three plots were generated with the LPIT.
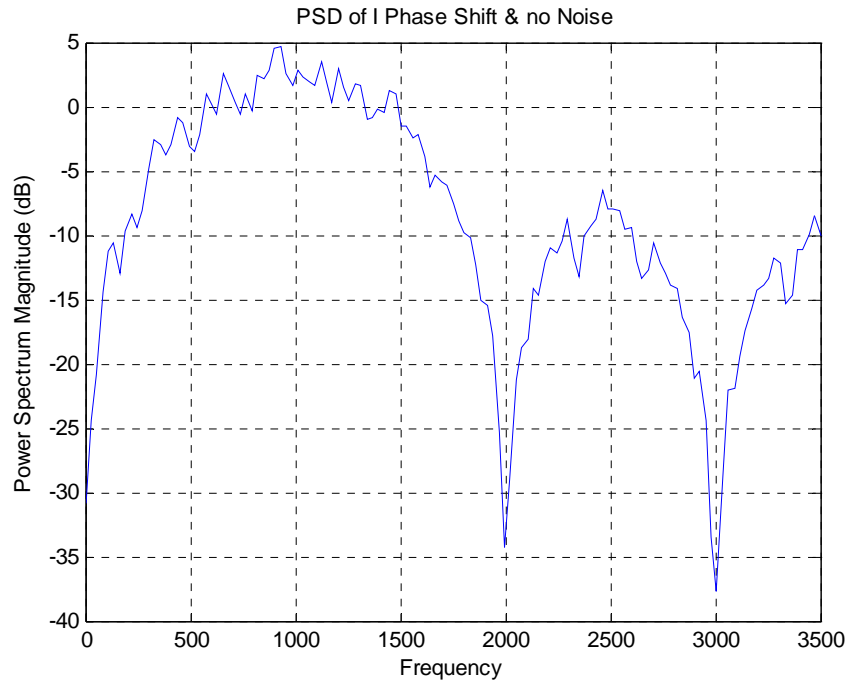
Figure 27.   Power Spectral Density of OPS 128 Code 3 (Signal only).
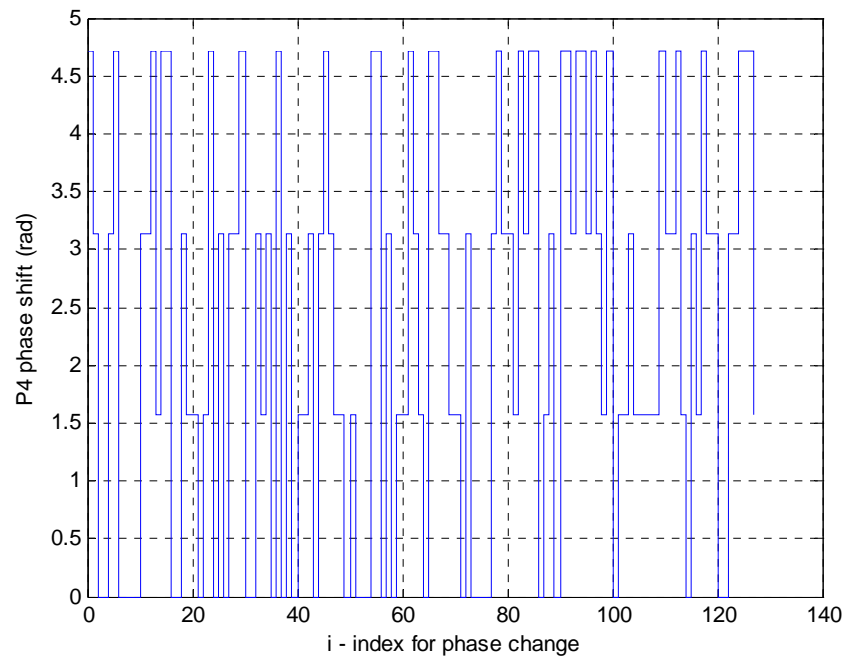
Figure 28.   OPS 128 Code 3 showing one period of phase shifts (radians).
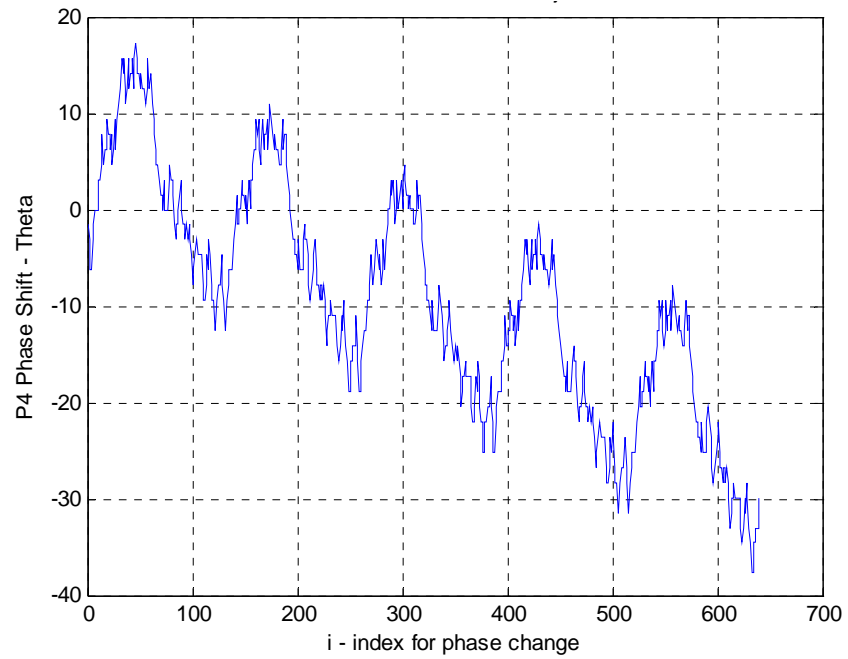
Figure 29.   OPS 128 Code 3 showing five periods of phase shifts (degrees).

Figure 30 (top plot) shows the ACF and the corresponding sidelobe structure for the OPS 128 code set #1. The peak sidelobe level (PSL) can be seen at approximately −21 dB from the peak [3]. Figure 30 (bottom plot) shows the PACF. Figure 31 shows the PAF. Based on the signal parameters $f_c = 1\,\text{kHz}$, $f_s = 7\,\text{kHz}$, and $cpp = 1$ and using Equation (24) the PAF repeats every code period as shown by [1]:

$$b_{sc} = N_c \left(cpp * \frac{fs}{fc} \right) = 896 \text{ samples} \tag{24}$$

All three plots were generated with ambfn7 [16].
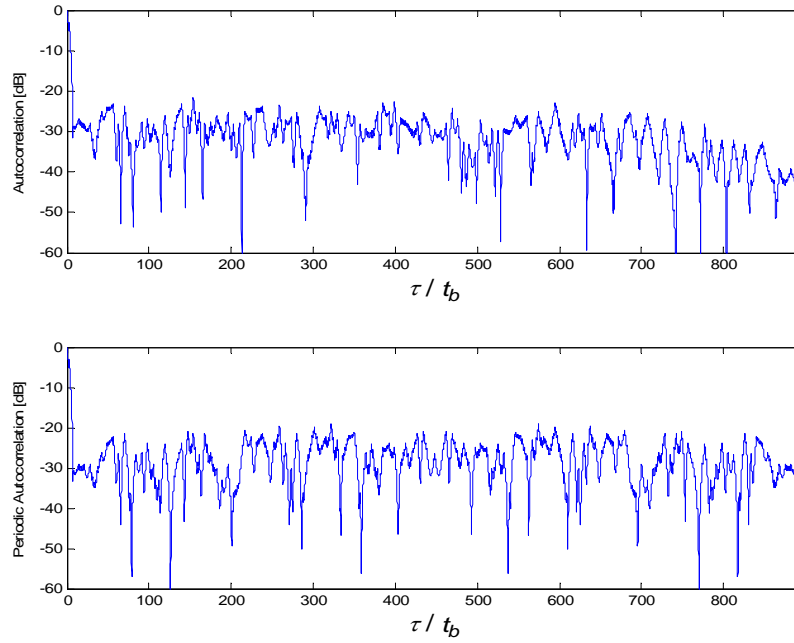
Figure 30.   OPS 128 Code 1 ACF (top) and PACF (bottom).
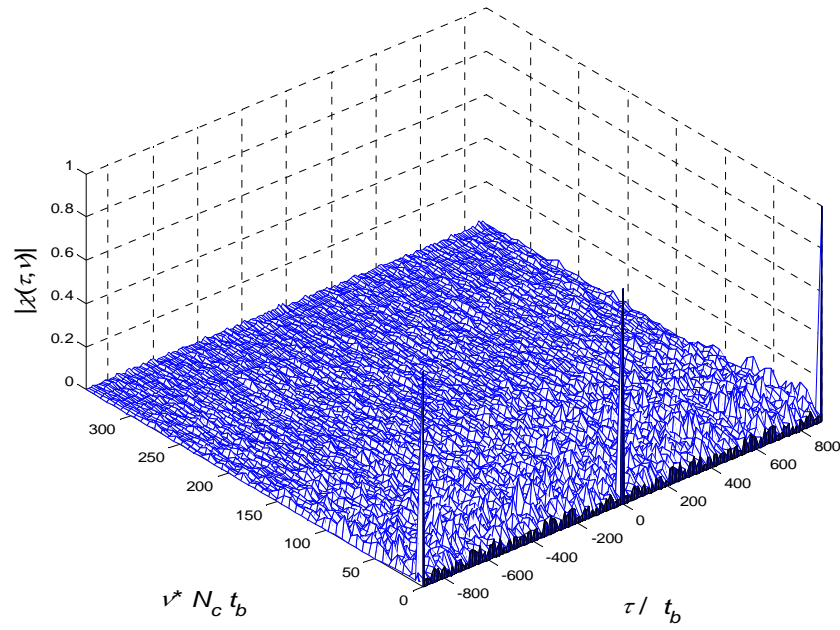
Figure 31.　　　OPS 128 Code 1 Periodic Ambiguity Function Plot.

　　　To illustrate the non-interference nature of the OPS 128 signal the CCF was calculated for all three possible combinations of signals that would be utilized by a networked LPI radar system with three nodes. Each would be transmitting its own code set. Theoretically there would be no interference between each different code sets using similar signal parameters. Figure 32 shows the CCF for the OPS 128 code set #1 and code set #2 on the left contrasted with the ACF of OPS 40 code set #1 on the right. Figure 33 shows the CCF for the OPS 128 code set #2 and code set #3 on the left contrasted with the ACF of OPS 40 code set #2 on the right. Figure 34 shows the CCF for the OPS 128 code set #3 and code set #1 on the left contrasted with the ACF of OPS 40 code set #3 on the right.
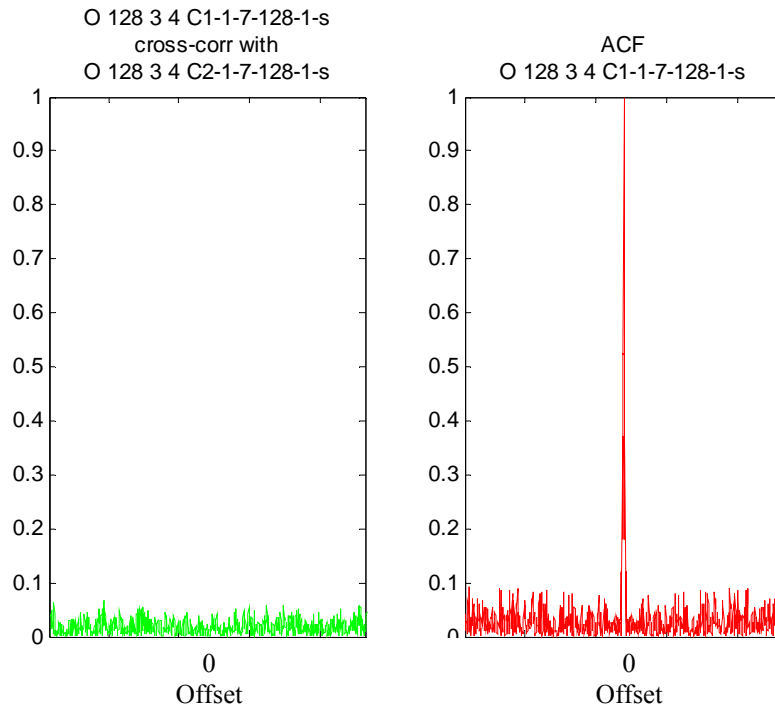
Figure 32.   OPS 128 Codes 1 and 2 CCF Plot (Left) and Code 1 ACF Plot (Right).
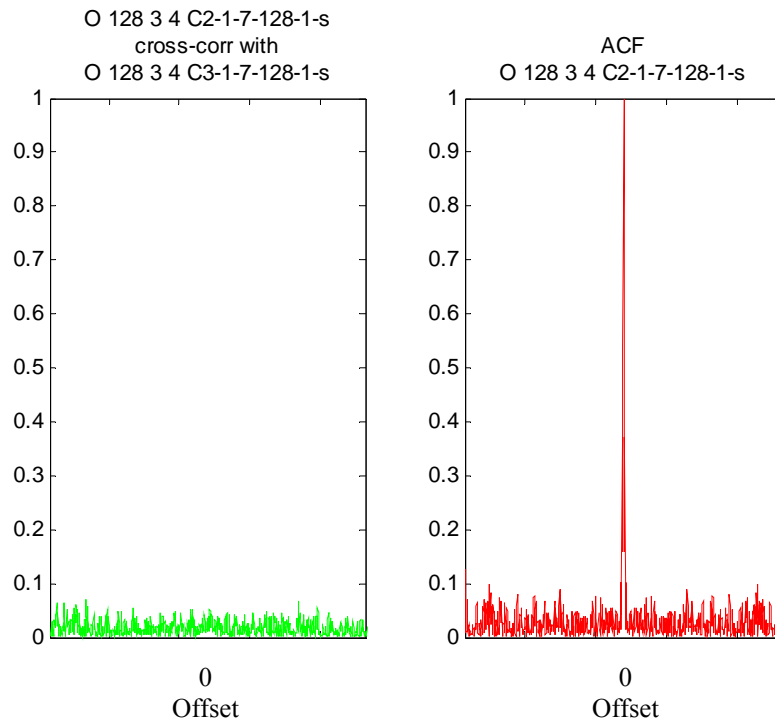
Figure 33.   OPS 128 Codes 2 and 3CCF Plot (Left) and Code 2 ACF Plot (Right).

43
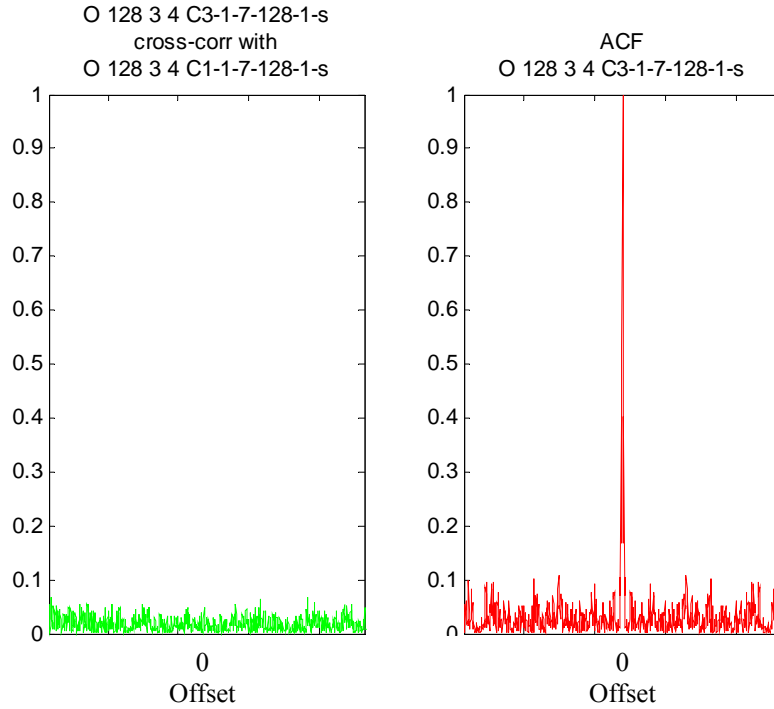
Figure 34.   OPS 128 Codes 3 and 1 CCF Plot (Left) and Code 3 ACF Plot (Right).

3.   Optimized Orthogonal Polyphase Sequences with Doppler Tolerance

The Optimized OPS by Kahn is an improvement on Deng's orthogonal polyphase sequences and are obtained through the use of an improved design tool known as cross entropy (CE). Using this optimization technique, the new polyphase sequences provide an improved Doppler tolerance in addition to being orthogonal. Deng's OPS required Doppler correction by the radar receiver while the Khan code is designed to be inherently Doppler resistant [5].

a.   Waveform Description

The Optimized OPS 40 code was designed with the following initial values, $L = 40$, $M = 3$, and $y = 4$. There are three code sets associated with this particular design. There are many more available phases for use in the Optimized OPS. These phases are more complex than for OPS 40, but this complexity provides the Doppler tolerance characteristic of the signal design. The selection of code phases is determined

from an array based on the value of *Y*. The MATLAB [2] code allows for user selection of all variables in Table 5. To prevent confusion and aid the user in creation of signals a naming convention was established for the Optimized OPS 40 code. The entire Optimized OPS 40 code file names begin with KO 40 4 4 (KO "N" "M" "y"). They are followed by the set number (i.e. C1), the carrier frequency (in kHz), the sampling frequency (in kHz), the code length, the number of cycles per phase, and finally the SNR (in dB, or "s" for signal only).

The Optimized OPS 40 code is selected as the length is short enough that the algorithm does not require a significant computation time, yet it is long enough that its performance exceeds that of shorter code lengths. The Optimized OPS 40 code is displayed in Table 6. Each code sequence is listed vertically ($M = 3$) and the sub-code index is listed horizontally ($N_c = 40$) to show the difference in phase value between each sub-code in each sequence. Equation (25) shows the method of determining the polyphase code value, where *m* is the number of code sequences (or radar transmitters), *P* is the number of phases to choose from, and *y* is the number of polyphase code value sets to select from on either side of the center of possible sets illustrated below:

$$ s_{m(i-y)}(l) \in X_i = \left\{ (|i-y|+1)\frac{2\pi}{yP}(0,1,2,...,(P-2)) \right\} \tag{25} $$

The center-most (*i*=4) phase value sets to choose from using Equation (25) and *y=4* and *P*=10 are from the following set $\{2\pi/40(0,1,2,...,8)\}$. Figure 35 illustrates the tendency for values of the polyphase codes available to get larger as the value of *i* moves away from the center value.

This increased diversity in phase values provides an inherent invulnerability to non-cooperative ESR and due to the nature of polyphase codes does not increase the signal bandwidth that is governed by the sub-code period. The harmonic relationship between polyphase sequences from one phase value to the next is the property that provides the Doppler tolerance. Building this harmonic nature into the creation of the polyphase code sequence decreases the loss due to the effect of a Doppler shift [7]. The Optimized OPS 40 code was generated for testing with the following characteristics as shown in Table 5.

45

Specific Signal Identification: KO 40 3 4 C1-1-7-40-1-s	
Carrier frequency (f_c)	1000 Hz
Sampling frequency (f_s)	7000 Hz
Number of phases	40
SNR	Signal Only
Number of cycles per phase	1
Number of potential signals in the set	3

Table 5.   Optimized OPS 40 Signal Characteristics.

Index	Code 1 $x \times \pi$	Code 1 Rad	Code 2 $x \times \pi$	Code 2 Rad	Code 3 $x \times \pi$	Code 3 Rad
1	1.60	5.03	0.60	1.88	0.80	2.51
2	1.00	3.14	0.20	0.63	0.40	1.26
3	1.20	3.77	1.00	3.14	0.00	0.00
4	0.80	2.51	1.20	3.77	0.00	0.00
5	1.80	5.65	1.80	5.65	1.00	3.14
6	0.40	1.26	1.80	5.65	1.80	5.65
7	1.35	4.24	0.15	0.47	1.05	3.30
8	1.05	3.30	0.60	1.88	0.45	1.41
9	0.30	0.94	1.35	4.24	1.20	3.77
10	0.15	0.47	0.30	0.94	0.45	1.41
11	1.35	4.24	1.35	4.24	1.05	3.30
12	1.35	4.24	1.20	3.77	1.35	4.24
13	0.20	0.63	0.50	1.57	0.80	2.51
14	0.00	0.00	0.80	2.51	0.90	2.83
15	0.10	0.31	0.50	1.57	0.10	0.31
16	0.80	2.51	0.00	0.00	0.20	0.63
17	0.00	0.00	0.70	2.20	0.90	2.83
18	0.60	1.88	0.80	2.51	0.90	2.83
19	0.05	0.16	0.00	0.00	0.00	0.00
20	0.20	0.63	0.05	0.16	0.05	0.16
21	0.05	0.16	0.10	0.31	0.05	0.16
22	0.25	0.79	0.05	0.16	0.25	0.79
23	0.90	2.83	0.80	2.51	0.00	0.00
24	0.90	2.83	0.10	0.31	0.90	2.83
25	0.20	0.63	0.80	2.51	0.00	0.00
26	0.70	2.20	0.10	0.31	0.80	2.51
27	0.00	0.00	0.90	2.83	0.80	2.51
28	0.20	0.63	0.60	1.88	0.20	0.63
29	1.20	3.77	1.20	3.77	1.35	4.24
30	1.35	4.24	0.45	1.41	0.15	0.47
31	0.00	0.00	0.45	1.41	1.35	4.24
32	0.00	0.00	0.00	0.00	1.35	4.24
33	1.20	3.77	1.35	4.24	0.30	0.94
34	0.30	0.94	1.20	3.77	0.75	2.36
35	1.40	4.40	0.40	1.26	1.20	3.77
36	0.60	1.88	1.20	3.77	0.60	1.88
37	0.20	0.63	1.40	4.40	0.60	1.88
38	1.20	3.77	0.60	1.88	1.20	3.77
39	1.20	3.77	0.00	0.00	1.40	4.40
40	1.60	5.03	1.80	5.65	1.40	4.40

Table 6.　　Optimized OPS Sequences $L = 40$, $M = 3$, $Y = 4$ (from [5]).
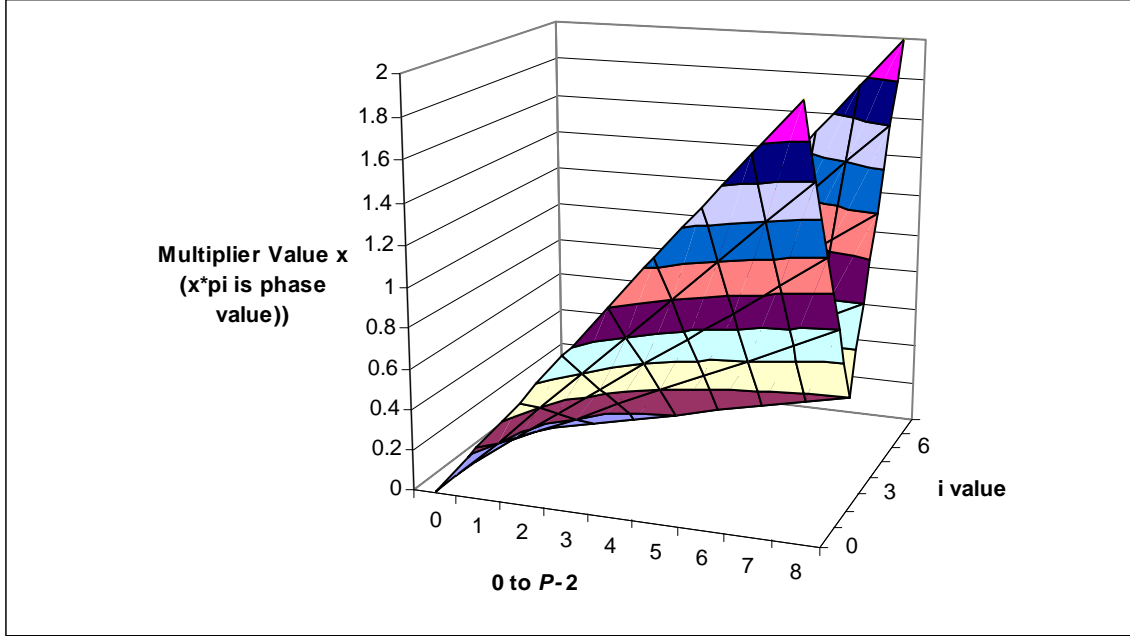
Figure 35.   Graphical Representation of Potential Phase Code Values.

b.   *Waveform Characteristics from Simulation*

Figure 36 shows the PSD versus frequency of the Optimized OPS 40 modulation code set #1 with $N_c = 40$. Figure 37 shows the discrete phase values for the Optimized OPS 40 modulation code set #1 with $N_c = 40$, the four phase values are readily apparent. Figure 38 shows the "I + jQ" phase shift for the Optimized OPS 40 modulation code set #1. This plot best illustrates the different signal characteristics between the different code sets. The carrier frequency is $f_c = 1\,\text{kHz}$, $f_s = 7\,\text{kHz}$, and *cpp* = 1. All three plots were generated with the LPIT.

48
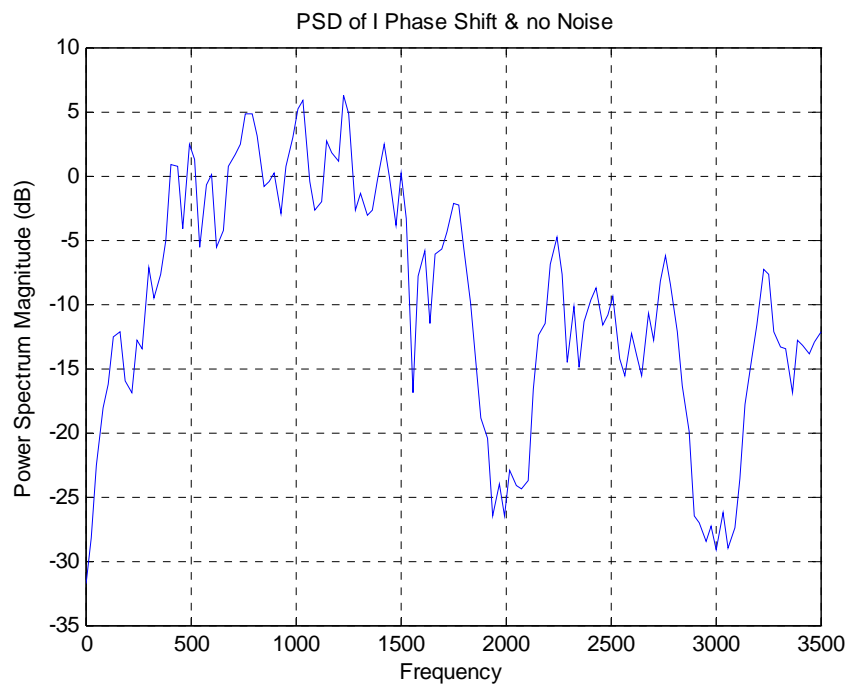
Figure 36.   Power Spectral Density of Optimized OPS 40 Code 1 (Signal only).
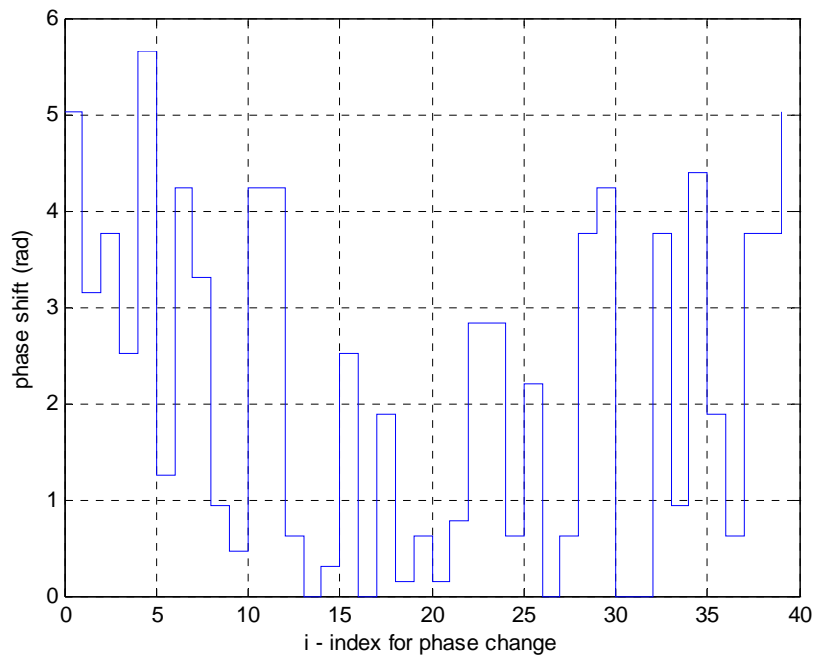
Figure 37.   Optimized OPS 40 Code 1 showing one period of phase shifts (radians).
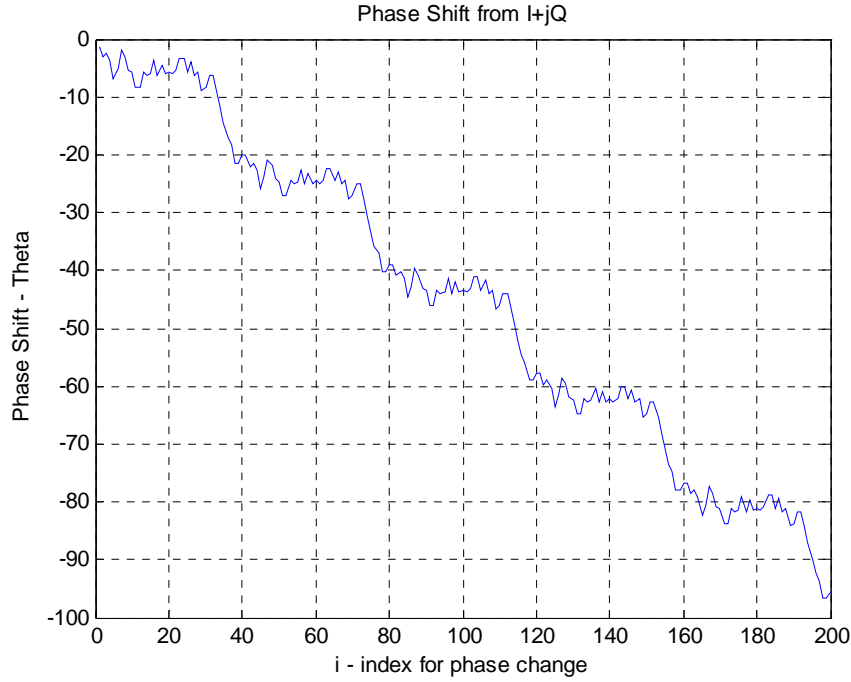
Figure 38.   Optimized OPS 40 Code 1 showing five periods of phase
shifts (degrees).

Figure 39 shows the PSD versus frequency of the Optimized OPS 40 modulation code set #2 with $N_c = 40$. Figure 40 shows the discrete phase values for the optimized OPS 40 modulation code set #2 with $N_c = 40$, the four phase values are readily apparent. Figure 41 shows the "I + jQ" phase shift optimized for the OPS 40 modulation code set #2. This plot best illustrates the different signal characteristics between the different code sets. The carrier frequency is $f_c = 1\,\text{kHz}$, $f_s = 7\,\text{kHz}$, and *cpp* = 1. All three plots were generated with the LPIT.
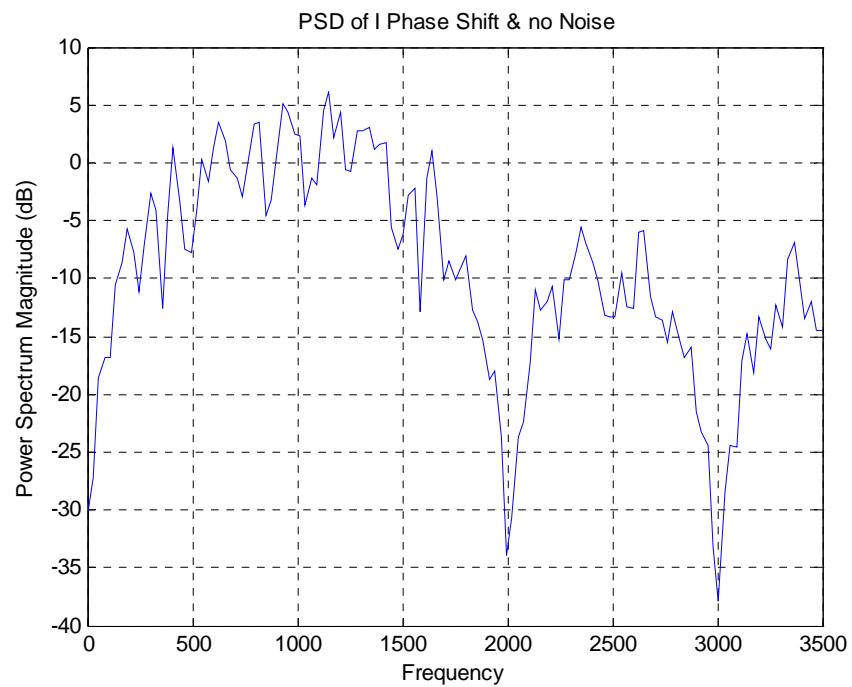
Figure 39.   Power Spectral Density of Optimized OPS 40 Code 2 (Signal only).
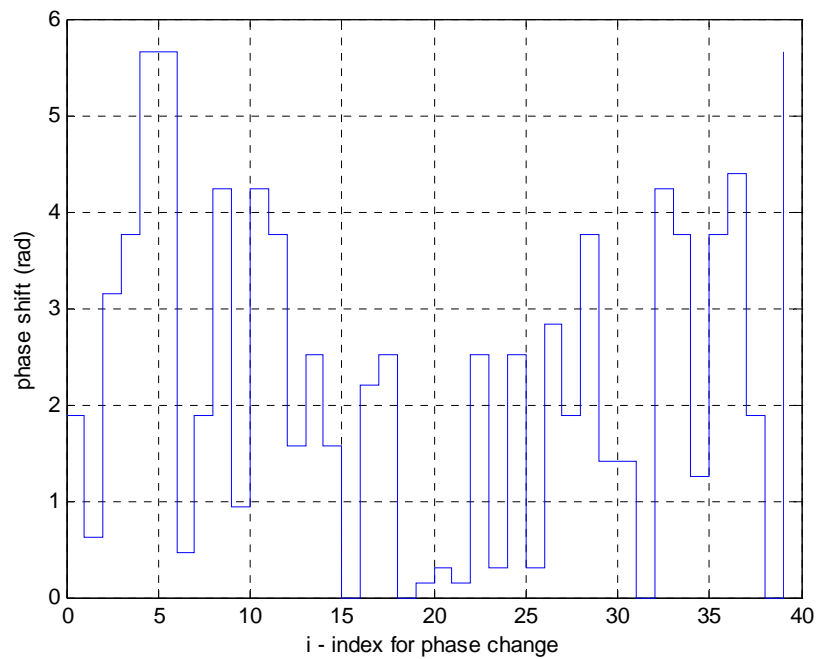
Figure 40.   Optimized OPS 40 Code 2 showing one period of phase
shifts (radians).

51
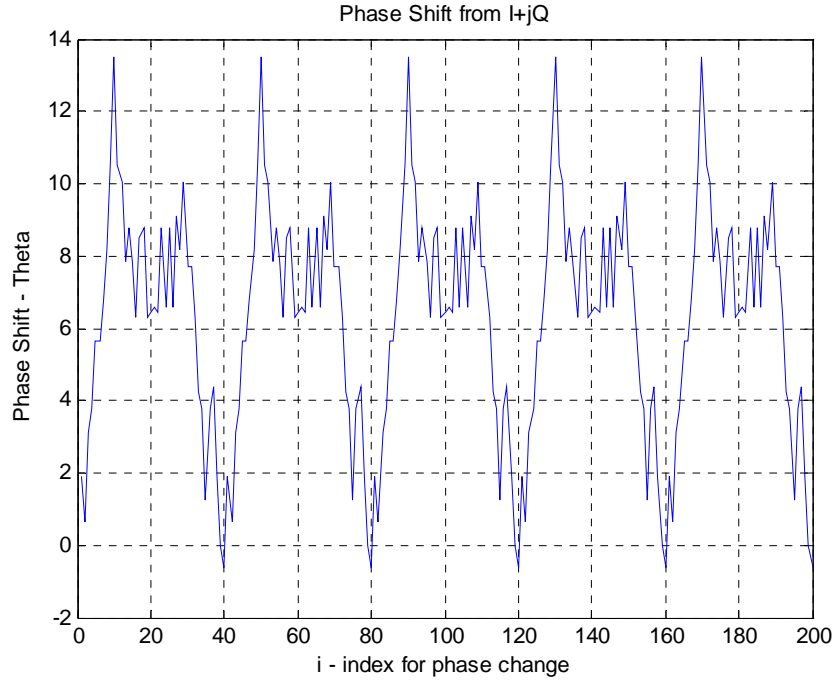
Figure 41.   Optimized OPS 40 Code 2 showing five periods of phase
shifts (degrees).

Figure 42 shows the PSD versus frequency of the Optimized OPS 40 modulation code set #3 with $N_c = 40$. Figure 43 shows the discrete phase values for the optimized OPS 40 modulation code set #3 with $N_c = 40$, the four phase values are readily apparent. Figure 44 shows the "I + jQ" phase shift optimized for the OPS 40 modulation code set #3. This plot best illustrates the different signal characteristics between the different code sets. The carrier frequency is $f_c = 1\,\mathrm{kHz}$, $f_s = 7\,\mathrm{kHz}$, and *cpp* = 1. All three plots were generated with the LPIT.
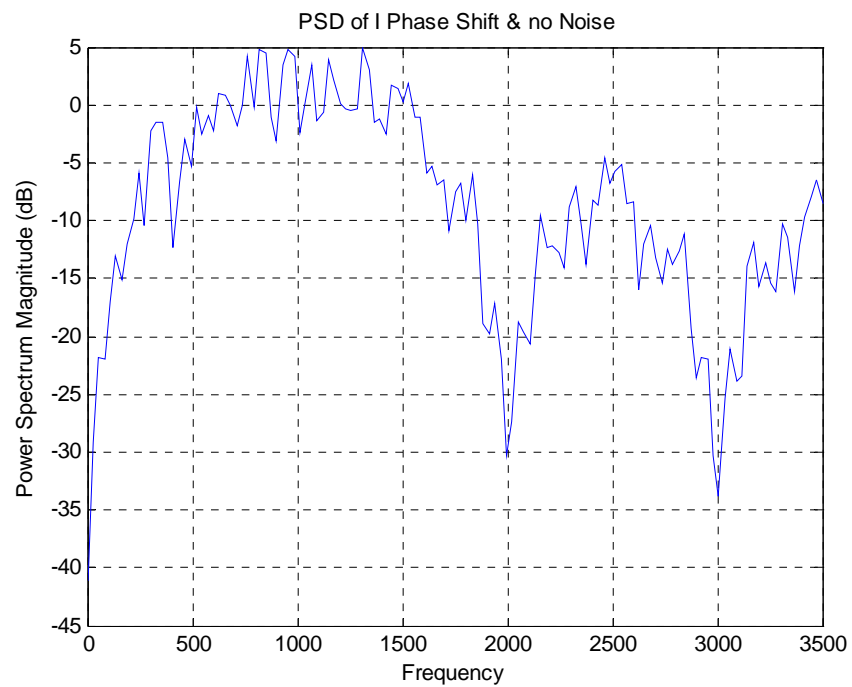
Figure 42.   Power Spectral Density of Optimized OPS 40 Code 3 (Signal only).
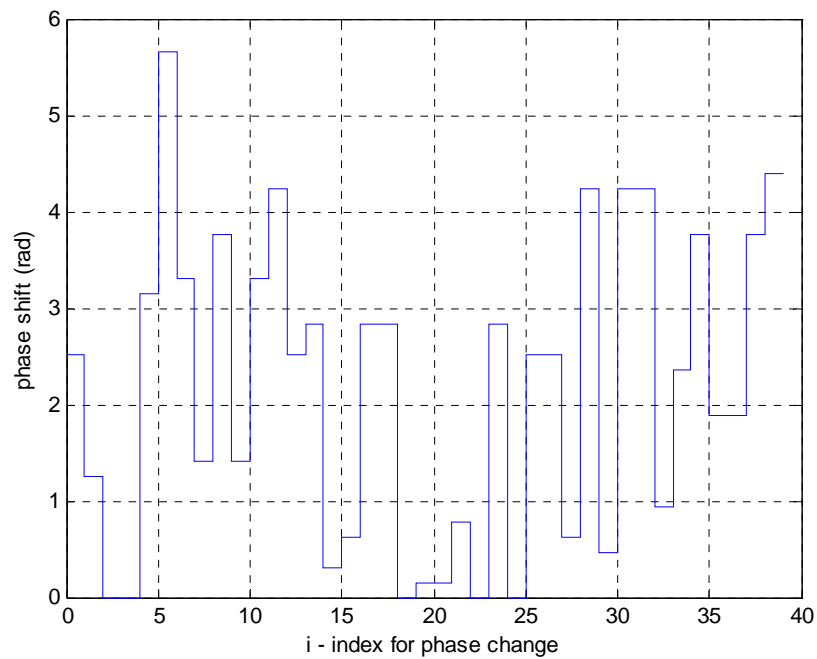
Figure 43.   Optimized OPS 40 Code 3 showing one period of phase shifts (radians).

53
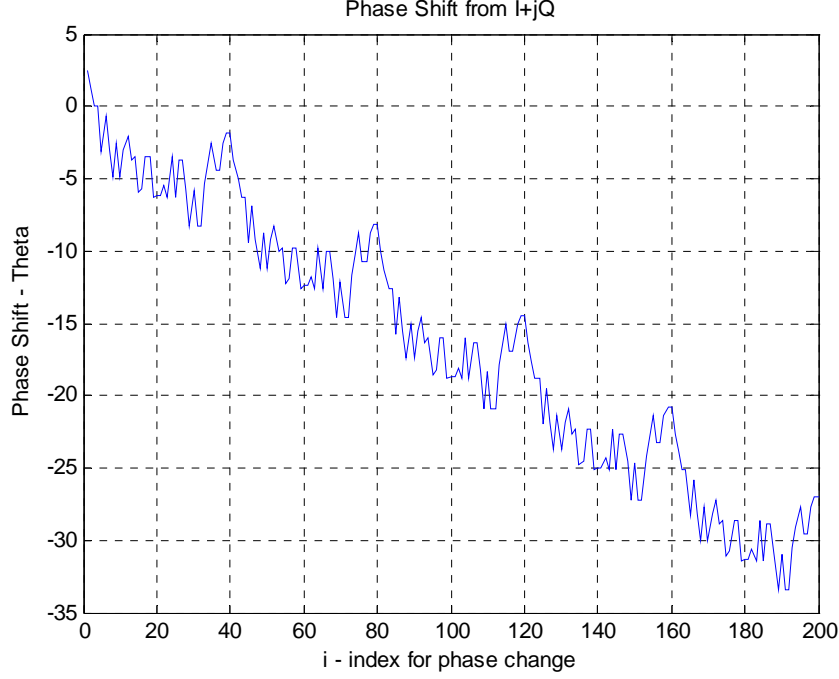
Figure 44.   Optimized OPS 40 Code 3 showing five periods of phase
shifts (degrees).

Figure 45 (top plot) shows the ACF and the corresponding sidelobe structure for the optimized OPS 40 code set #1. The PSL can be seen at approximately -17 dB from the peak in Figure 45 (bottom plot). All three plots were generated with ambfn7 [16]. Figure 46 shows the PAF. Based on the signal parameters $f_c = 1\,\text{kHz}$, $f_s = 7\,\text{kHz}$, and $cpp = 1$ and using Equation (26) the PAF repeats every code period as shown by [1]:

$$b_{sc} = N_c \left(cpp * \frac{fs}{fc} \right) = 280 \text{ samples} \qquad (26)$$
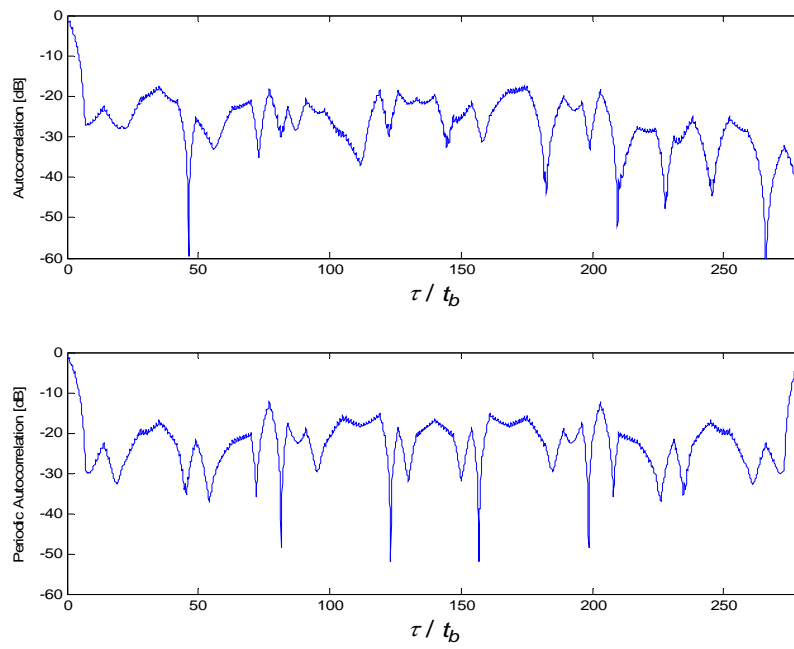
Figure 45.   Optimized OPS 40 Code 1 ACF (top) and PACF (bottom).
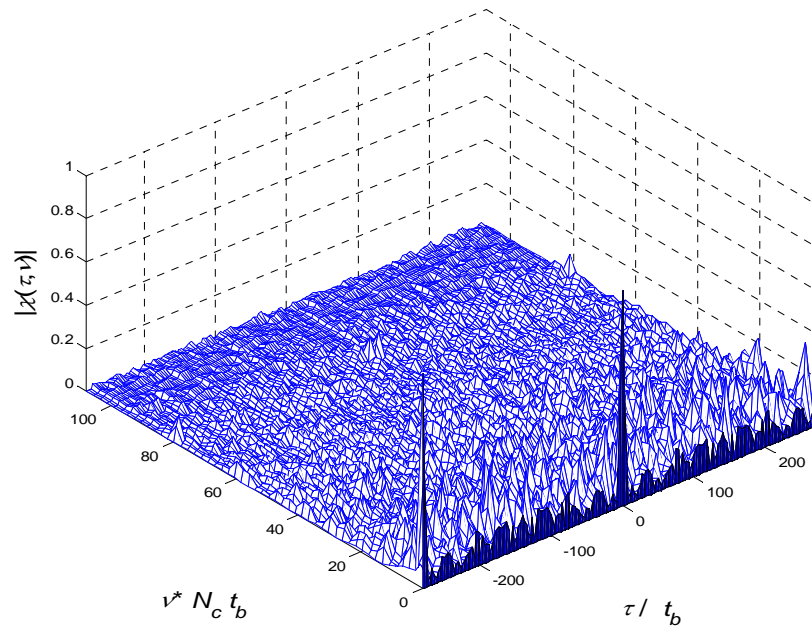
Figure 46.   Optimized OPS 40 Code 1 Periodic Ambiguity Function Plot.

To illustrate the non-interference nature of the Optimized OPS 40 signal the CCF was calculated for all three possible combinations of signals that would be utilized by a networked LPI radar system with three nodes. Each would be transmitting its own code set. Theoretically there would be no interference between each different code sets using similar signal parameters. Figure 47 shows the CCF for the optimized OPS 40 code set #1 and code set #2 on the left contrasted with the ACF of optimized OPS 40 code set #1 on the right. Figure 48 shows the CCF for the optimized OPS 40 code set #2 and code set #3 on the left contrasted with the ACF of optimized OPS 40 code set #2 on the right. Figure 49 shows the CCF for the optimized OPS 40 code set #3 and code set #1 on the left contrasted with the ACF of optimized OPS 40 code set #3 on the right.
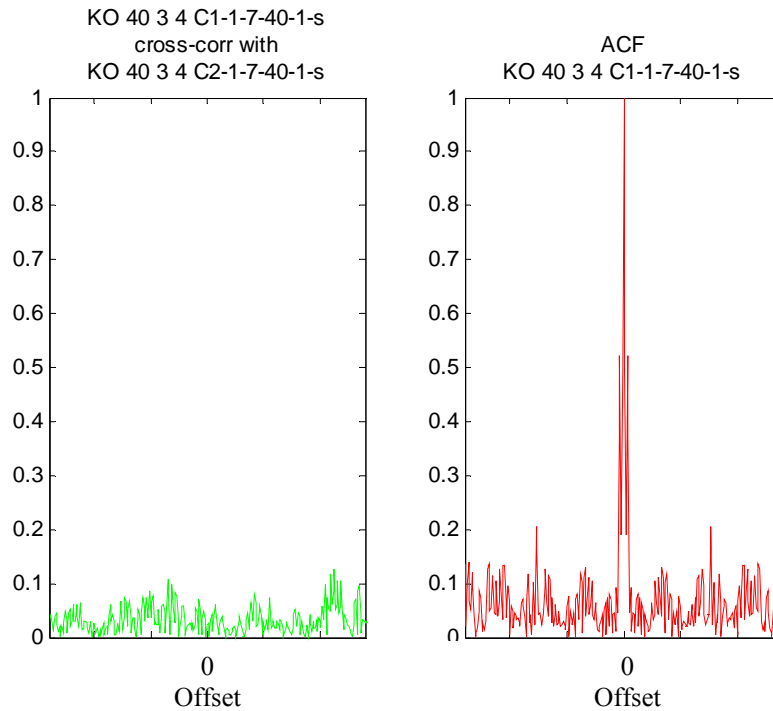
Figure 47.   Opt. OPS 40 Codes 1 and 2 CCF Plot (Left) and Code 1 ACF Plot (Right).

KO 40 3 4 C2-1-7-40-1-s
cross-corr with
KO 40 3 4 C3-1-7-40-1-s

ACF
KO 40 3 4 C2-1-7-40-1-s

Offset

Offset
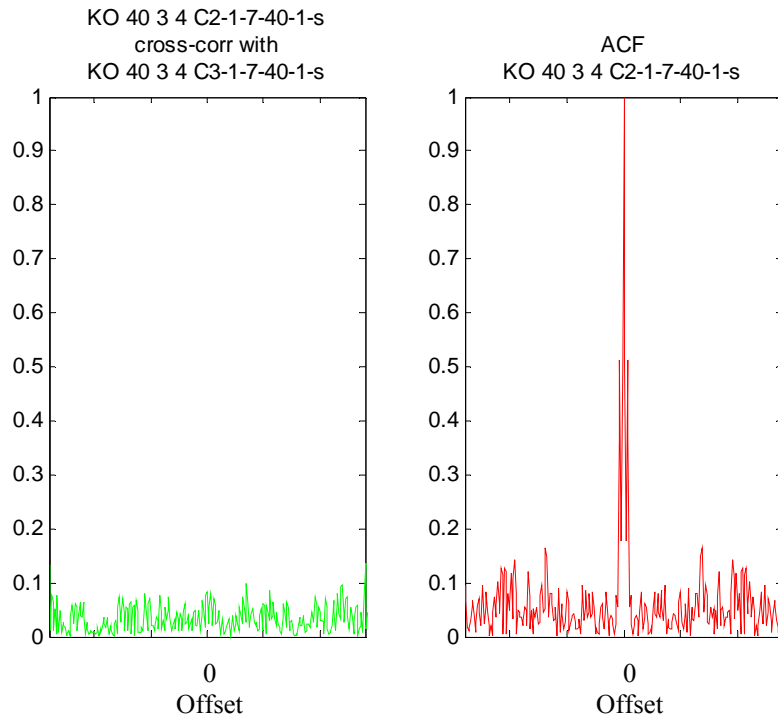
Figure 48.   Opt. OPS 40 Codes 2 and 3 CCF Plot (Left) and Code 2
ACF Plot (Right).

KO 40 3 4 C3-1-7-40-1-s
cross-corr with
KO 40 3 4 C1-1-7-40-1-s

ACF
KO 40 3 4 C3-1-7-40-1-s

Offset

Offset
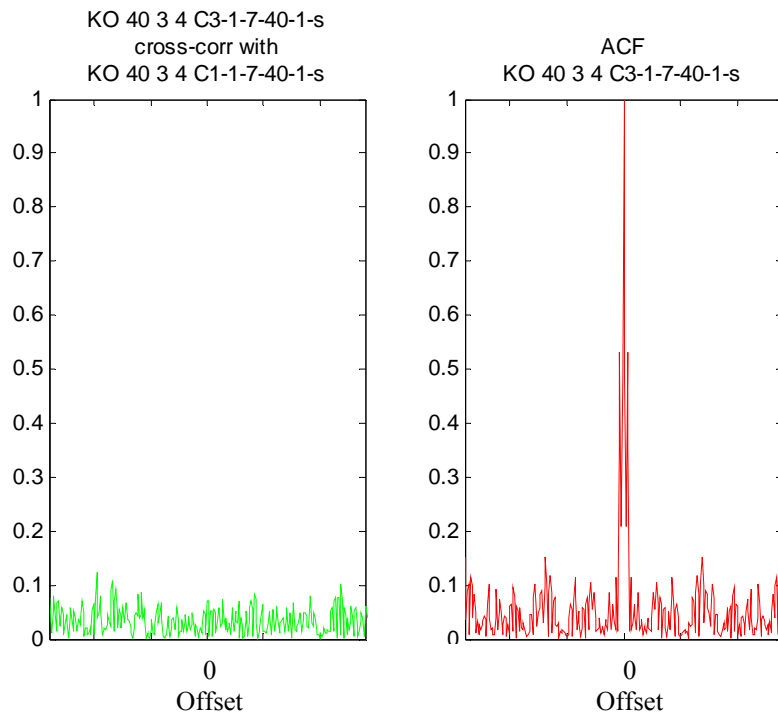
Figure 49.   Opt. OPS 40 Codes 3 and 1 CCF Plot (Left) and Code 3
ACF Plot (Right).

57

B.   DISCRETE FREQUENCY CODING

1.   DFC 32 Frequency Series

The orthogonal discrete frequency coding (DFC) waveforms are identified as a set of L frequency hopping sequences. Each frequency hopping sequence is a CW waveform defined by the number N_F of contiguous frequency codes of each duration t_p. As length N_F increases, so does radar performance in terms of the auto-correlation side lobe levels decreasing. Computation time deriving the codes is increased with increasing values of N_F. Similar frequency hopping waveforms have been developed such as the Costas arrays, but for use in a single radar system. Algebraic calculations for two or more different Costas arrays do not guarantee a low cross correlation between the different waveforms [3].

The next step is the formation of a frequency code matrix, which consists of L sets of frequency codes of length N_F. SA is required in the determination of multiple frequency coded sequences with low cross correlation because algebraic determination of greater than two sequences is very difficult [3]. SA was initially designed for VLSI circuit design [3]. The algorithm is an optimization algorithm with the benefit of not becoming fixed on local optima during the search process. The optimization process is based on the comparison of two properties of the DFC signal, the autocorrelation and the cross correlation. Specifically the code set must satisfy Equation (27) and Equation(28) [5].

$$A(s_l, \tau) = \frac{1}{N} \int_t s_l(t) s_l^*(t - \tau) dt \begin{cases} = 1, \tau = 0 \\ \approx 0, otherwise \end{cases} \quad l = 1, 2, ...L \quad (27)$$

$$C(s_p, s_q, \tau) = \frac{1}{N} \int_t s_p(t) s_q^*(t - \tau) dt \approx 0, p \neq q, p, q = 1, 2, ...L \quad (28)$$

The cost function is given by Equation(29). The principle of the cost function is to minimize the autocorrelation sidelobe peaks and the cross correlation peaks. The optimization technique is to minimize the total autocorrelation sidelobe energy and cross correlation energy. This is shown in Equation(29).

$$E = \sum_{l=1}^{L} \int_{\tau} |A(s_l, \tau)|^2 \, d\tau + \sum_{p=1}^{L-1} \sum_{q=p+1}^{L} \int_{\tau} |C(s_p, s_q, \tau)|^2 \, d\tau \qquad (29)$$

Given the predetermined values of L and N_F the minimization of Equation (29) utilizing SA will generate a group of frequency coded sequences that are automatically constrained by Equation (27) and Equation(28) [5]. For signal generation the frequency multiplier value was multiplied by a base frequency to achieve the 32 frequency values for the signal. Most of the DFC signals that were generated had a base frequency of 1 kHz, this yielding a frequency range from 1 kHz to 32 kHz for the signal to be analyzed.

a.   *Waveform Description*

The Discrete Frequency Coding sequence was generated for testing with the following characteristics shown in Table 7. Table 8 shows the frequency multiplier values for DFC signal with 32 frequencies.

Specific Signal Identification: DFC-32-1-7-1000	
Base frequency (f)	1000 Hz
Sampling frequency (f_s)	7000 Hz
Number of frequencies (N_F)	32
SNR	Signal Only
Frequency duration (t_p)	0.001 s
Number of potential signals in the set	3

Table 7.   DFC Signal Characteristics.

Index	Code 1	Code 2	Code 3
	Frequency Multiplier		
1	32	3	32
2	29	12	14
3	2	13	19
4	31	15	21
5	4	30	12
6	9	17	8
7	11	7	30
8	13	2	28
9	8	10	9
10	26	22	23
11	12	25	1
12	16	24	2
13	24	6	22
14	14	27	15
15	28	20	10
16	23	4	18
17	27	8	6
18	18	31	26
19	6	14	27
20	22	9	11
21	7	21	20
22	3	18	17
23	30	19	31
24	16	5	16
25	17	1	13
26	20	29	24
27	10	32	5
28	21	16	4
29	19	28	7
30	1	11	3
31	25	26	29
32	5	23	25

Table 8.   DFC Frequency-Coding Sequences (based on [4]).

b.   *Waveform Characteristics from Simulation*

Figure 50 shows the power spectrum magnitude versus frequency of the DFC modulation code set #1 with N_F = 32. The base frequency is $f = 1\,\text{kHz}$, $f_s = 100\,\text{kHz}$, and $t_p = 0.001$ s. The plot was generated with the LPIT.
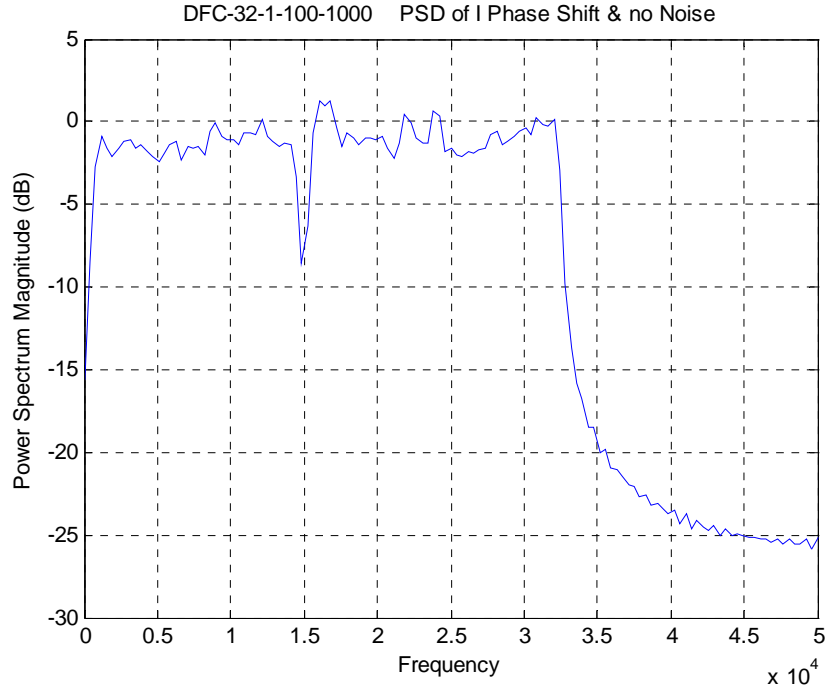
Figure 50.   Power Spectral Density of DFC Set 1 (Signal Only).

Figure 51 shows the power spectrum magnitude versus frequency of the DFC modulation code set #2 with N_F = 32. The base frequency is $f = 1\,\text{kHz}$, $f_s = 100\,\text{kHz}$, and $t_p = 0.001$ s. The plot was generated with the LPIT.
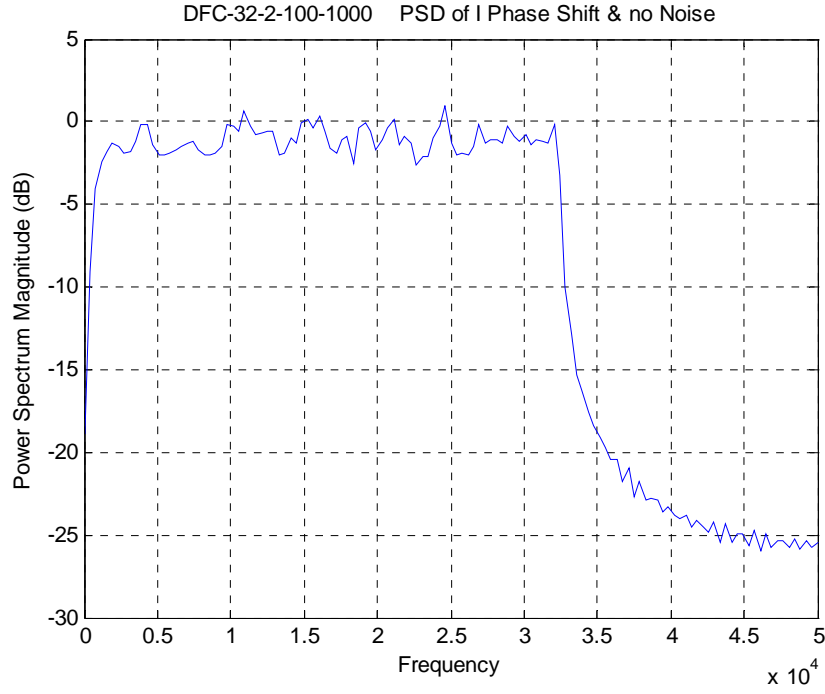
Figure 51.   Power Spectral Density of DFC Set 2 (Signal Only).

Figure 52 shows the power spectrum magnitude versus frequency of the DFC modulation code set #3 with N_F = 32.   The base frequency is $f = 1\,\text{kHz}$, $f_s = 100\,\text{kHz}$, and t_p = 0.001 s. The plot was generated with the LPIT.
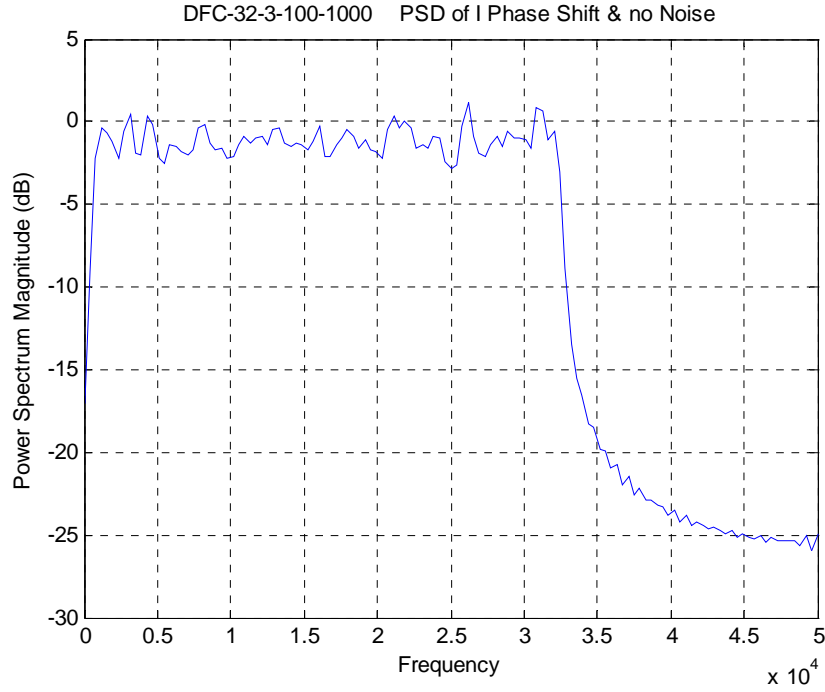
Figure 52.　　　Power Spectral Density of DFC Set 3 (Signal Only).

Figure 53 (top plot) shows the ACF and the corresponding sidelobe structure for the OPS 40 code set #1. The peak sidelobe level (PSL) is slightly higher than -20 dB from the peak [4]. Figure 53 (bottom plot) shows the PACF. Figure 54 shows the PAF. The carrier frequency is $f = 1 \, \text{kHz}$, $f_s = 100 \, \text{kHz}$, and $t_p = 0.001$ s. All three plots were generated with ambfn7 [16].
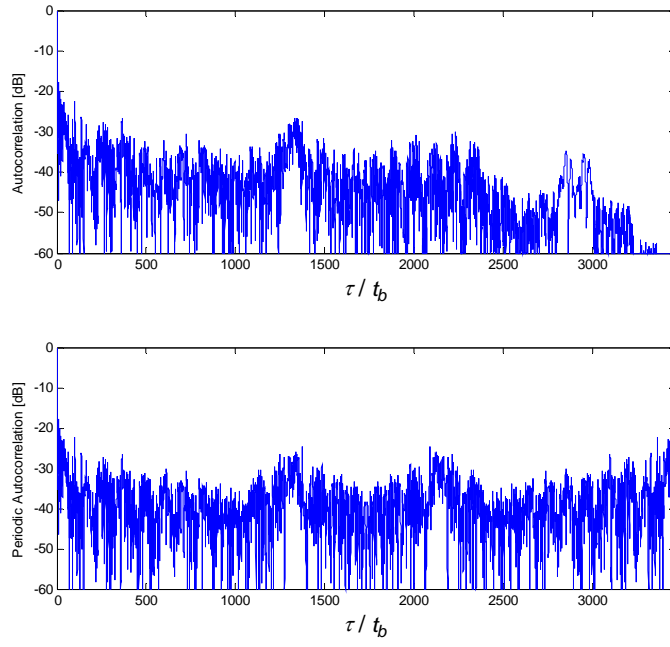
Figure 53.   DFC 32 Code 1 ACF (top) and PACF (bottom).
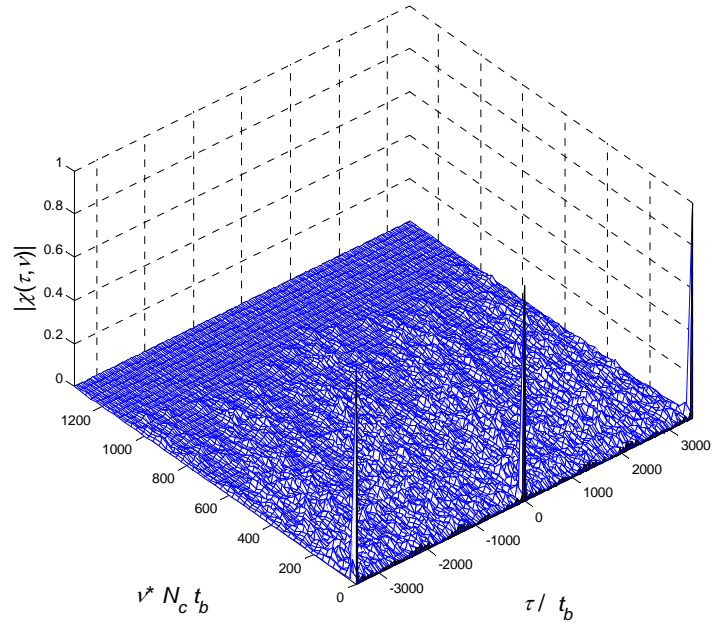
Figure 54.   DFC 32 Code 1 Periodic Ambiguity Function Plot.

To illustrate the non-interfering nature of the DFC 32 signal the CCF was applied to all three possible combinations of signals that would be utilized by a networked LPI radar system with three nodes. Each radar would be transmitting its own code set. Theoretically there would be no interference between each different code sets using similar signal parameters. Figure 55 shows the CCF for the DFC 32 code set #1 and code set #2 on the left contrasted with the ACF of DFC 32 code set #1 on the right. Figure 56 shows the CCF for the DFC 32 code set #2 and code set #3 on the left contrasted with the ACF of DFC 32 code set #2 on the right. Figure 57 shows the CCF for the DFC 32 code set #3 and code set #1 on the left contrasted with the ACF of DFC 32 code set #3 on the right.
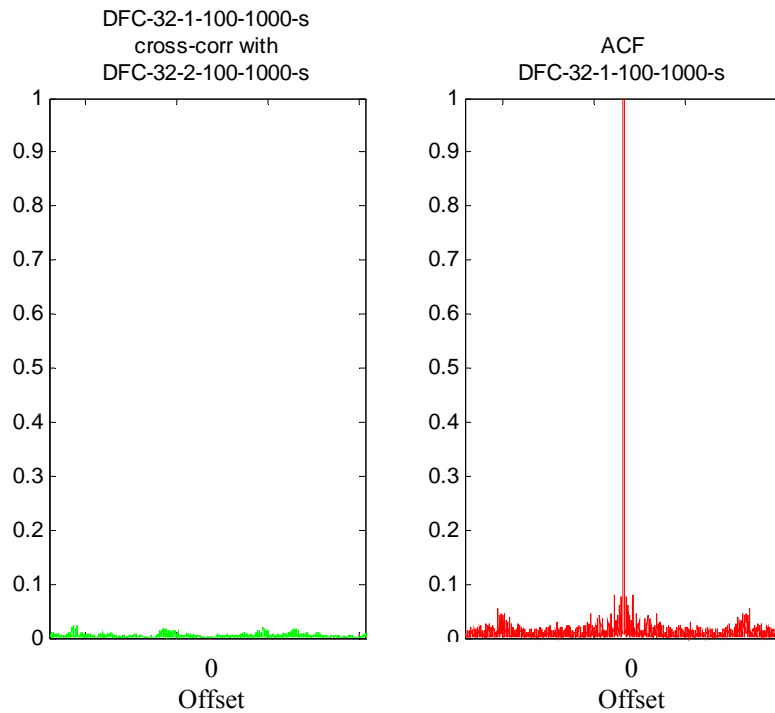
Figure 55.   DFC 32 Codes 1 and 2 CCF Plot (Left) and Code 1 ACF Plot (Right).
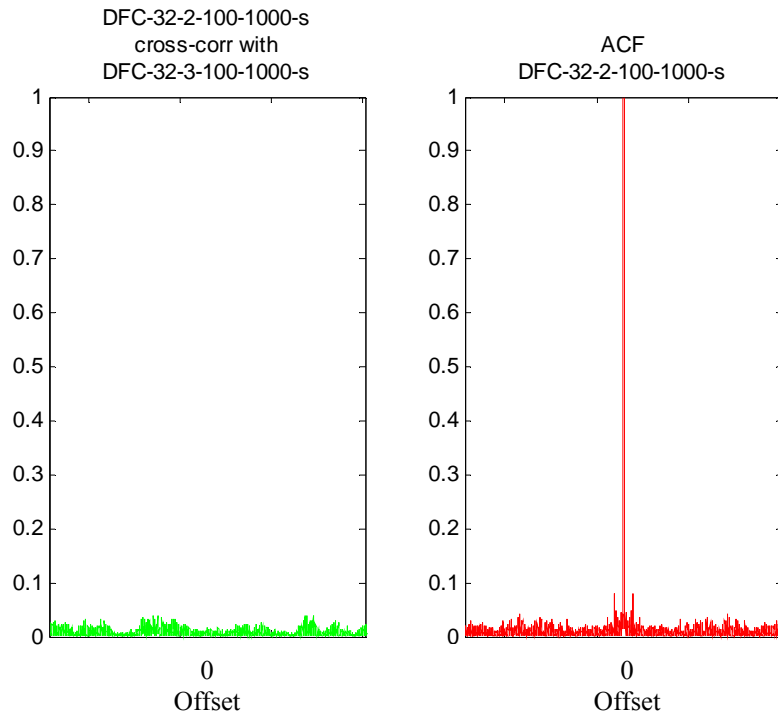
Figure 56.   DFC 32 Codes 2 and 3 CCF Plot (Left) and Code 2 ACF Plot (Right).
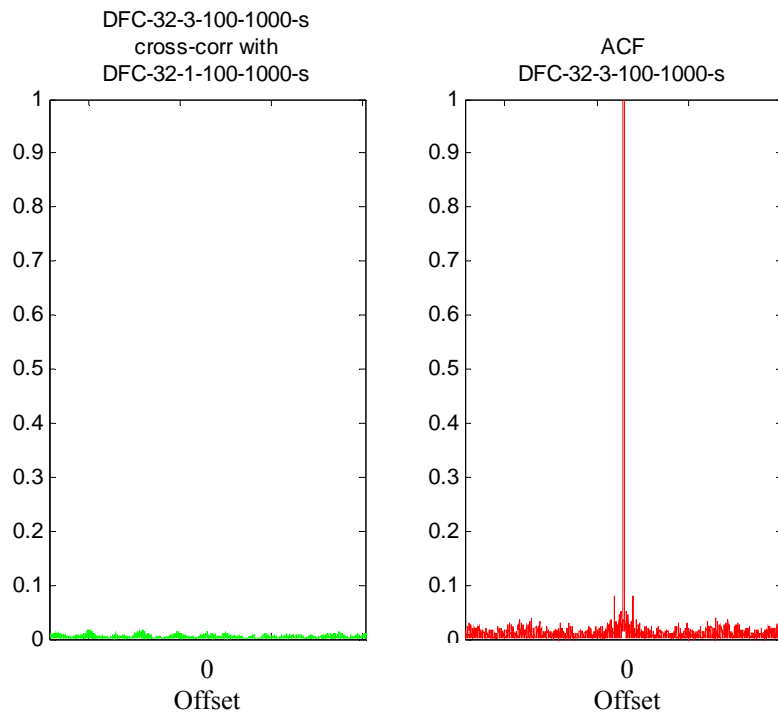
Figure 57.   DFC 32 Codes 3 and 1 CCF Plot (Left) and Code 3 ACF Plot (Right).

C.   SUMMARY

In summary, Table 9 shows the PSL for each of the codes examined in this chapter. In the next chapter, the codes generated will be analyzed using time-frequency and bi-frequency techniques to extract the signal parameters.

Code	N_c/N_F	PSL (dB)
OPS	40	−16
OPS	128	−21
Optimized OPS	40	−17
DFC	32	−20

Table 9.   PSL of Orthogonal Codes.

THIS PAGE INTENTIONALLY LEFT BLANK

IV. WAVEFORM PARAMETER EXTRACTION TECHNIQUES

A. WIGNER-VILLE DISTRIBUTION

1. Introduction

The first waveform analysis performed on the signals was the Wigner-Ville Distribution (WVD) analysis. This analysis was first introduced by Wigner. The process was introduced separately by Ville. We use the WVD to produce the time-frequency analysis that enables the extraction of the LPI signal parameters. These time-frequency plots are also used to identify the modulation types. This is accomplished by sending a portion of the received signal through a bank of kernel functions. The length of the kernel function bank is determined by selecting the correct window length that provides the right balance of time-frequency resolution, but also stays within the computational limits of the system. The Fourier transform is taken of the kernel output to yield the frequency portion of the plot.

This analysis contains "cross terms," which are unintended constructive interference patterns that result from the presence of two signals. The locations of the interference patterns are desirable for signal analysis and carrier frequency identifications. The graphics are in three dimensions (time, frequency, and magnitude) or they can be displayed in a two dimensional format of time versus frequency with a color scheme used to show relative magnitude differences. With these plots, the modulation period, center frequency, and time/frequency resolutions are clearly identifiable [1].

2. LPI Waveform Parameter Extraction Capability

a. Orthogonal Polyphase Sequence of 40 Sub-codes

The WVD time-frequency image of the OPS 40 signal code set #1 with a center frequency of 1 kHz and bandwidth of 1 kHz is shown in Figure 58 (see Table 2). The WVD marginal frequency domain image Hz is shown in Figure 59. In the marginal

frequency domain image, the center frequency is readily apparent. In addition, the bandwidth of the signal can also be estimated.
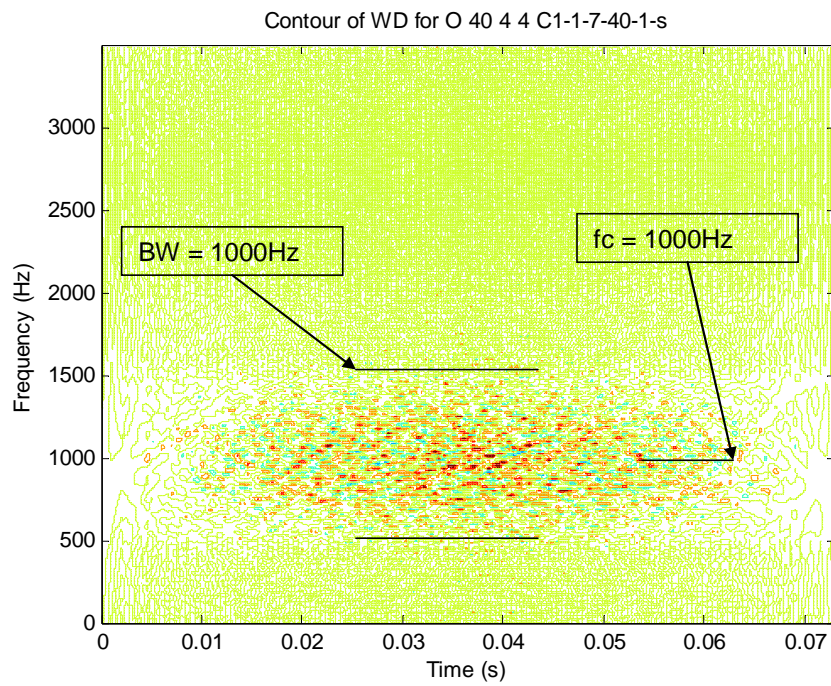
Figure 58.   Time Frequency WD Plot OPS 40 Code 1.
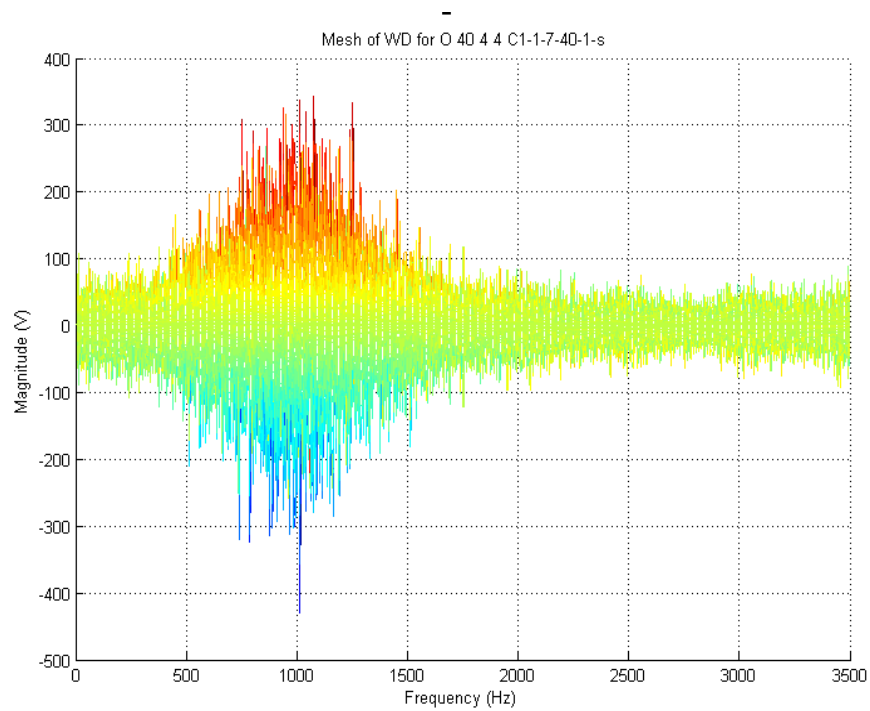
Figure 59.   Marginal Frequency Domain Plot OPS 40 Code 1.

b. Orthogonal Polyphase Sequence of 128 Sub-codes

The WVD time-frequency image of the OPS 128 signal code set #1 with a center frequency of 1 kHz and bandwidth of 1 kHz is shown in Figure 60 (see Table 4). The WVD marginal frequency domain image is shown in Figure 61. In the marginal frequency domain image, the center frequency is readily apparent. In addition, the bandwidth of the signal can also be estimated.
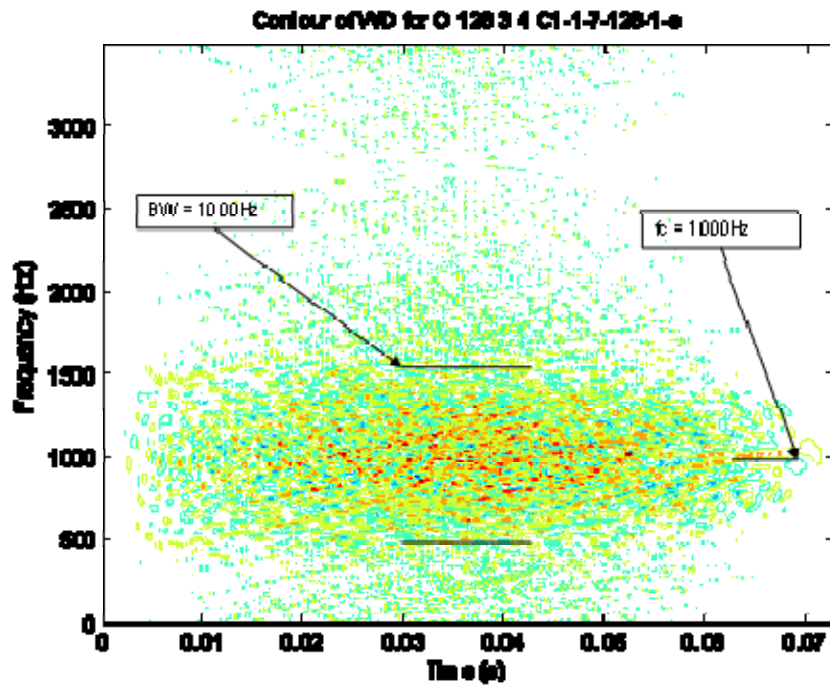
Figure 60.   Time Frequency WD Plot OPS 128 Code 1.
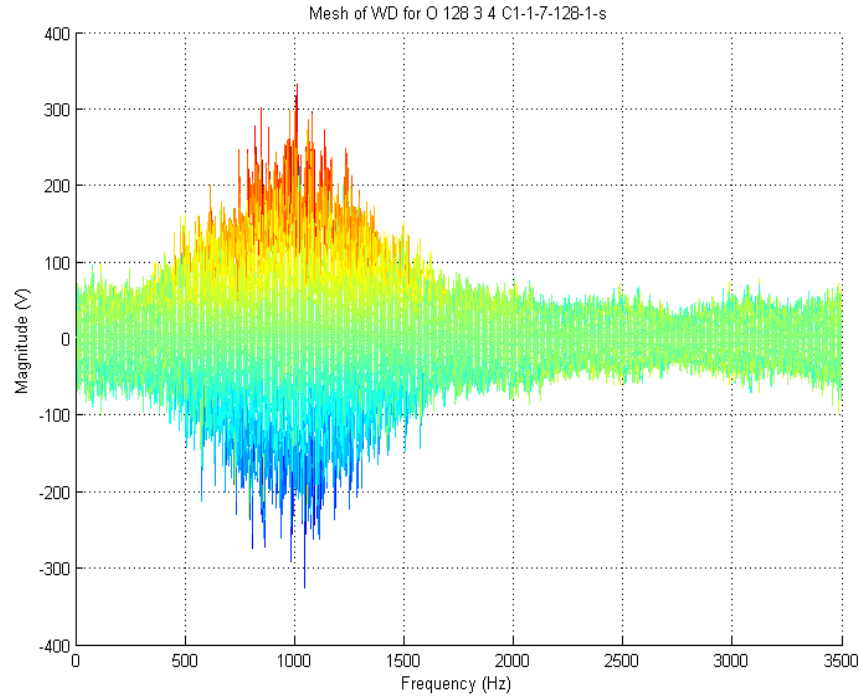
Figure 61.   Marginal Frequency Domain Plot OPS 128 Code 1.

c.   *Optimized Orthogonal Polyphase Sequence*

The WVD time-frequency image of the Optimized OPS 40 signal code set #1 with a center frequency of 1 kHz and bandwidth of 1 kHz is shown in Figure 62 (see Table 6). There is an identifiable pattern on the slope of half of the bandwidth (BW) over half of the code period (T). The WVD marginal frequency domain image is shown in Figure 63.

72
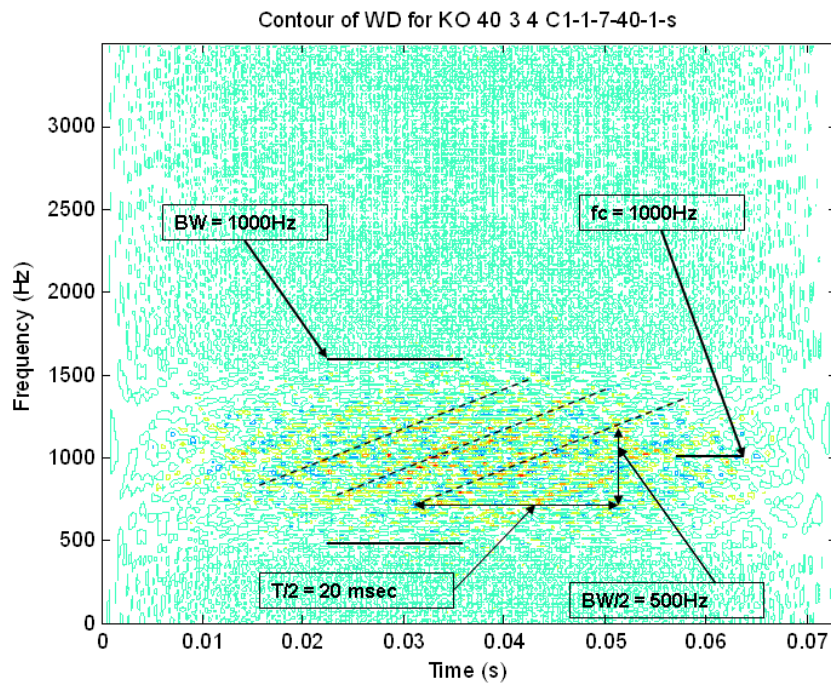
Figure 62.   Time Frequency WD Plot Optimized OPS 40 Code 1.
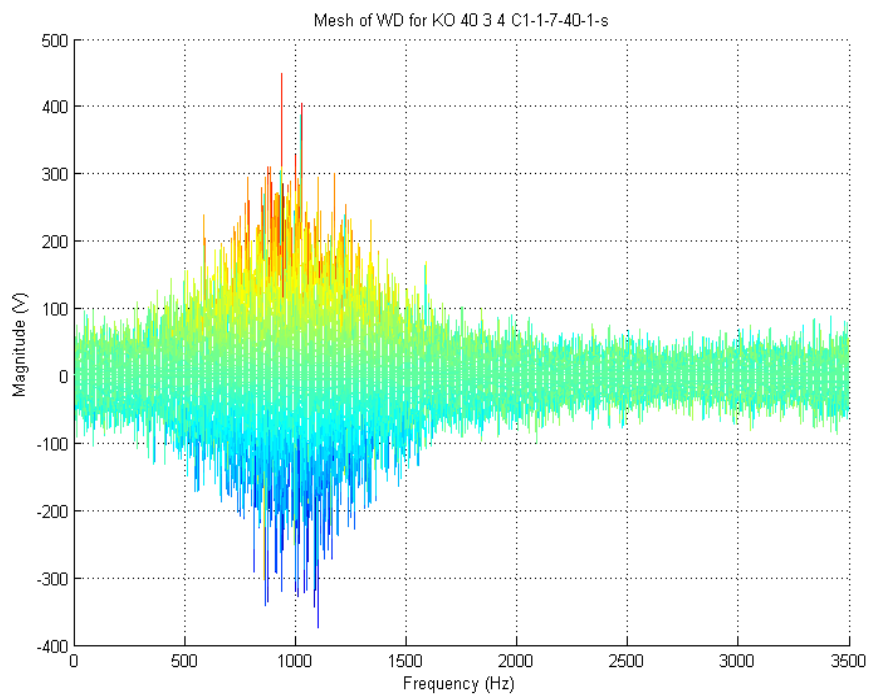
Figure 63.   Marginal Frequency Domain Plot Optimized OPS 40 Code 1.

d.   Discrete Frequency Coding

The WVD time-frequency image of the DFC 32 signal code set #1 with $N_F = 32$, base frequency is $f = 1\,\text{kHz}$, $f_s = 100\,\text{kHz}$, and $t_p = 0.001$ s is shown in Figure 64 (note the reversal of the time axis). The WVD marginal frequency domain image of the DFC 32 signal code set #1 is shown in Figure 65. The WVD images yield few details about the DFC 32 signal. The frequencies can be identified (see Table 8, Code 1) up until the point where the actual frequency values are masked by the cross terms.
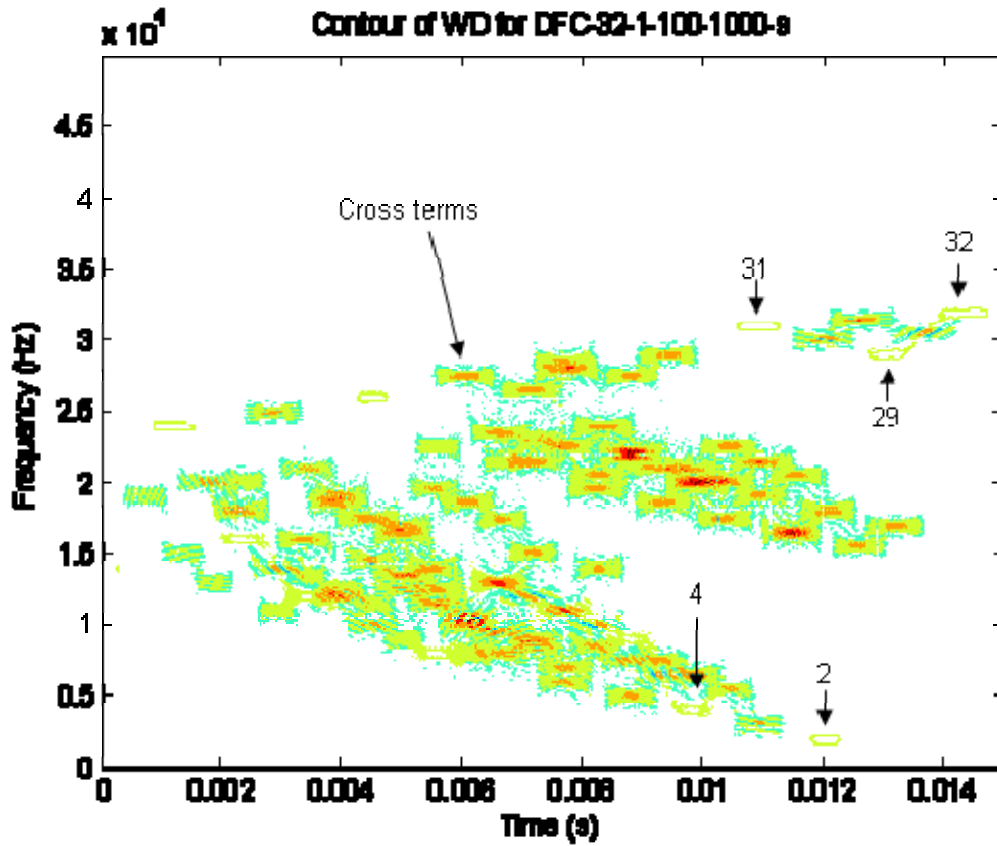
Figure 64.   Time Frequency WD Plot DFC 32 Code 1.
Note the first five frequency multiplier terms (from Table 8) in reverse order.
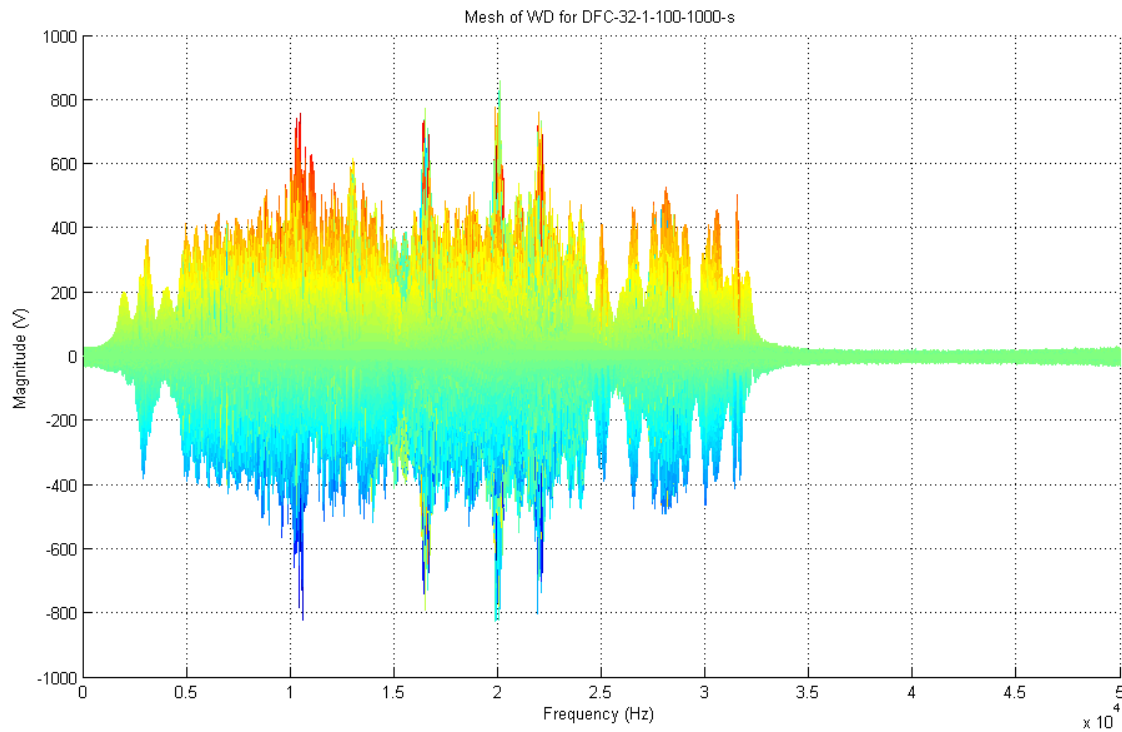
Figure 65.   Marginal Frequency Domain Plot DFC 32 Code 1.

3.   Conclusions

The WVD process appears to provide some signal extraction capabilities against the OPS signals. In all OPS simulations center frequency was readily apparent. The DFC signal's parameters were nearly impossible to extract with the WVD process. Due to the high number of frequencies in the sequence the WVD process was able to identify patterns created by the waveform, but useful parameter extraction could not be performed.

B.   QUADRATURE MIRROR FILTER BANK ANALYSIS

1.   Introduction

The second waveform technique used on the LPI waveforms was the Quadrature Mirror Filter Bank (QMFB) analysis. This analysis uses a tree of wavelet filters to dissect the incoming LPI signal into a series of time-frequency layers. The lower layers have small time resolution, but large frequency resolution. The upper layers have the

opposite characteristics with large time resolution, but small frequency resolution. The simultaneous analysis of multiple layers allows for a very accurate depiction of the characteristics of the LPI signal. The decomposition of the received signal is best looked at as a myriad of bandpass filters called wavelets that are used to break up the signal into smaller pieces that are better for analysis. This is accomplished by using a standard wavelet as the basis function and then translating, dilating, or contracting the wavelet as necessary to achieve the desired time and frequency resolution. The signal parameters are graphically displayed in time-frequency plots that have color schemes to identify centers of concentrated signal energy. The QMFB has the advantage over WVD and Cyclostationary Spectral Analysis (CSA) because it has no cross terms that adds noise to the signal and could possibly obscure extraction of its parameters. The output graphics are used to identify modulation period, center frequency, signal bandwidth, code period, and in some cases the phase shift [1].

2. LPI Waveform Parameter Extraction Capability

a. Orthogonal Polyphase Sequence of 40 Sub-codes

The fourth layer of the QFMB time-frequency plane of the OPS 40 signal code set #1 with a center frequency of 1 kHz and bandwidth of 1 kHz is shown in Figure 66 (see Table 2). Five periods are captured. The repetitive nature of the polyphase sequence and the center frequency are obvious as shown in Figure 66. A close up of the fourth layer of the QFMB time-frequency plane of the same OPS 40 signal is shown in Figure 67. The code period is readily apparent in this view.
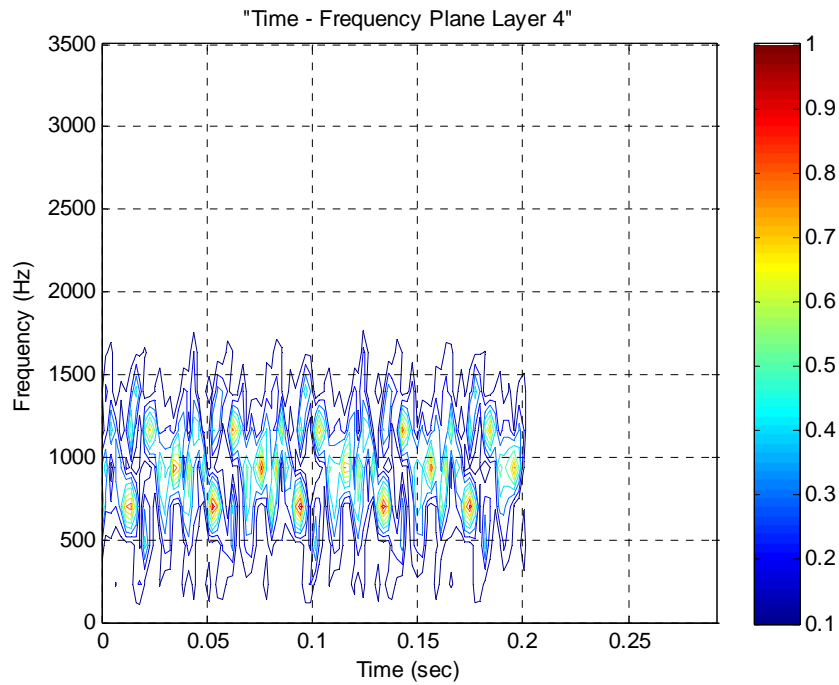
Figure 66.   QMFB Layer 4 of OPS 40 Code 1 showing all five code periods.
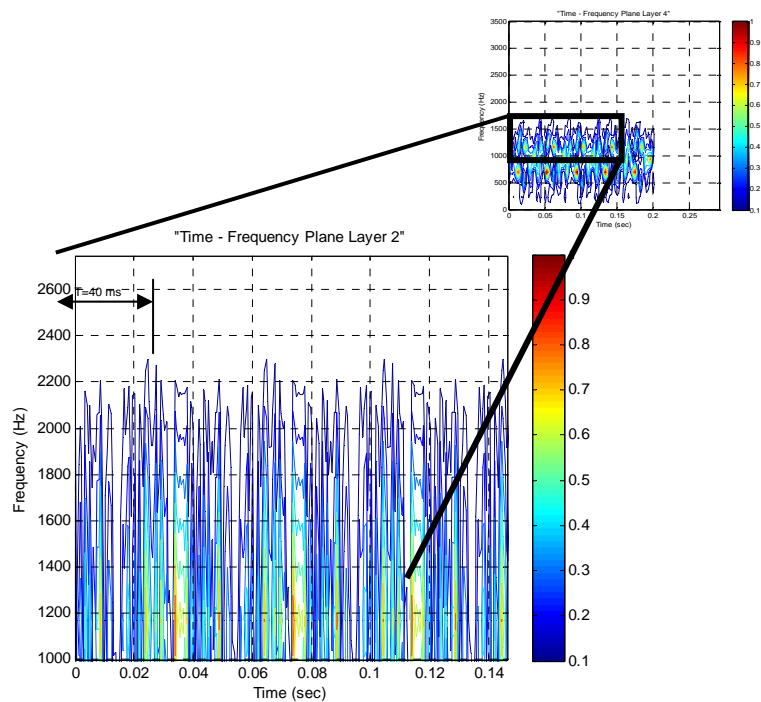
Figure 67.   QMFB Layer 2 of OPS 40 Code 1 with code period T = 40 ms.

b.   *Orthogonal Polyphase Sequence of 128 Sub-codes*

The fourth layer of the QFMB time-frequency plane of the OPS 128 signal code set #1 with a center frequency of 1 kHz and bandwidth of 1 kHz is shown in Figure 68 (see Table 4).   Five periods are captured.   The repetitive nature of the polyphase sequence and the center frequency are obvious in Figure 68.   A close up of the fourth layer of the QFMB time-frequency plane of the same OPS 128 signal is shown in Figure 69. The code period is readily apparent in this view.
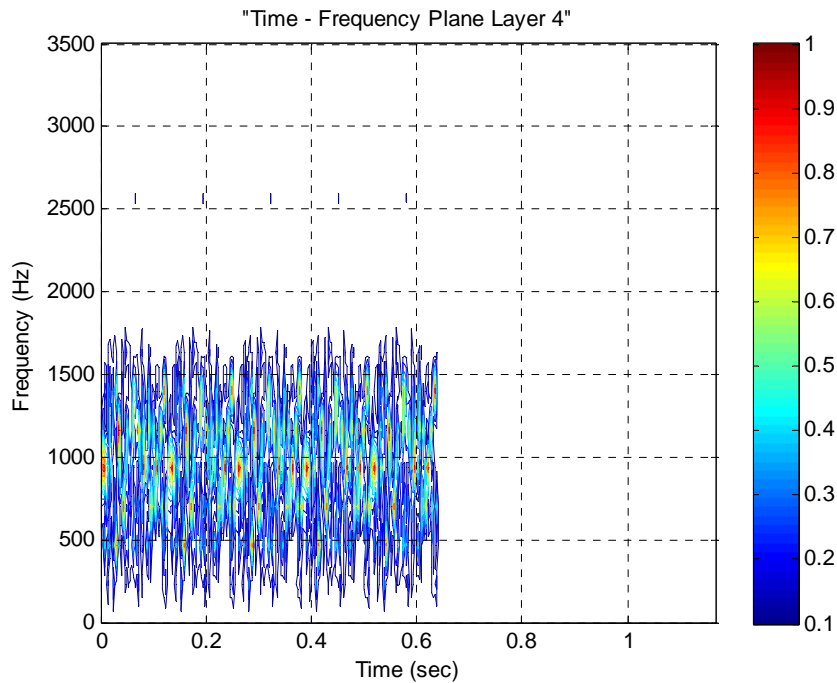
Figure 68.   QMFB Layer 4 of OPS 128 Code 1 showing all five code periods.
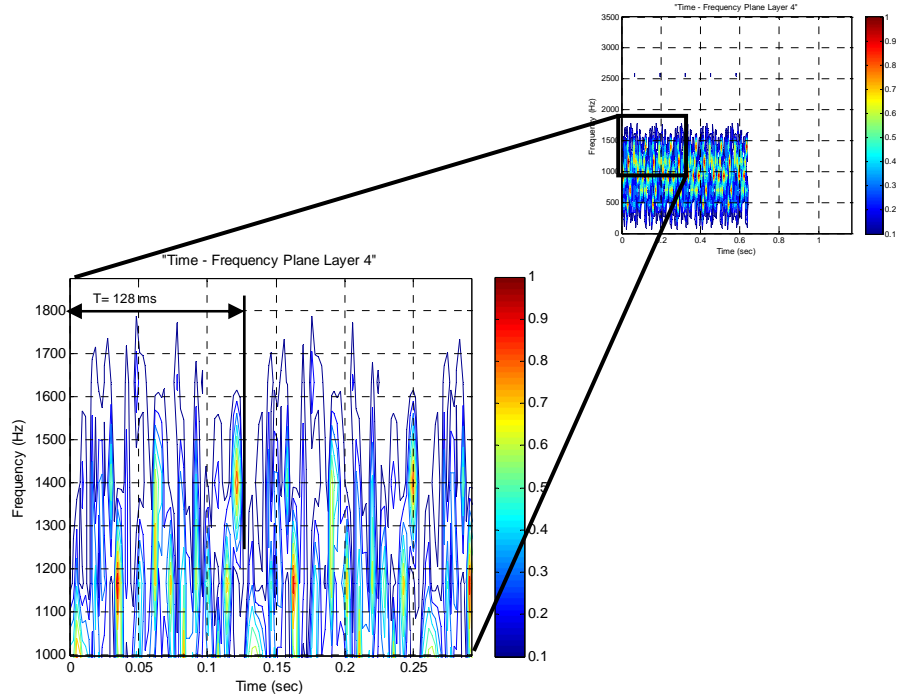
Figure 69.   QMFB Layer 4 of OPS 128 Code 1 showing code period T = 128 ms.

c.   *Optimized Orthogonal Polyphase Sequence*

The fourth layer of the QFMB time-frequency plane of the Optimized OPS 40 signal code set #1 with a center frequency of 1 kHz and bandwidth of 1 kHz is shown in Figure 70 (see Table 6). Five periods are captured. The repetitive nature of the polyphase sequence and the center frequency are obvious in Figure 70. A close up of the fourth layer of the QFMB time-frequency plane of the same Optimized OPS 40 signal is shown in Figure 71. The code period is readily apparent in this view.
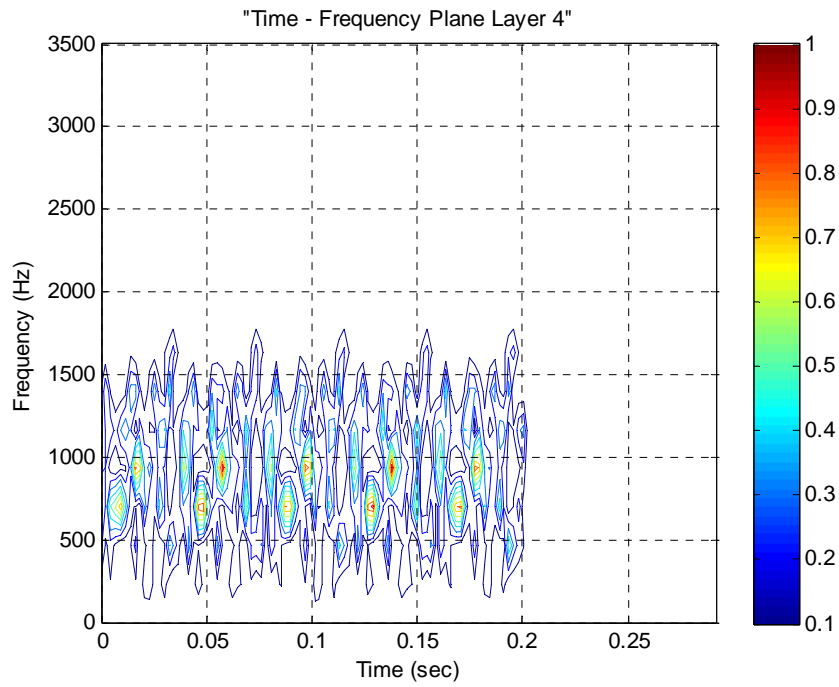
Figure 70.   QMFB Layer 4 of Optimized OPS 40 Code 1 all five code periods.
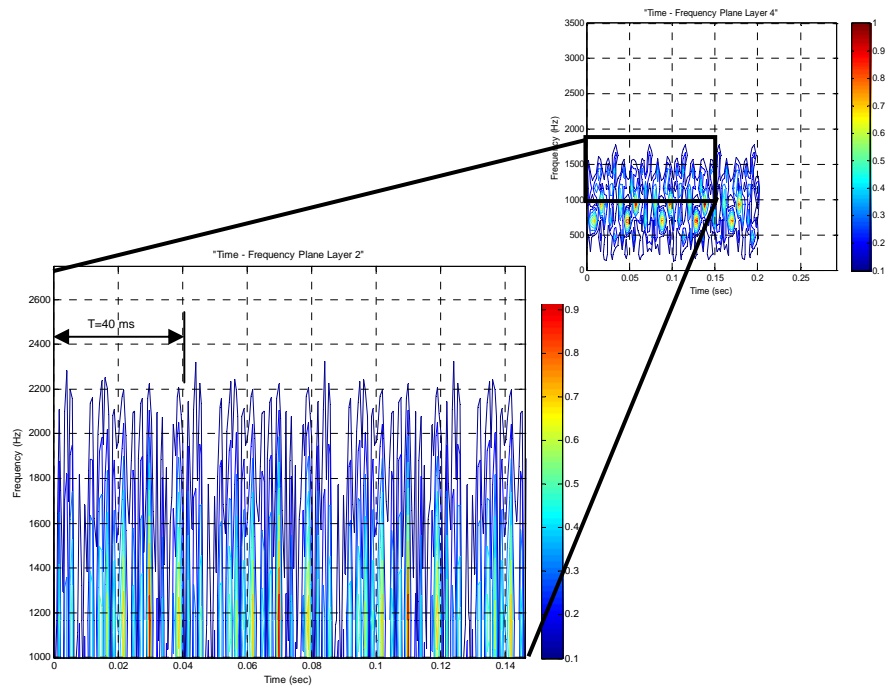
Figure 71.   QMFB Layer 2 of Optimized OPS 40 Code 1 code period T = 40 ms.

d. *Discrete Frequency Coding*

The fifth layer of the QFMB time-frequency plane of the DFC 32 signal code set #1 is shown in Figure 72 (see Table 8). A close up of the fifth layer of the QFMB time-frequency plane of the same DFC 32 signal is shown in Figure 73. The frequency duration is discernable in this view and the frequency values proportional to the original code set can be determined. QMFB presents a clearer view of frequency duration and frequency value than WVD.
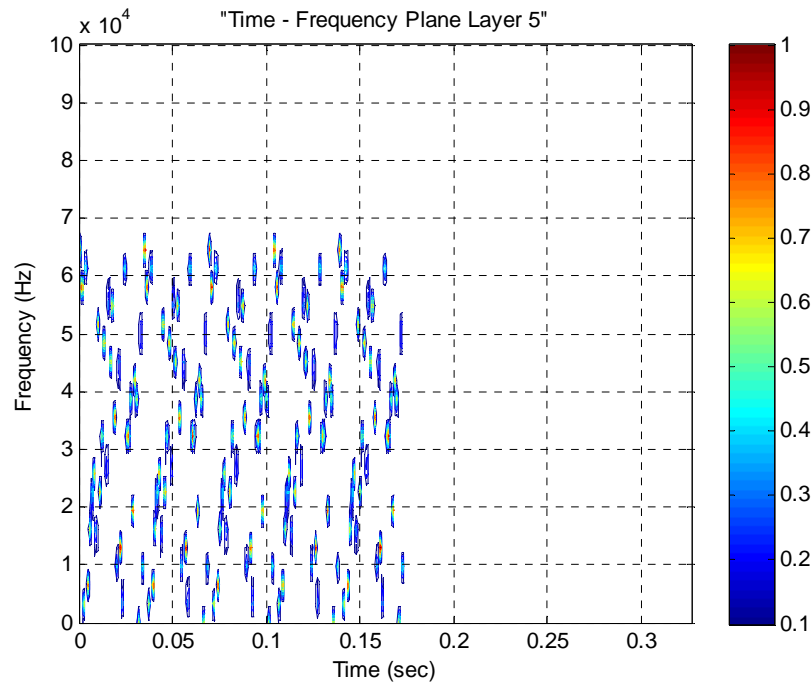
Figure 72.   QMFB Layer 5 of DFC 32 Code 1.
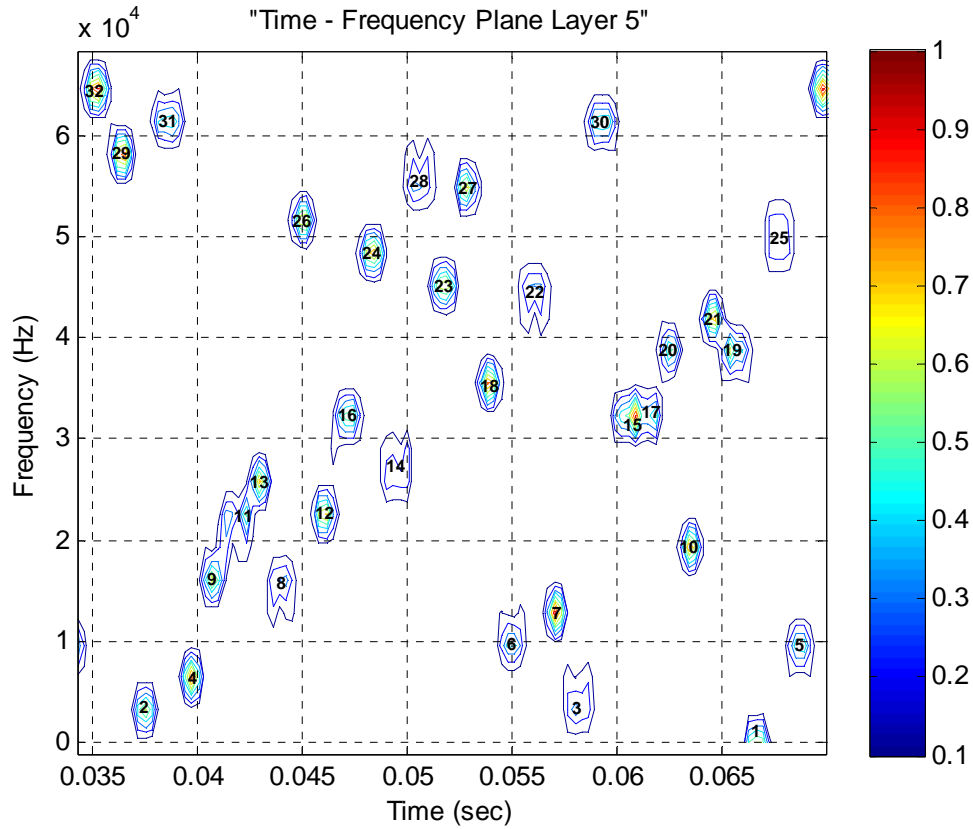
Figure 73.   The First Period of QMFB Layer 5 of DFC 32 Code 1.

3.   Conclusions

QMFB showed some potential for parameter extraction of the OPS code.   The code period was identifiable utilizing QMFB under no noise simulations as well as an estimate of center frequency.   The QMFB process performed on the DFC signal revealed that a frequency hopper was being utilized, and the extraction of the sequence is made possible by this method.   In addition, with a close in view the frequency duration could be determined.

C. CYCLOSTATIONARY SPECTRAL ANALYSIS

1. Introduction

The third waveform analysis technique used on the LPI signals was the Cyclostationary Spectral Analysis (CSA). The main premise of CSA is the analysis of the received signal using a different less traditional approach. Both WVD and QMFB viewed parameter extraction from a time-frequency point of view. CSA uses a frequency versus cycle frequency format in order to provide an additional capability for LPI signal analysis. This bi-frequency analysis is obtained through using Fast Fourier Transforms (FFT) to manipulate the ACF into a cyclic autocorrelation function (CACF). The Fourier transform is applied to the CACF to produce the CSA. The CSA can be found with either a time-smoothing FFT Accumulation Method (FAM) or a Direct Frequency-Smoothing Method (DFSM). The FAM uses many smaller calculations that produce a more timely analysis of the signal. DFSM is more computationally intensive and relies on spectral-correlation operations. The plots generated are used to identify center frequency, signal bandwidth, and code rate [1]. For consistency all CSA was conducted selecting a frequency resolution of 128 Hz and a df/dα (M) of 2.

2. LPI Waveform Parameter Extraction Capability

a. *Orthogonal Polyphase Sequence of 40 subcodes*

The frequency smoothing spectral correlation density (SCD) of the OPS 40 signal code set #1 with a center frequency of 1 kHz and bandwidth of 1 kHz is shown in Figure 74. A closer look, shown in Figure 75, at a single modulation quadrant reveals additional signal structure. The time smoothing spectral correlation density (SCD) of the OPS 40 signal code set #1 with a center frequency of 1 kHz and bandwidth of 1 kHz is shown in Figure 76. A closer look, shown in Figure 77, at a single modulation quadrant reveals additional signal structure.

Frequency Smoothing SCD O 40 4 4 C1-1-7-40-1-s, df = 128, N = 128
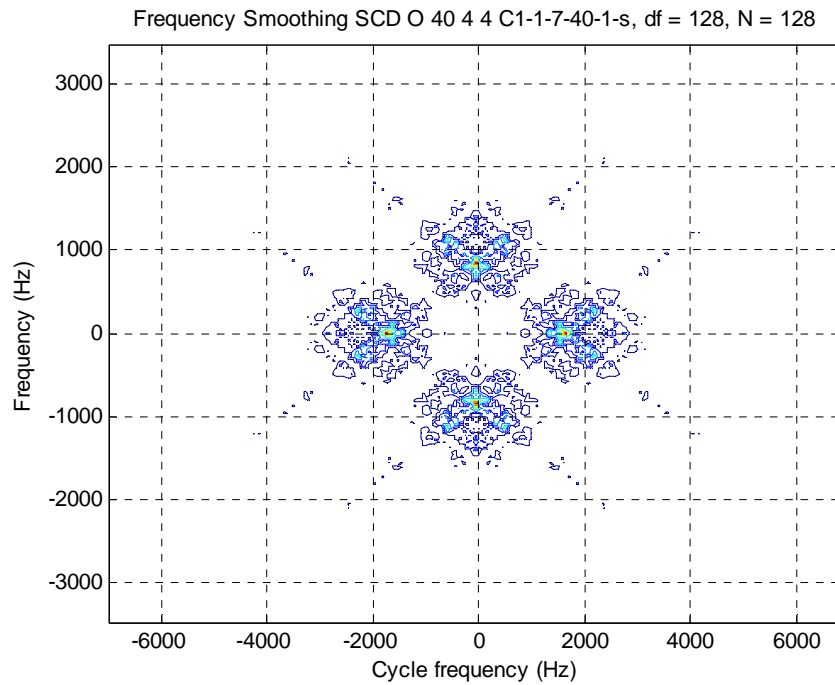
Figure 74.   DFSM of OPS 40 Code 1 with T = 40 ms and B = 1000 Hz.
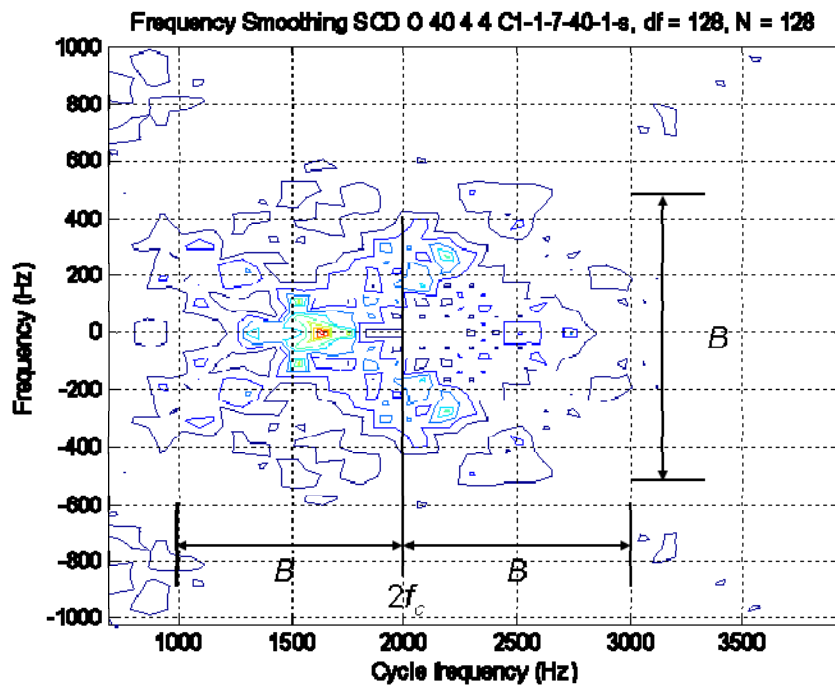
Figure 75.   DFSM of OPS 40 Code 1 with T = 40 ms and B = 1000 Hz Individual Modulation Quadrant.
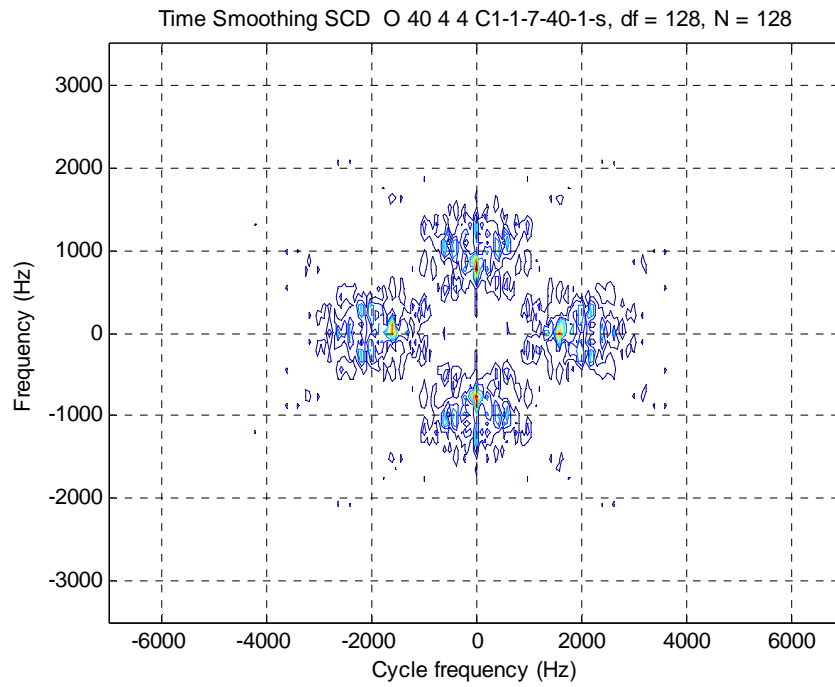
Figure 76.   FAM of OPS 40 Code 1 with T = 40 ms and B = 1000 Hz.
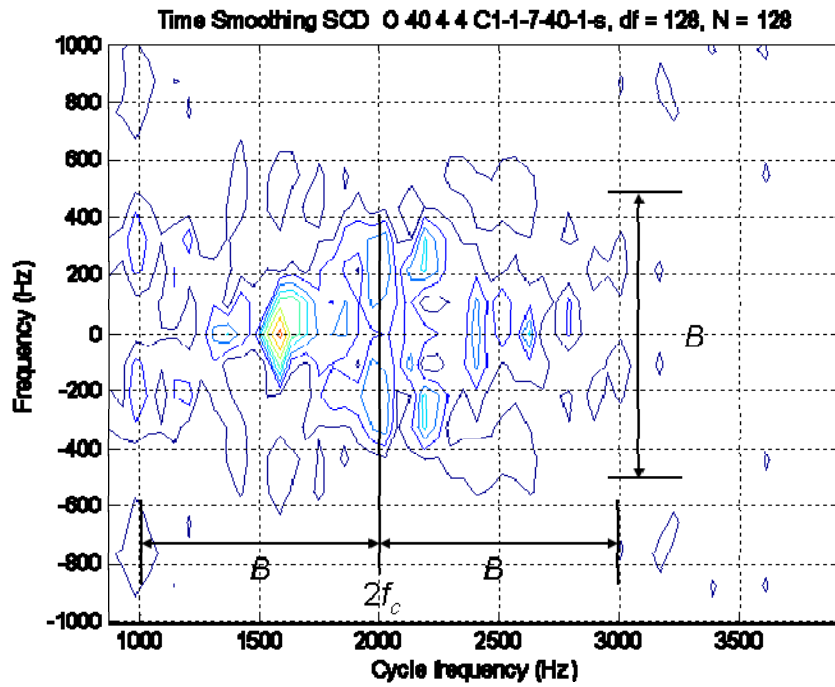
Figure 77.   FAM of OPS 40 Code 1 with T = 40 ms and B = 1000 Hz Individual
Modulation Quadrant.

b. Orthogonal Polyphase Sequence of 128 Sub-codes

The frequency smoothing spectral correlation density (SCD) of the OPS 128 signal code set #1 with a center frequency of 1 kHz and bandwidth of 1 kHz is shown in Figure 78. The center frequency can be observed in Figure 78. A closer look, shown in Figure 79, at a single modulation quadrant reveals additional signal structure. The time smoothing spectral correlation density (SCD) of the OPS 128 signal code set #1 with a center frequency of 1 kHz and bandwidth of 1 kHz is shown in Figure 80. A closer look, shown in Figure 81, at a single modulation quadrant reveals additional signal structure.
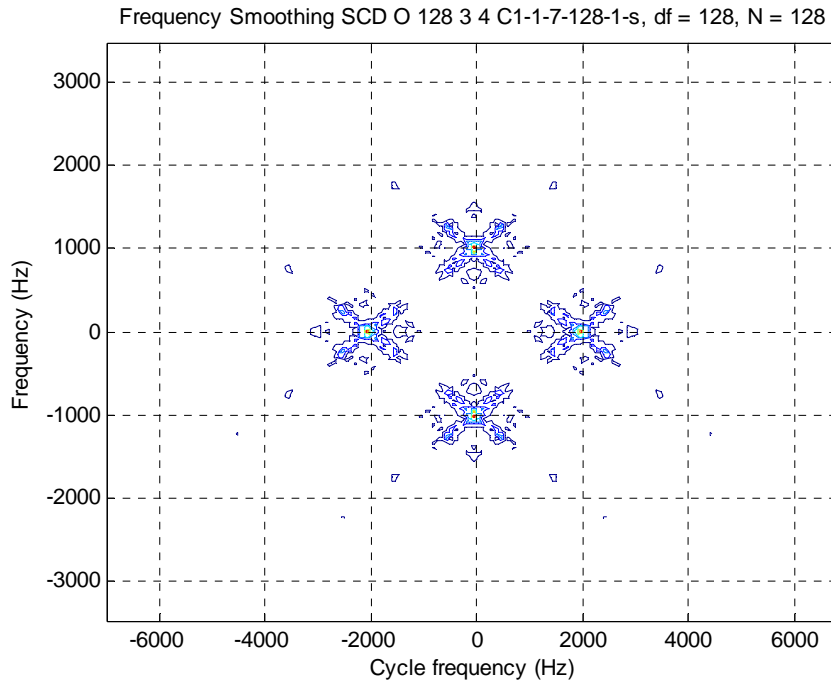
Figure 78.   DFSM of OPS 128 Code 1 with T = 128 ms and B = 1000 Hz.
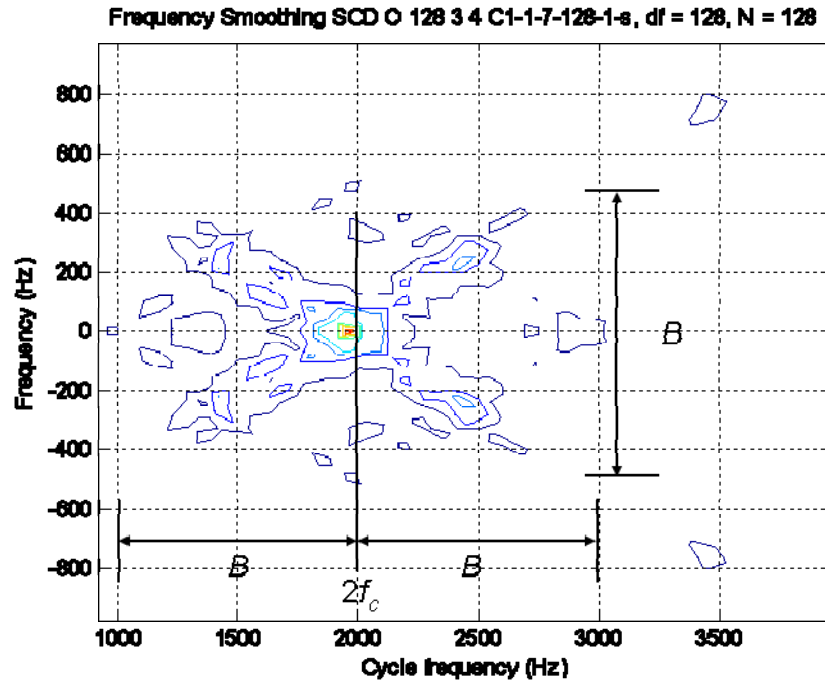
Figure 79.   DFSM of OPS 128 Code 1 with T = 128 ms and B = 1000 Hz Individual
Modulation Quadrant.
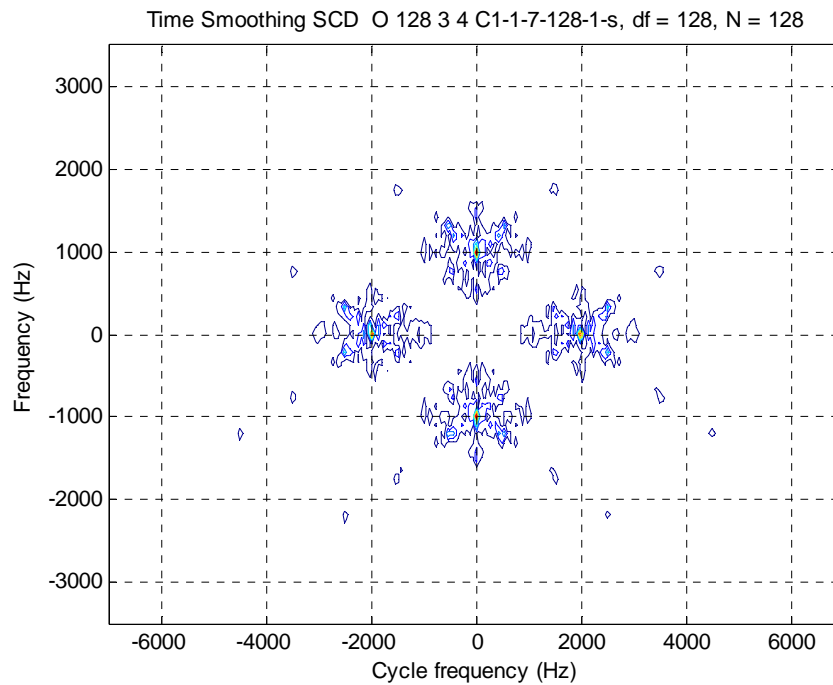
Figure 80.   FAM of OPS 128 Code 1 with T = 128 ms and B = 1000 Hz.
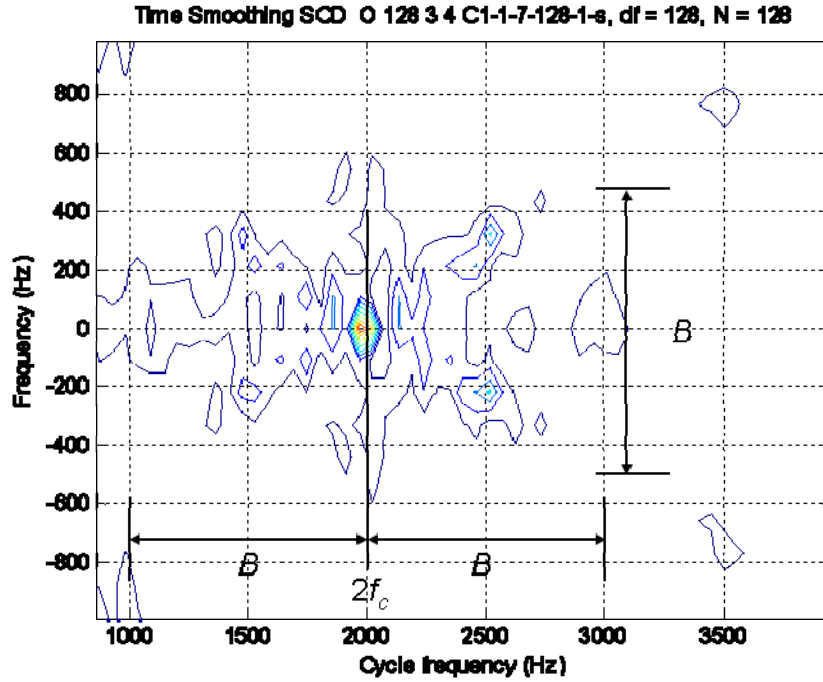
Figure 81. FAM of OPS 128 Code 1 with T = 128 ms and B = 1000 Hz Individual Modulation Quadrant.

c. *Optimized Orthogonal Polyphase Sequence*

The frequency smoothing spectral correlation density (SCD) of the Optimized OPS 40 signal code set #1 with a center frequency of 1 kHz and bandwidth of 1 kHz is shown in Figure 82. The center frequency can be observed in Figure 82. A closer look, shown in Figure 83, at a single modulation quadrant reveals additional signal structure. The time smoothing spectral correlation density (SCD) of the Optimized OPS 40 signal code set #1 with a center frequency of 1 kHz and bandwidth of 1 kHz is shown in Figure 84. A closer look at a single modulation quadrant as shown in Figure 85 reveals additional signal structure. The energy centers present indicate a distinct linear modulation that is present in orthogonal waveforms.

Frequency Smoothing SCD KO 40 3 4 C1-1-7-40-1-s, df = 128, N = 128
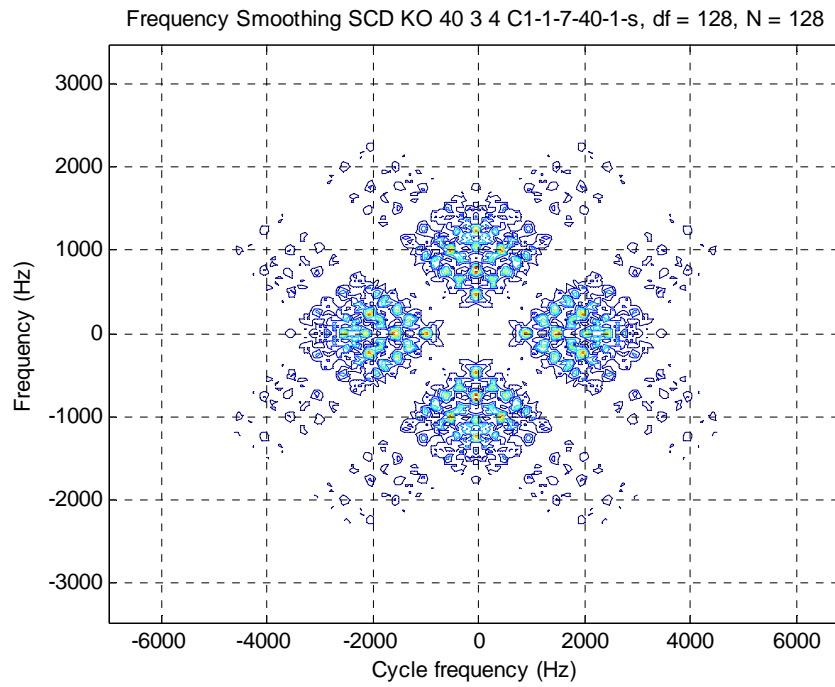
Figure 82.   DFSM of Optimized OPS 40 Code 1 with T = 40 ms and B = 1000 Hz.

Frequency Smoothing SCD KO 40 3 4 C1-1-7-40-1-s, df = 128, N = 128
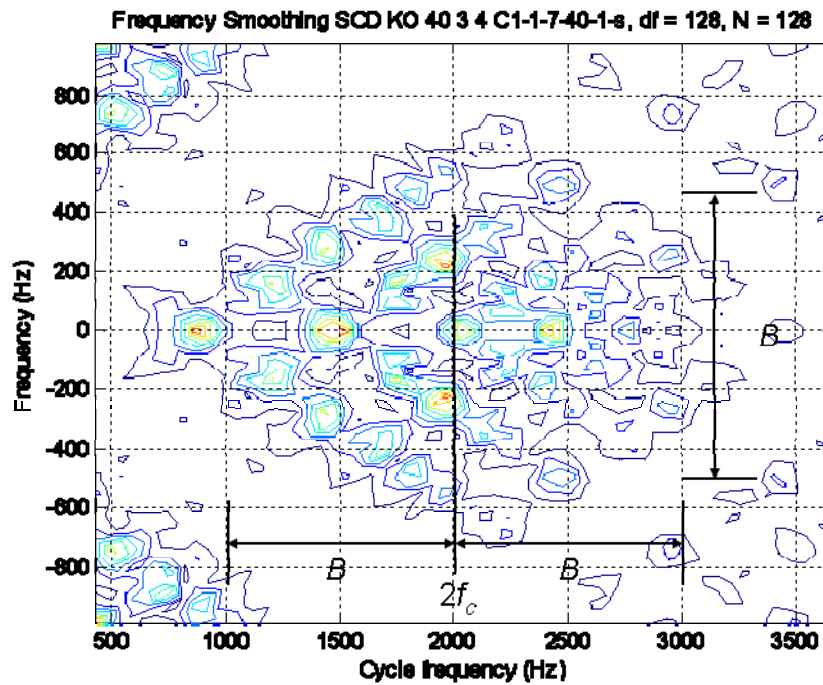
Figure 83.   DFSM of Optimized OPS 40 Code 1 with T = 40 ms and B = 1000 Hz
Individual Modulation Quadrant.

Time Smoothing SCD KO 40 3 4 C1-1-7-40-1-s, df = 128, N = 128
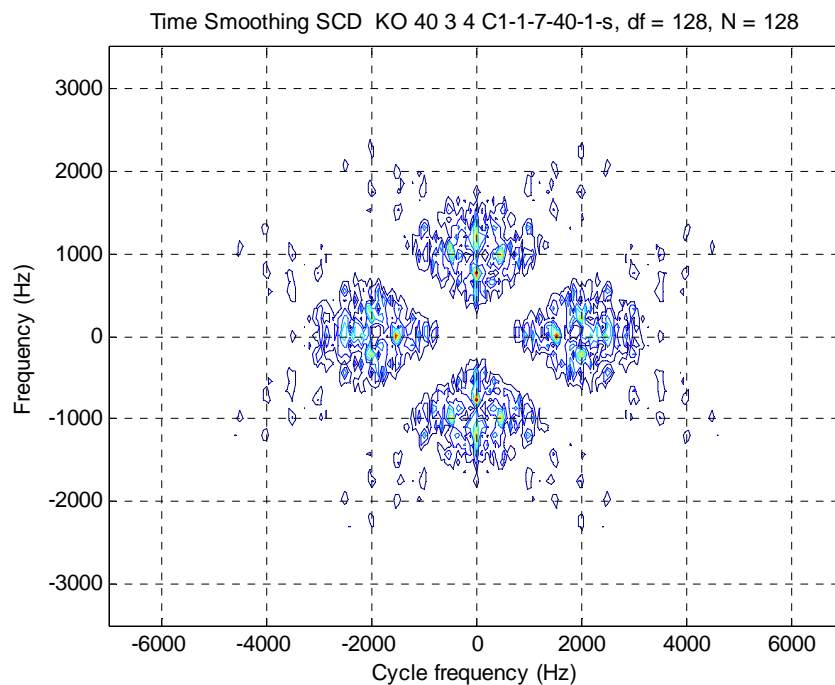
Figure 84.   FAM of Optimized OPS 40 Code 1 with T = 40 ms and B = 1000 Hz.
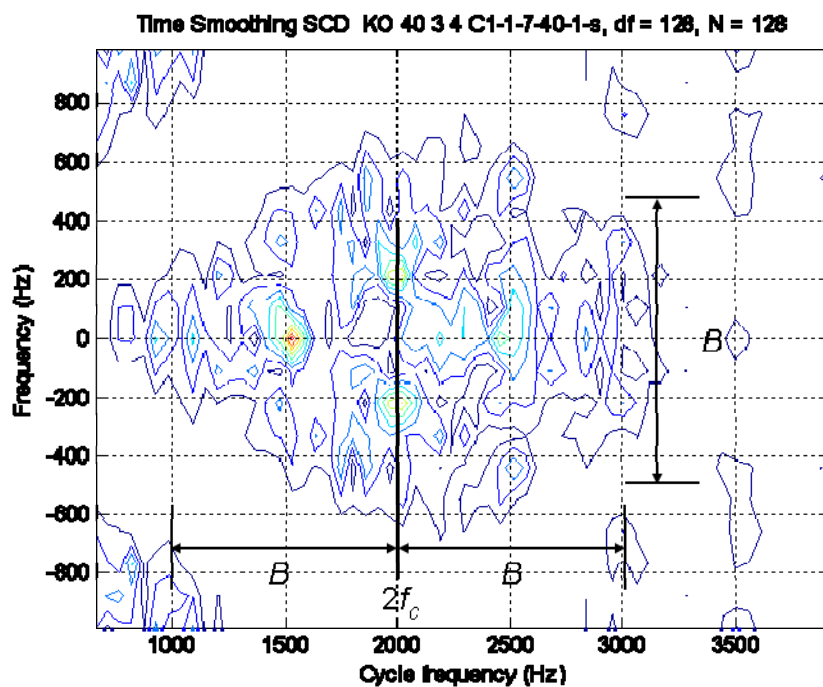
Figure 85.   FAM of Optimized OPS 40 Code 1 with T = 40 ms and B = 1000 Hz
Individual Modulation Quadrant.

90

d. Discrete Frequency Coding

The frequency smoothing spectral correlation density (SCD) of the DFC 32 signal code set #1 is shown in Figure 86. A closer look, shown in Figure 87, at a single modulation quadrant reveals additional signal structure. The time smoothing spectral correlation density (SCD) of the DFC 32 signal code set #1 is shown in Figure 88. A closer look, shown in Figure 89, at a single modulation quadrant reveals additional signal structure. For CSA on the DFC32 signal the base frequency was reduced to 50 Hz and the sampling frequency was reduced to 5 kHz.
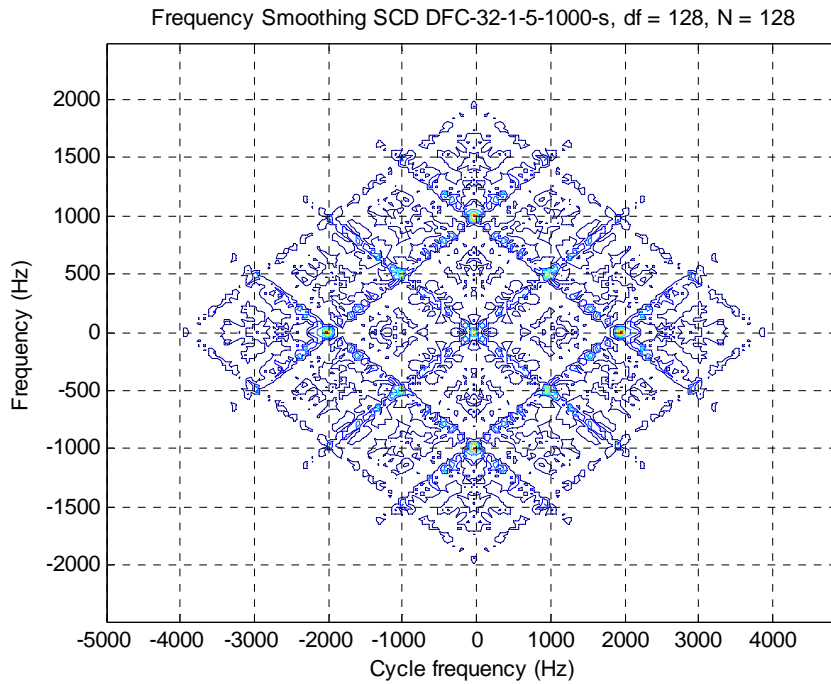
Figure 86.   DFSM of DFC 32 Code 1 with $f = 1000$ Hz.
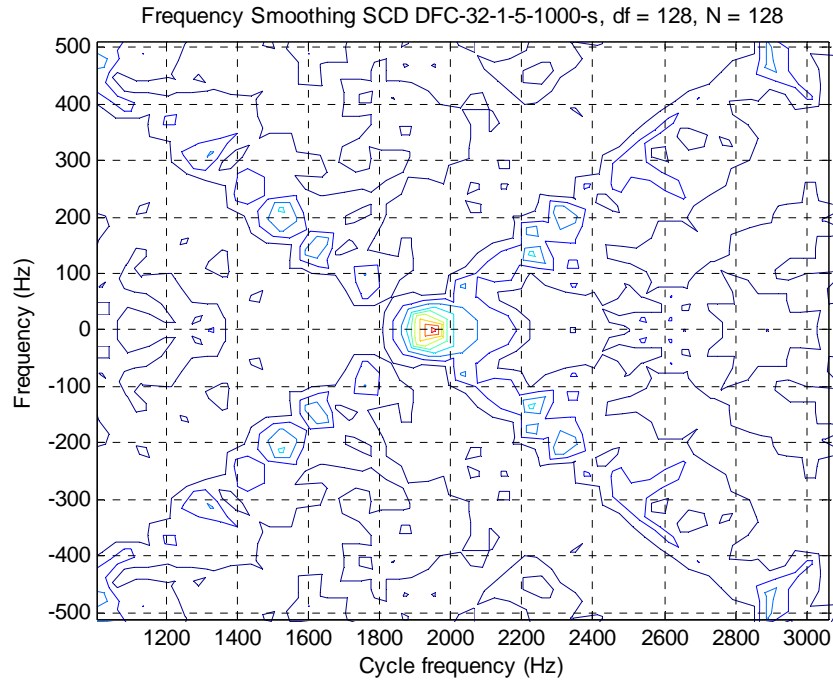
Figure 87. DFSM of DFC 32 Code 1 with $f = 1000$ Hz Individual Modulation Quadrant.
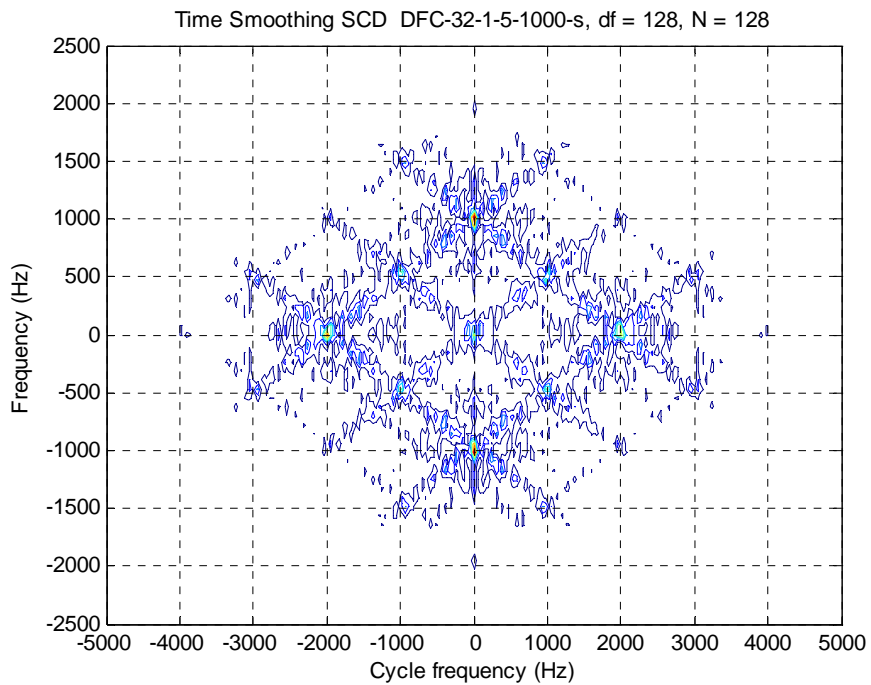
Figure 88. FAM of DFC 32 Code 1 with $f = 1000$ Hz.
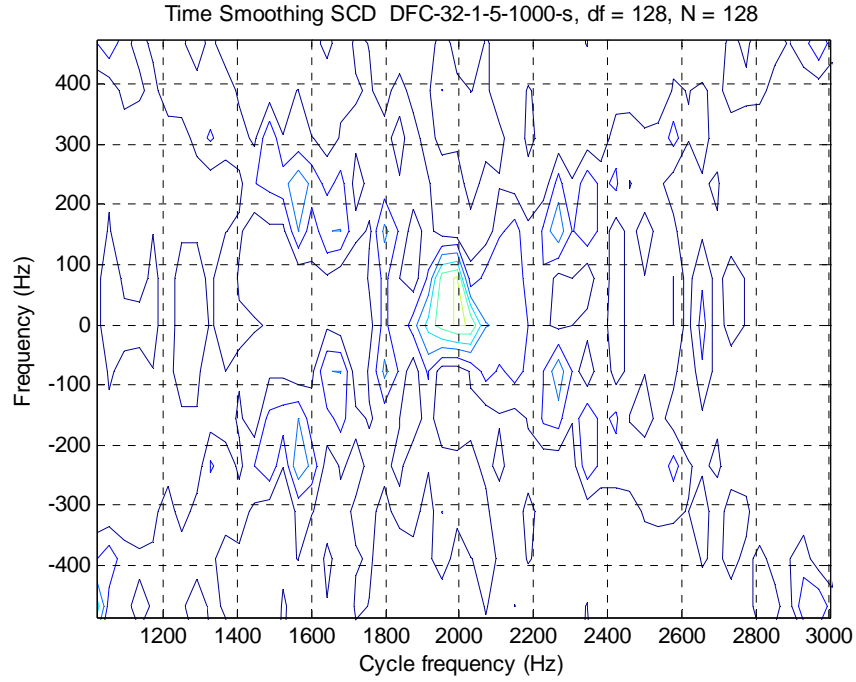
Figure 89.   FAM of DFC 32 Code 1 with $f = 1000$ Hz Individual
Modulation Quadrant.

3.   Conclusions

Cyclostationary spectral analysis provides the most insight to center frequency and bandwidth measurements of the LPI signals. Each pattern was anchored by a multiple of the center frequency and an individual section of the pattern was twice the width of the bandwidth. Within each pattern, the code rate and code period can also be measured to obtain a better idea of the coding being used and the origin of the waveform. The polyphase signals with $N_c \geq 40$ complicate the extraction of detail down to the sub-code level.

THIS PAGE INTENTIONALLY LEFT BLANK

V. UAV SWARM THEORY

A. UAV SWARMS

The concept of a swarm of individuals acting in conjunction with one another to accomplish a greater task is not a new idea. Entire colonies of animals, insects, and organisms depend on the foundations of a swarm to survive. Take ants fighting off a predator for example. A predator many times larger and stronger than an individual ant is easily subdued by the coordinated efforts of a swarm of ants too numerous for the single predator to fend off. A pride of lions hunts in a pack or "swarm." They attack animals much more powerful and sometimes faster and more capable, but with their combined efforts, they capture their prey. From a different viewpoint, the lions' prey by themselves does not have a chance to survive against the pack of lions. However, as a herd or "swarm", the herd always survives because of their numbers and coordinated escape. From nature it can be observed that three main pillars support the swarm concept: survivability of the swarm, the coordination of the swarm through internal communication, and enhanced capabilities of the swarm versus individual capabilities.

The UAV has significant advantages over a traditional surveillance aircraft. First, their name implies that there is no risk of loss of human life when a UAV is sent to a battlefield to perform its mission. The price tag on a UAV is also significantly less than a fighter aircraft, which allows the UAV to enter situations that pose more danger because the risk assessment is lessened. Second, a UAV can operate in an area that is not suitable for human life due to nuclear, chemical, or biological weapons that have been detonated there. This provides for battle damage assessment and other missions of that kind. Finally, the radar cross section (RCS) of a UAV is quite small compared to a fighter aircraft. This means the UAV can infiltrate enemy defenses much further than a fighter and perform missions closer to the enemy [20].

B.   SWARMING MECHANISM

The swarming mechanism is based on the ant-inspired model of foraging for food, which is also displayed in many other biological creatures. The swarm is comprised of individual entities or small units that are in search of a target of interest. The search for such a target is coordinated with the use of chemical substances or pheromones. Pheromone trails are used to guide other ants to the spot where a target of interest has been spotted. Pheromones are continuously laid as the ant searches for a target. As the ant moves further from the colony, the strength of this scent of its trail diminishes. Once the target (use food for instance) has been spotted, the ant takes some of the food and brings it back to the colony. The return trip reinforces the pheromone trail thus confirming the validity of the target. As more and more ants follow the trail to the food, the pheromone trails are strengthened and it is easier for successive ants to gather food for the colony [11].

Termites are another creature that can build elaborate mud arches using the principle of pheromones. The termite senses the pheromone, which tells him to gather up dirt in its mouth and deposit it where the scent of the pheromone is the strongest. The termite gathers dirt and moves to the location of the strongest scent and deposits the mud there. As this process is repeated by a number of termites all leaving their own contribution of pheromone at the scene, the autocatalytic effect takes over. This positive feedback cycle reinforces the strength of the pheromone scent and lures more and more termites to the scene to contribute to the building of the arch, which in turn brings the arch closer to completion. Once the arch has been completed, there will be no more termites following the trail to build the arch, so the pheromones will wear out and the scent will vanish [13].

Fixed action patterns and instinctive behaviors can be explained using the concept of pheromones. These chemicals leave behind odors that, in turn, signal or alert other ants. They are drawn to the possible location based on what signal that particular pheromone sends. Various pheromones are used to trigger different simplistic responses from ants. Pheromones are used to adapt the behavior of the individuals into group

behavior that is more useful and stronger than that of the individual ant. Hence, pheromones are a means of communication between ants that allows them to coordinate their efforts to enable their group to accomplish a goal. Individually, the ants are not a force to be reckoned with in the least, but coordinated together to form a swarm or group; the ants can accomplish extreme feats [11].

The main idea in swarm intelligence is the accomplishment of a grand feat without centralized control, but by using simple tasks that sum together to realize the whole goal. This decentralized control is brought about by *stigmergy*, which is communication by altering the state of the environment in such a way that will affect the behaviors of others for whom the environment is a stimulus. There are two different categories of *stigmergy*, cue-based and sign-based. Cue-based *stigmergy* defines the way a certain event or action is a tell tale indication that the behavior of the individual should change in order to conform to the idea of the group. Sign-based *stigmergy* refers to the signal that is sent to the other individuals, possibly by way of pheromone trail, to change to their actions. The arch building termites' example includes both cue-based and sign-based *stigmergy*. The cue-based *stigmergy* is seen as the tower building process. A termite will see the tower building process beginning and know to gather dirt in its mouth to contribute to the building efforts. The sign-based *stigmergy* is the signal of the pheromone of where to place the dirt from the mouth of the termite. Both *stigmergetic* effects are geared towards the same goal and continue until the task has been completed [13].

C.   UAV SWARM CONCEPT

UAV have become an integral part of the modern battlefield. They have a variety of missions ranging from Intelligence, Surveillance, and Reconnaissance (ISR) missions, to directed fire support of ground troops, to unmanned strike missions. The versatility of the UAV, its relatively low cost as compared to a fighter plane, and its ability to remain hidden from enemy radar (low radar cross-section) make it a very useful platform. However, by itself, the UAV can be overcome by enemy forces. The UAV has little to no armor or defensive components that will ensure it survivability in the case of attack.

To combat this, the idea of the UAV swarm came about to ensure the survivability of the UAV in order to accomplish the mission. The increases productivity and output of the UAV swarm also aided in the development of UAV swarm theory [19].

UAV swarm theory is explained as offensive action generated in pulses by highly dispersed forces that do not employ traditional hierarchical command control structures. The 9/11 attacks are an example of this swarm doctrine. There are many different separate entities that are capable of performing the mission by themselves. The individual UAV are given simple instructions such as, "perform reconnaissance on an enemy military compound." Each UAV can accomplish this mission on its own; however, the more UAV engaged in the mission, the faster it is completed and the better the finished product.

Historical analyses have shown that the Objective Force must possess superiority in the following three battlefield functional capabilities in order to defeat future threats: situational awareness, stand-off lethality, and survivability by agility. Situational awareness is derived from the timely processing and fusion of remote sensor data. Stand-off lethality is highly dependent on an effective merge of sensor grids and shooter grids as targeting data will be contained on both grids and is necessary for an accurate and timely shot. The survivability of a team of UAV is necessary for the post-modern battlefield. Knowledge of when and where to move will minimize vulnerability to enemy defense networks and maximize the capabilities of the autonomous platform [12].

The core idea of the UAV swarm is centered on the ability of the swarm to be able to communicate within itself in order to coordinate their efforts to maximize efficiency and minimize their vulnerability to attack. The possible solution to this is the formation of a "gossip network" between UAV that is used to transfer information from one UAV to another. This wireless network will be open to any UAV joining the mission and will be the medium through which the Digital Information Pheromones (DIP) will be transferred to alert the other UAV in the swarm about the presence of a target or a threat. Much like the ants and termites mentioned above, the pheromones will be digitized and sent through the gossip network and serve the same purpose of alerting other UAV to a discovery made by a UAV in the swarm [19].

The UAV that is uploading important DIP on a possible target location to the pheromone landscape broadcasts a message that alerts other UAV. This message is received by the other UAV in range and directs them to subscribe to the gossip network alerting them to the presence of a new post. The other UAV in range of the initiator UAV will respond with a message acknowledging they have received the message and will establish the wireless communications channel. Each message will contain the location and message time of the initiator UAV. The probability of passing on gossip messages and posts decreases exponentially as distance from the initiator UAV increases. This can be counteracted by the UAV that receive the initiator message relaying that message to other UAV that might be further away from the initiator UAV. This network architecture guarantees the survivability of the gossip network and allows for any of the UAV in the swarm to be a hub, relay, or member in order to complete the mission [19].

D.   ADVANTAGES OF THE UAV SWARM

The advantages of the UAV swarm are precipitated in the interaction within the swarm and the speed with which the swarm of UAV can coordinate their efforts to accomplish their mission. The use of Internet Protocol to convey information over a network has inherent advantages that the UAV gossip network will build on [12]. The use of flags or indicators as to the purpose or content of a packet is used often in Internet Protocol to alert different machines as to the nature of the information they are receiving. The flags that would be most useful to the UAV swarm would be: Deploy (in transit to search region), Exploring (searching region for potential targets), Following (leaves search and traverses path indicated by digital pheromone path to potential target), Monitoring Target (flying close enough to the target to survey it), and Return to Base (UAV has remaining fuel lower level interlock that forces it to disregard further gossip network flags and proceed back to base). Much like the biological creature pheromones, these five flags would be necessary to direct the simple actions of the UAV in order to contribute to the swarm that is trying to accomplish it mission 13].

Two of the flags that can be further manipulated to yield more accurate direction to the UAV are the Following and Monitor Target flags. The Following flag is used at

the onset of target identification by one of the UAV in the swarm. The UAV issues the flag in a message, but there are conditions on the flag released. These conditions refer to the relative certainty with which the initiator UAV is of finding a potential target. If the UAV has detected an enemy radar signal of interest in the threat band and held the signal for enough time to analyze and extract its parameters, then the Follow flag will have a high importance attached to it. This signifies to the other UAV that they should cease their Exploring flag and follow the DIP to the location of the initiator UAV to begin the Monitor Target flag. The other UAV send their messages back to the initiator UAV then head to the first waypoint indicated by the DIP. From here, the DIP will lead the UAV to the location of the first possible target contact and begin their Monitor Target sequence. Conversely, if there was only a brief hit of a radar signal that was unable to be analyzed and therefore only a sporadic indication of a possible target, there will be a low importance flag placed on an uncertain target sighting. Only the closest UAV might leave its search and follow the DIP to the target sighting [13].

The Monitor Target flag is a short duration flag that is used only when a target has been found and data collection is required to fix its position and record its location for future analysis. The Monitor Target flag will be switched on once the UAV arrives at the end of the DIP trail and acquires the possible target's signal. The UAV will then take up a monitoring path that resembles a 90-degree arc around the potential location of the target. The UAV will travel along this arc ensuring it keeps constant contact with the target signal, but remaining far enough away from the target as to keep from arousing suspicion. The UAV will collect data and attempt to extract the parameters of the target signal using its onboard software. Once the UAV has completed the arc, it will have an initial bearing to the signal and a cross bearing from the final bearing to the target. The place where these bearings cross will be recorded by the UAV and will be stored as the location of the target emitting the signal. This data will be uploaded to the gossip network and shared with other UAV to find the most probable location of the target [12].

E. CHALLENGES TO THE SWARM CONCEPT

Despite the gains in surveillance and reconnaissance that a swarm of UAV has over a single platform performing a similar mission, there are some challenges that must be addressed. First is the lack of a physical medium on which to leave a pheromone trail. The first solution to this challenge is somewhat complicated, but given enough development of the idea could provide a nearly untraceable means of communication between UAV. When a UAV wishes to make its message known to the rest of the group, it releases a chemical into the air. This chemical will have much of the same properties as air (density, molecular composition, and temperature) to ensure it does not float away or sink to the ground. Each UAV will have onboard a miniature gas chromatographer that can separate the atomic elements in the air and analyze them. When another UAV detects the chemical that signifies something to the swarm of UAV, such as target has been spotted, it will follow the trail of the chemical until it rendezvous the initiator UAV at the target sighting location. This method of communication is quite primitive and requires further development before bringing it into service, but it most closely resembles that of the biological pheromone trail [13].

The other possible solution to the physical pheromone medium challenge has been introduced above and that is the idea of a gossip network. This network would be localized to the UAV in the swarm and would be used to transfer information and alerts to the other UAV in the swarm. Using Internet protocol and its use of "flags", the UAV will communicate and share information on the network. Each UAV will be programmed to periodically subscribe to the gossip network to receive updated tasking and changes to the mission. In addition, target sightings, locations, and signal parameters of interest will be available for UAV to peruse when they get a chance. Using this network, the UAV will also alert one another to the possible sighting of a target and using DIP they can guide each other on to the trail of the target's signal. This coordination is what gives the swarm of UAV the advantage over one UAV by itself [12].

A second challenge that will have to be addressed is the possibility that a number of the targets being observed by the UAV swarm may not be fixed. Normally, ant targets

are fixed, but UAV targets can be mobile. Therefore, it has been suggested that an anti-pheromone be used to update the location of mobile and dynamic targets. This means that in addition to the DIP, there will be a cancellation DIP that will negate the previous pheromone. On the other hand, if the trail to a target changes, ants continue the trail of DIP to the new location of the target in order to regain access for the rest of the swarm. This continued trail if often inefficient and many times more lengthy that one continuous trail. This aspect of the discussion is critical due to the limited fuel capacities of UAV, the concern for weight restrictions, and the reluctance to take up cargo space with extra fuel. Anti-DIP is a much more direct and efficient way to make a path to a target, but continuing the DIP trail from where it left off to the new location of the target is faster and can be updated closer to real time [12].

F. CONCLUSIONS

The idea of taking a group of advanced unmanned machines and coordinating them to work together like a Navy SEAL Team or a Marine Scout Sniper is a very serious undertaking. With a human unit, there are many concerns such as survivability, sustainability, security, shelf-life of the asset, and most important of all the loss of human life. Many of these concerns are alleviated by using a swarm UAV to accomplish the same mission, but with real time analysis of the intercepted signal, a more efficient and timely acquisition of the target, and above all the absence of the risk of human life. The technology for DIP and gossip networks are progressing and will aid the military in their future ISR missions.

VI. UAV SWARM JAVA PROGRAM

A. PROGRAM BACKGROUND

1. Program Development

The Java program that came before this program was originally created by Chin Lua of the Computer Science and Operations Research Department at North Dakota State University with the intent on employing a swarm of UAV to partake in a synchronized attack against a target of opportunity [21]. The UAV swarm is sent out with the mission to destroy a certain target (enemy radar or other transmitter). Once one of the UAV detects the target, all the other UAV are notified and a surveillance mission is conducted. Once, the target has been adequately confirmed to be the target of interest, the UAV take up attack positions and wait for the countdown to strike. Each UAV carries a small payload and all the munitions are dropped simultaneously on the target at the commencement of the attack.

This Java program has a slightly different mission and therefore has different goals and an entirely different end state. The swarm of UAV is not used for combat or strike missions, but as an ISR mission capable group. The swarm of UAV will be uniquely outfitted with the signal analysis tools discussed above in order to perform ISR missions on all LPI systems and radar signals. The threat of radar systems and netted radar using LPI waveforms a great one for strike aircraft whose radar cross-section is enormous compared to that of a UAV. The Java program shows a simulated ISR mission of a UAV swarm that has been deployed to hunt down an element of an Integrated Air Defense System (IADS). These radar systems could be monostatic or bistatic depending on the technology and the level of integration of the radar network.

The UAV will set out from their base rendezvous point and search an area for LPI signals that correspond to known threat bands of enemy LPI radar. Once found, the UAV detecting the enemy signal will broadcast the detection to the other UAV in the area to assist in data collection and target confirmation. The UAV will take up stations called

orbit stations in an arc at the maximum detection range from the target for survivability concerns. Once the UAV have subscribed to the gossip network and posted their plotted position of the enemy radar target, they will move on. This will continue until: The mission is complete and the UAV are instructed to return home; the low-fuel flag is detected by the swarm and they are ordered to return home; or they are engaged by enemy fire and the mission is aborted.

2.   UAV Response Actions

The UAV swarm will employ three basic actions during its mission. These actions are implemented in the hardware of each UAV, so communication within the swarm for contact avoidance is not necessary. The first of these is the "avoid" maneuver. It entails a UAV detecting two other UAV or any obstacles in its path. The UAV will perform a simple vector analysis of the situation and act accordingly to avoid the two obstacles. The UAV will use the bearings to each of the two obstacles summed together to form the resulting course for contact avoidance. The UAV will continue to move along the new vector and turn clockwise or counterclockwise to avoid any obstacles. This iteration of vector analysis is computationally simplistic in nature and once the UAV is clear of the obstacles, it will return to its original mission of searching for a target or observing a target.

The second simple UAV action is the "attract" maneuver. This movement is in response to a UAV receiving confirmation of a target sighting. The UAV will advance towards the target until it also detects the target. The UAV plots a set of waypoints in a circular fashion around the target. Next, the UAV selects the waypoint most directly between the target and itself and promotes this waypoint to make it the station point. Finally, the UAV moves to the station point in the set to allow it to properly position itself for data collection and to complete its ISR mission.

The third action the UAV performs is the "orbit" maneuver. This movement consists of the UAV finding its station point around which to set up a circular track and then traversing that track or orbit while it completes its mission. The UAV plots a set of waypoints in a circular path around the station point in one quadrant about the target.

The UAV then follows these plotted waypoints while it gathers intelligence on the target. This intelligence will be used to properly identify the target once the mission is completed and most importantly to fix its position for mapping and possible targeting for destruction at a later time. The UAV continues to move in a counterclockwise pattern about the reference point at the maximum detection range of the UAV to the target. Once the requisite amount of intelligence has been gathered, the UAV moves on to search for another target according to its mission parameters [15].

In Figure 90 shown below, the movements and actions of the individual UAV are conceptualized to provide a basis for their actions in the Java Program. The UAV control structure employs a decentralized architecture that is the basis for their autonomous mission capabilities. The UAV respond to their external sensors and inputs from the gossip network. These factors determine the next course of action for the UAV. As part of a UAV swarm, much like the insects addressed above, the initiation of action by one UAV is propagated to the other UAV in order to accomplish the mission through coordinated action.
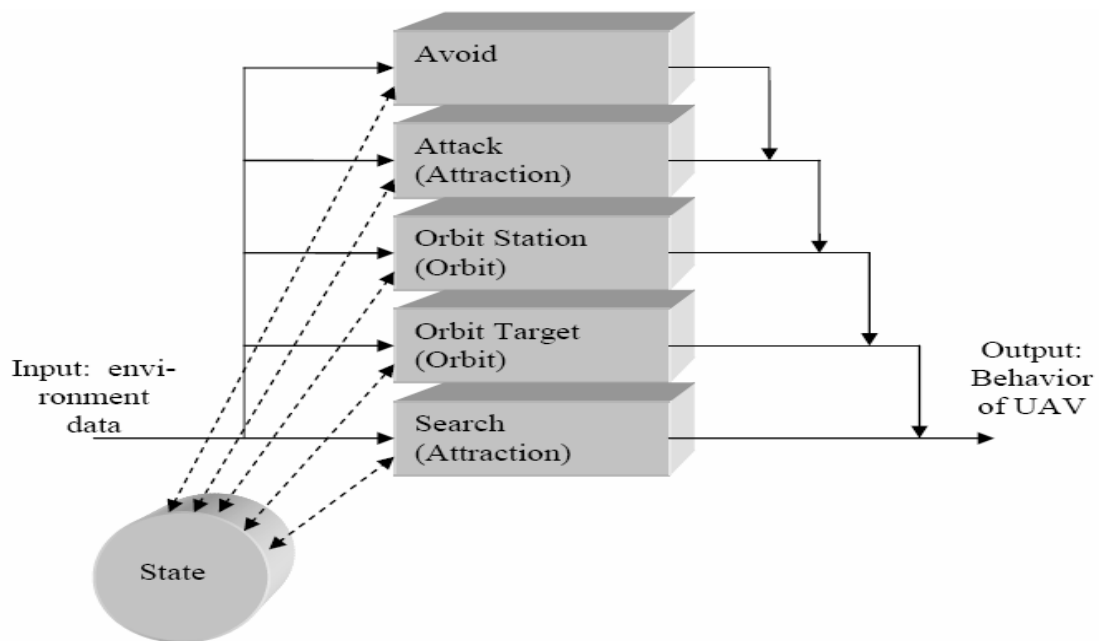
Figure 90.   UAV Control Structure in Java Program.

3.   The Gossip Network Function In The UAV Swarm

The gossip network is essential for the coordination of the UAV in accomplishing their mission. In Figure 91 below, the gossip network traffic is depicted. The UAV 1 is the UAV that in both cases detects the target first. The target detection is denoted by the step increase in awareness of the UAV. This awareness includes the transition from "search" maneuvers to "attract" maneuvers. Once the UAV has calculated the station points and determined which station point to observe the target from, it transitions to "orbit" maneuvers. The sustained value of 0.5 higher than the base value of one for UAV 1 shows a heightened sense of awareness during which time the UAV is observing the target, recording bearing and range information, and passing this data to the other UAV over the gossip network. Once the UAV has finished the requisite actions for target observance, it disengages from the target as shown by the step decrease in awareness to a value of 0.5 lower than the base value. During this time, the UAV is turning to a course that takes it safely away from the target and reassuming its "search" maneuvers.
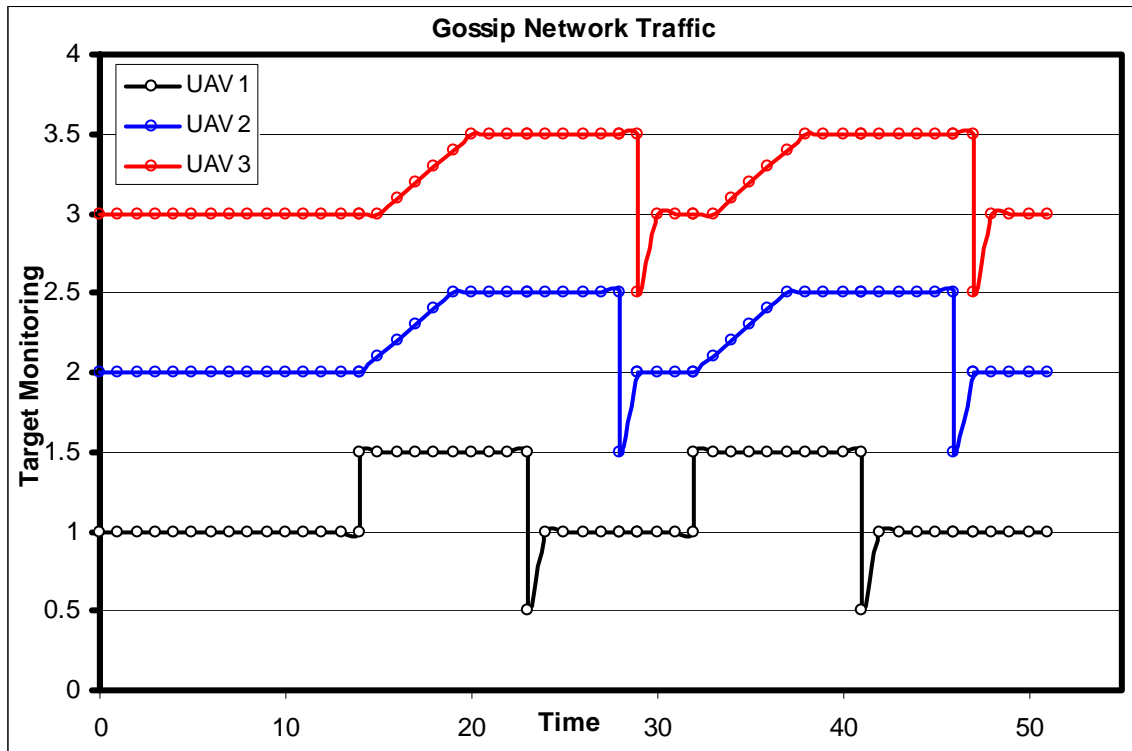
Figure 91.   Gossip Network traffic from three UAV in their search of two targets.

The other two UAV show the results of the message traffic taking place on the gossip network. UAV 2 is the first to receive the target detected broadcast message from UAV 1. The ramp up in awareness for UAV 2 over the course of five time slots shows its transition both in position relative to the target and behavior state. UAV 2 is not so close that it detects the target when UAV 1 does, so it must travel to the waypoint broadcast by UAV 1 once target detection occurs. When UAV 2 reaches a value of 0.5 higher than its base value, it has reached the target detection waypoint and is now performing "attract" maneuvers in order to get into position to correctly observe the target. Once it has reached its station point, it begins to orbit that point and take data on the target by performing "orbit" maneuvers. Upon completion of data collection, UAV follows suit with UAV 1 and returns to its "search" maneuvers to look for the second target.

UAV 3 is the furthest away from the target upon initial detection. UAV 3 does not hear the target detected message broadcast from UAV 1, so that is why its ramp up in awareness occurs one time slot after UAV 2 begins to ramp up awareness. This is because as part of the gossip network, UAV 2 rebroadcasts the target detected message as soon as it is received. UAV 3 is in range of UAV 2, so it hears the message and is thus delayed in reaching the target. In a similar fashion as the other UAV, UAV 3 transitions from "search" maneuvers to "attract" maneuvers upon reaching the target detection waypoint. Once its station point is calculated, it travels to the station point and begins to orbit the station point and perform orbit maneuvers. After sufficient data has been collected and transmitted through the gossip network, UAV 3 disengages from the target and falls back to its "search" maneuvers in order to find the next target.

B. THE UAV SWARM JAVA PROGRAM

1. The Java Program Equivalence

The actions and maneuvers of the UAV swarm are based in part on the capabilities of the Compact LCR-100 Electronic Intelligence (ELINT) receiver that can be carried onboard a UAV with little restriction on overall payload and endurance. This

is an example of the type of sensor needed to enable the performance of the UAV swarm in a similar manner to the Java program. This receiver weighs about a pound and occupies only 12 cubic inches of payload space. Its sensitivity is approximately -105 dB and covers a frequency range of 0.5 – 18 GHz. These statistics are a minimum requirement to ensure the effectiveness and survivability of the UAV Swarm.

All the measurements and distances in the UAV Swarm Java program are referenced to pixels on a computer screen. The target mark that the UAV are trying to detect is a diameter of 10 pixels. To make a more useful parallel, it is assumed that a radar site would be 150 feet in diameter; hence, the ratio of computer pixels to feet is 1:15. The vision range of a UAV searching for a target is 400 pixels or 6,000 feet. This is just over a mile, which is typical when searching for a LPI emitter. This means that the swarm of UAV must comb their search terrain and come to within a mile of the LPI emitter in order for the ELINT receiver to detect the LPI signal waveform and extract its parameters using the methods discussed above. This range is very close to the LPI emitter, but with such a small RCS, the UAV has a low probability of detection.

The other parameters of the UAV Swarm such as maximum speed and maximum turn are arbitrary constraints for a generic UAV. Some newer UAV can go faster and have a smaller turning radius, but these limits were chosen to maximize on station time and minimize fuel consumption. The repulsion range variable refers to the minimum distance required between one UAV and another to prevent collisions and provide for adequate maneuver room to avoid other contacts. A UAV model with more sophisticated avoidance algorithms or faster processors could reduce the repulsion range, but this value was chosen for the generic UAV model.

The on station time required for adequate surveillance and target location determination is based in part on the time required to pull the signal out of the environment and in part on the direction finding (DF) and ranging capabilities of the UAV antenna supported by the ELINT receiver. The time required to fix the target's position is inversely proportional to the number of UAV attempting to find the target.

This means that as the number of UAV increases, the time required to fix the target's position goes down. This is another reason that a swarm of UAV is very effective in both finding and pinpointing a target's position.

The time required to fix a target's position is largely dependent on two factors: the bearing and range errors of the ELINT sensor and the number and location of data points uploaded to the gossip network, which is dependent on the number of UAV in the swarm. The bearing and range error of an ELINT sensor's DF capabilities are rarely adjustable. The more advanced the sensor, the smaller the error.

The UAV swarm presents a solution to this problem by providing more data points in a timelier manner. One UAV trying to DF a target would produce a circular error probable (CEP) many times larger than a swarm of five UAV. This is due to inability of one UAV to get data points quick enough and accurately enough. In Figure 91 below, the relative differences between the CEP of one UAV and five UAV are shown. With five UAV, the CEP is constricted due to the increased number of data points and the locations of the UAV. Figure 92 below shows the reduction in the CEP from just two UAV at crossed bearings. The gray ellipses depict the CEP produced when one UAV attempts to DF the target. The blackened area where the two ellipses cross shows the reduced area of commonality between the two bearings and ranges. The black circle around the target (red circle inside the blackened area) shows the resulting CEP when the two data points are uploaded to the gossip network. The gossip network is instrumental in the comparing and contrasting of the data points from all the UAV in the swarm. The individual UAV contribute to the final target location CEP and that location is saved on board every UAV to ensure survivability of the mission and use in future missions [22].
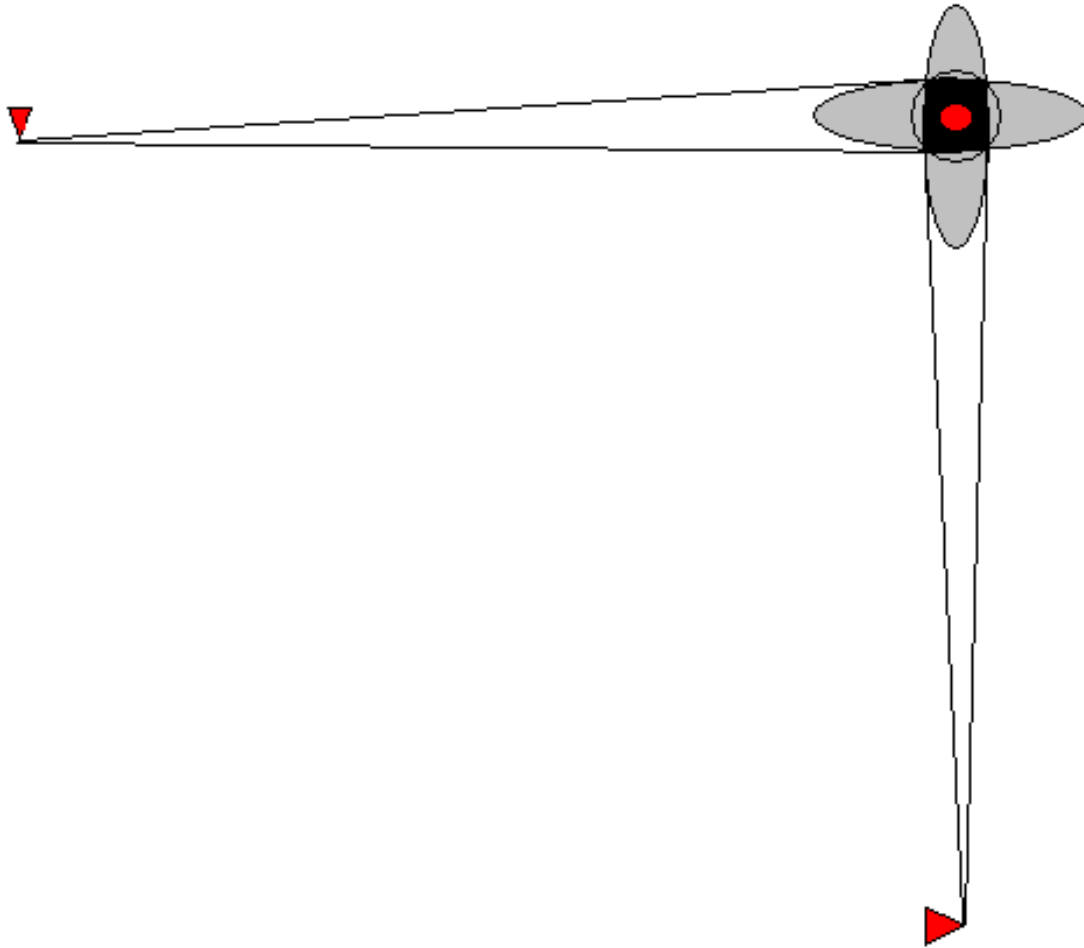
Figure 92.   Illustration of UAV Swarm reduction target location CEP [22].

2.   UAV Swarm Detection Process

The Java Program illustrates the interaction of the UAV as they traverse their search area in order to accomplish their mission. Each time new data is obtained by any of the UAV in the swarm, the information is relayed by the gossip network to each of the other UAV. This promotes the coordination of UAV actions so that the effective efforts of the UAV swarm are increased. The individual UAV can find all the targets by itself, but would have to remain on station for longer in order to obtain a more accurate target location. Figure 93 illustrates the coordination of the UAV through the gossip network in finding and fixing the positions of the two targets below.

In the simulation in Figure 93 below, three UAV are searching for two targets situated about ten miles apart. UAV 1 is the black track, UAV 2 is the blue track, and UAV 3 is the red track. The UAV start their mission at the far left vertically stacked using search mode to find the first target. As discussed, this is a simple mode that tells the UAV to continue along a predetermined path (in this case it is a saw tooth course to the southeast) until it detects the target. Once target detection is accomplished by UAV 1, its detection is relayed over the gossip network by a message containing waypoint data and initial radar signal parameters (these are rough estimates of carrier frequency and bandwidth) and broadcasts that to the other UAV in range. The other UAV broadcast the same message including the data time group (DTG) so each UAV can determine its location relative to the target detection sighting. Once a UAV receives a target detection message from another UAV, it alters its course to align with the target detection waypoint and proceeds to that point.

Once a UAV reaches the initial target detection waypoint, it proceeds to follow its programmed path to determine which station point it should take up in order to perform surveillance and data collection on the target. Each successive UAV fills in the next station circle over from the previous one and begins its orbit. The maneuvers required for a UAV to travel from its search point to its station circle are quite simple and are mostly comprised of avoidance maneuvers to prevent collisions between UAV. Once each UAV has obtained a station circle it begin to orbit and transitions to the data collecting phase of the target location process.

At the onset of a UAV reaching a station and orbiting the station point, it begins taking data on the target signal's waveform. The goals are two fold: attempt to extract the LPI signal parameters during surveillance for future use against the target weapons system and obtain a requisite number of DF values to include bearing and range at a minimum in order to provide enough data to upload an accurate value to the gossip network for comparison with the other UAV in the swarm. The accomplishment of the first task can be difficult and possibly not occur at all. Since the UAV is gathering the data, it can be analyzed later by a computer with more processing power than the one on board a UAV. The second task is essential to the mission and thus is the first priority of

the UAV. Each UAV systematically takes data ensuring it receives a data point every time it passes around its orbit. The bearing and range values are averaged and this final product is uploaded to the gossip network for comparison by the other UAV. Once all the UAV have uploaded their data, the orbit phase is complete and the UAV swarm moves on according to their mission requirements.

Once the target's position is fixed and recorded by the other UAV through the gossip network, the UAV swarm then moves to the next target. The second search pattern of the UAV swarm is a saw tooth course to the northeast to detect the second target and fix its position. This search and seek pattern can be duplicated until the UAV swarm reaches its fuel limits or its memory limits with the LPI signal parameters and the target's positions.
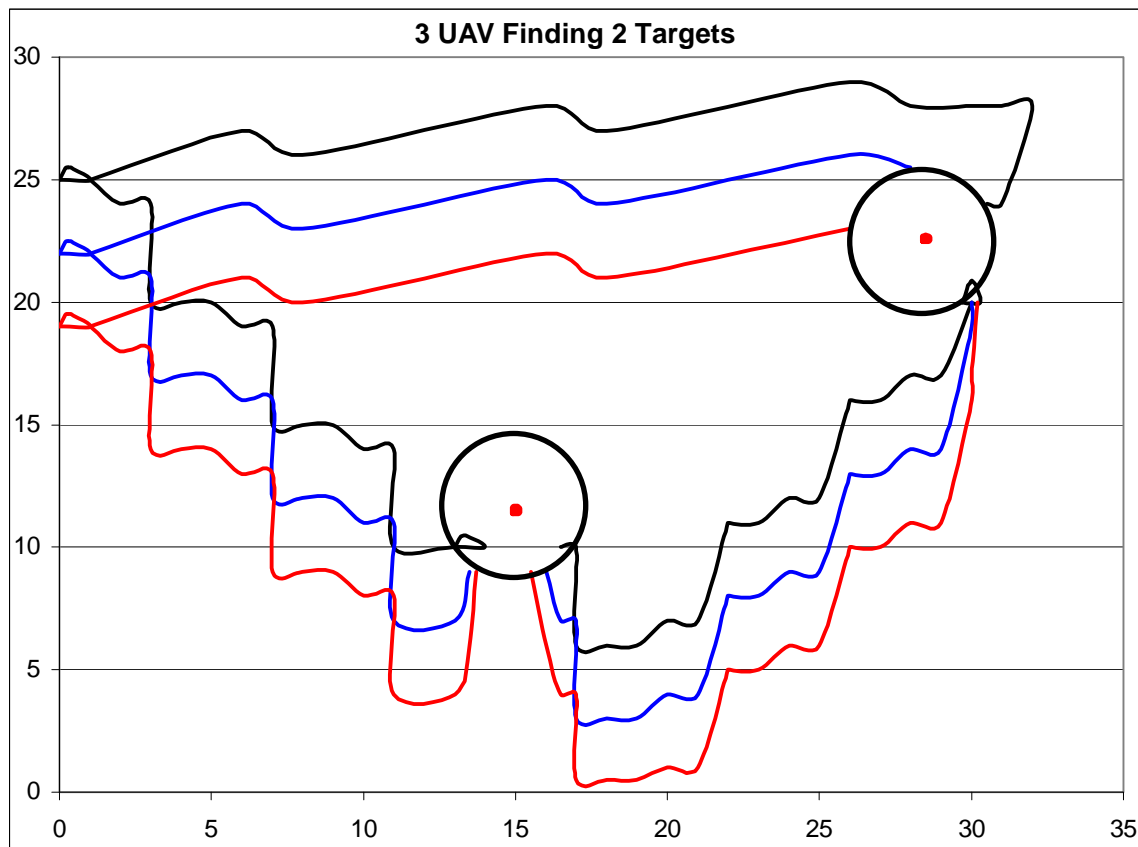

Figure 93. UAV target detection path showing communications with other UAV.

VII. CONCLUSIONS

The four LPI signals introduced in this document perform well when implemented in a networked LPI radar system. They illustrate the value of employing complex signal designs to improve the performance of LPI radar from three aspects: radar capable of identifying and locating targets, the ability to remain undetected during periods of radiation and to provide a cooperative signal environment for multiple radar sites to function as bistatic radars for one another throughout the network. A networked radar system could also use these standard signal design patterns and have another code set prepared in reserve for use during times of war. This would reduce the opportunities for non-cooperative ESR operators to prosecute the reserve code sets and only present the standard design for training and during peacetime.

Current non-cooperative signal prosecution techniques though capable of identifying the presence of a signal are not capable of extracting detailed information of regarding the transmitted signal's parameters. Basic patterns are discernable such as approximate center frequency and cycle repetition (for poly-phase only).   When compared to other poly-phase coded signals (Frank or P1-P4), it is more difficult to extract parameter information from the OPS codes. All the signal parameter extraction techniques are required to identify these signal parameters. Although these signals do not necessarily need to be used by a network of radars, they each have excellent performance when used alone in netted LPI radar systems. Longer code sequences could be generated to further prevent exploitation by non-cooperative ESR.

The UAV swarm concept was explored and proved to be a great asset for future ISR missions. The capabilities it provides in signal detection and target geo-location coupled with removing the risk to personnel has the potential to aid ground forces in combat. The UAV swarm can also be used for other missions to include stand-in radar jamming and strike missions. The key to the success of the UAV swarm is coordination and communication. One UAV is quite capable by itself, but in the same way as the ant and termite colonies, the individual is far surpassed by the swarm in a coordinated effort.

113

THIS PAGE INTENTIONALLY LEFT BLANK

LIST OF REFERENCES

[1]   P.E. Pace (2004). Detecting and Classifying Low Probability of Intercept Radar. Boston, MA: Artech House.

[2]   MATLAB® Software – Version 7.5.0.342, Release 2007b on PCWIN, The MathWorks, Inc., August 15, 2007

[3]   Hai Deng (2004, November). Polyphase Code Design for Orthogonal Netted Radar Systems. *IEEE Transactions on Signal Processing,* Vol. 52, No. 11, 3126-3135.

[4]   Hai Deng (2004, February). Discrete Frequency-Coding Waveform Design for Netted Radar Systems. *IEEE Signal Processing Letters,* Vol. 11, No. 2, 179-182.

[5]   A. Hammad, Khan, Zhang, Yangyang, Ji, Chunlin, Stevens, Christopher J., Edwards, David J., & O'Brien, Dominic (2006, October). Optimizing Polyphase Sequences for Orthogonal Netted Radar. *IEEE Signal Processing Letters*, Vol. 13, No. 10, 589-592.

[6]   A. Hammad, Taboada, Fernando. "Detection and Classification of LPI Radar Signals Using Parallel Filter Arrays and Higher Order Statistics," NPS Master's Thesis, September 2002

[7]   Eric J. Carlson (1988). Low Probability of Intercept (LPI) Techniques and Implementations for Radar Systems. *IEEE Transactions on Aerospace and Electronic Systems*. 56-60.

[8]   Nadav Levanon (2002, July). MATLAB Code for Plotting Ambiguity Functions. *IEEE Transactions on Aerospace and Electronic Systems*, Vol. 38, No. 3, 1064-1068.

[9]   Y. Teng, Baker, C., & Woodbridge K. (2006). Netted Radar Sensitivity and the Ambiguity Function. *IEEE, Department of EE, University College London*, 6-9.

[10]   Nadav Levanon & Mozeson, Eli (2004). Radar Signals. Hoboken, NJ: John Wiley and Sons Incorporated.

[11]   James Kennedy & Eberhart, Russell C. (2001). Swarm Intelligence. San Diego, CA: Academic Press.

[12]   S. Li, Boskovic, J. D., Seereeram, S., Prasanth, R., Amin, J., & Mehra, R. (2002). Autonomous Hierarchical Control of Multiple UCAVs. 274-279.

[13]   D. M.Hart & Craig-Hart, P. A. (2004). Reducing Swarming Theory to Practice for UAV Control. *Proceedings of the Aerospace Conference, IEEE*. 3050-3063.

[14]   Nadav Levanon & Freedman A. (1994, July). Properties of the Periodic Ambiguity Function. *IEEE Transactions on Aerospace and Electronic Systems*, Vol. 30, No. 3, 938-941.

[15]   C. A. Lua, Altenburg, K., & Nygard, K. E. Synchronized Multi-Point Attack by Autonomous Reactive Vehicles with Simple Local Communication. *North Dakota State University*, Retrieved July 01, 2007, from http://www.cs.ndsu.nodak.edu/~nygard.

[16]   Nadav Levanon & Mozeson, Eli (2004). Radar Signals. Hoboken, NJ: John Wiley and Sons Incorporated.

[17]   Jacquie Barker (2005). *Beginning Java Objects: From Concepts to Code, Second Edition*. Berkeley, CA: Apress.

[18]   Y. Teng, Griffiths, H. D., Baker, C. J., Woodbridge, K. (2007). "Netted radar sensitivity and ambiguity," in *IET Radar Sonar Navigation*, Vol. 1, No. 6, 479-486.

[19]   Prithviraj Dasgupta. (2008, May). A Multi-agent Swarming System for Distributed Automatic target Recognition Using Unmanned Aerial Vehicles. *IEEE Transactions on Systems, Man, and Cybernetics,* Vol. 38, No. 3, 549-563.

[20]   I. C. Price & Lamont, G. B. (2006). GA Directed Self-Organized Search and Attack UAV Swarms. *IEEE Proceedings of the 2006 Winter Simulation Conference*. 1307-1314.

[21]   Natalie R. Frantz. – "Swarm Intelligence for Autonomous UAV Control," NPS Master's Thesis, June 2005.

[22]   A. Finn, Brown, K., & Lindsay, T. (2002). Miniature UAVs & Future Electronic Warfare. *Proceedings of the Land Warfare Conference, Brisbane, Australia*. 1-12.

INITIAL DISTRIBUTION LIST

1. Defense Technical Information Center
   Ft. Belvoir, Virginia

2. Dudley Knox Library
   Naval Postgraduate School
   Monterey, California

3. Professor Phillip E. Pace
   Naval Postgraduate School
   Monterey, California

4. LTC Terry Smith
   Naval Postgraduate School
   Monterey, California

5. Mr. and Mrs. Michael Crescitelli
   El Cajon, California

6. Ronald Kistner
   Jefferson, South Dakota